SCHOOL OF CHEMISTRY
THE UNIVERSITY OF EDINBURGH

Synthesis of Polymers of Intrinsic Microporosity derived from rigid bridged bicyclic monomers for gas separation

Thesis submitted for the degree of Doctor of Philosophy by:

Yuancheng Liu

Supervisor: Neil B. McKeown **2025**

Declaration

Statement 1

This work has not been submitted in substance for any other degree or award at this or any other university or place of learning, nor is it being submitted concurrently in candidature for any degree or other award.

Signed ………………………………………… (candidate)
Date …25/11/2025……………………………

Statement 2

This thesis is being submitted in partial fulfilment of the requirements for the degree of Doctor of Philosophy.

Signed ………………………………………… (candidate)
Date …25/11/2025……………………………

Statement 3

This thesis is the result of my own independent work/investigation, except where otherwise stated. Other sources are acknowledged by explicit references. Any views expressed are my own.

Signed ………………………………………… (candidate)
Date …25/11/2025……………………………

Statement 4

I hereby give consent for my thesis, if accepted, to be available for photocopying and for inter-library loan, and for the title and summary to be made available to outside organisations.

Signed ………………………………………… (candidate)
Date …25/11/2025……………………………

Acknowledgements

First and foremost, I would like to express my gratitude to my supervisor, Professor Neil McKeown, for giving me the opportunity to carry out my PhD within his research group. I really appreciate all his support, guidance, encouragement, and full academic freedom to conduct my project over the last three years. I was deeply impressed by his prompt suggestions and feedback in response to any questions I had.

A special thank you to Dr John Tobin for his assistance in the lab and help with BET data. I am grateful to Dr Dominic Taylor for his extensive support during my PhD. I would like to thank our current and former group members: Khairul, Emily, Kimia, Shuhua, Shannah, Yihao, Kim, Yanbo, Anli and Xin Peng for their support and help in building a collegial and respectful working environment. I am sincerely grateful for your contributions; this thesis would not have been possible without the collective effort and support from each and every one of you.

I would like to express my sincere gratitude to the academic, administrative, and technical staff of the School of Chemistry at the University of Edinburgh. Thanks to their support and dedication, a convenient and excellent academic environment was created, which was of great importance to the completion of this project. I am grateful to the School of Chemistry for the tuition fee waiver, which gave me the valuable opportunity to undertake my PhD at the University of Edinburgh.

I would like to acknowledge the financial support sponsored by the China Scholarship Council.

Finally, I would like to thank my parents for always being on my side, and for their unwavering love, encouragement, and understanding throughout this challenging academic journey.

Lay Abstract

Membranes based on polymers are of increasing use for energy-efficient separations of industrial gas mixtures, including natural gas or biogas upgrading (CO_2/CH_4), oxygen or nitrogen enrichment of air (O_2/N_2) and hydrogen recovery from ammonia purge gases (H_2/N_2). Membranes with high permeability and high selectivity are desirable for enhancing productivity and process efficiency, while reducing the overall size and manufacturing cost of membrane systems. Polymers of Intrinsic Microporosity (PIMs), characterised by their rigid and contorted macromolecular structures, offer exceptionally high permeability with moderate selectivity and have emerged as promising materials for gas separation.

Highly rigid bridged bicyclic units such as triptycene (Trip) and benzotriptycene (Btrip) generate intermolecular free volume (IMFV) that is configuration-based and intrinsic to their superrigid molecular backbone, thereby offering polymers with exceptional gas separation performance. This project describes the synthesis of a series of novel monomers featuring rigid bridged bicyclic structures. These monomers were designed with the intention to conform to the concept of PIMs, generating rigid and contorted polymer structures. The synthesised monomers were subsequently used as building blocks for the preparation of PIMs. The synthesised PIMs exhibited enhanced intrinsic microporosity, high gas adsorption capacity and excellent thermal stability. Several PIMs demonstrate exceptional gas separation performance.

Abstract

Polymers of Intrinsic Microporosity (PIMs) are a relatively new class of microporous materials, first reported in 2004. The rigid and contorted macromolecular structures provide PIMs with unique solution processability and high free volume, which support the rapid and selective transport of small molecules. PIMs show great potential in gas separations due to their high permeability with great selectivity. This project focuses on the synthesis of novel PIMs that can form self-standing films suitable for gas permeability measurements.

The first part involves the preparation of a series of copolymers based on three naphthopleiadene (NP) derivatives. The substitution with various functional groups on the NP scaffold enabled modification of the polymer backbone, so that we could tune the physical and microporous properties. These copolymers exhibit ultra-microporosity and a large BET surface area. Robust self-standing films were obtained from these NP-based copolymers.

In the second part, benzopleiadene (BP), a novel bridged bicyclic monomer composed of two catechol units and a single naphthalene core fused at two bridgehead carbon atoms, was designed and synthesised. The homopolymer (PIM-BP) was prepared based on dibenzodioxin formation. PIM-BP exhibits high permeability and remarkable selectivity for carbon capture (CO_2/N_2), natural gas purification (CO_2/CH_4) and oxygen enrichment (O_2/N_2). A series of copolymers composed of PIM-BP and PIM-1 were prepared. In particular, the copolymer PIM-BP_{75} demonstrates gas separation performance comparable to that of PIM-BP, along with improved solubility. The homopolymer PIM-BP was further modified via amidoxime functionalisation. As expected, amidoxime functionalised PIM-BP (AO-PIM-BP) exhibits ultra-high selectivities and high permeabilities for hydrogen recovery (H_2/N_2 and H_2/CH_4).

In the third part, a novel aryl ether-bridged dinaphthalene (EDN) monomer, structurally similar to the NP scaffold, was synthesised. The EDN monomer was used to prepare the linear polymers (PEEK-EDN and PES-EDN), from which robust self-standing films were successfully obtained. Despite their extremely low gas permeabilities for all gases, both polymers demonstrate excellent H_2/N_2 and H_2/CH_4 selectivities above those of existing PEEK polymers.

Finally, a novel dimethoxy-functionalised benzopleiadene (DMBP) monomer, structurally based on the BP scaffold, was synthesised via an intramolecular Friedel–Crafts cycloalkylation. Polymer PEN-DHBP based on the DHBP (the demethylation product of DMBP) was prepared.

Overall, this thesis focuses on a comprehensive study of the synthesis of novel monomers, highlighting their potential applications in gas separations.

Abbreviations

AO	Amidoxime	**MS**	Mass Spectrometry
BET	Brunauer–Emmett–Teller	**NMP**	*N*-methyl-2-pyrrolidone
BTrip	Benzotriptycene	**NMR**	Nuclear magnetic resonance
COFs	Covalent organic frameworks	**NP**	Naphthopleiadene
DCM	Dichloromethane	**PAE**	Poly(arylene ether)
DMAc	Dimethylacetamide	**PEEK**	Poly(ether ether ketone)
DMF	*N,N*-dimethylformamide	**PES**	Poly(ether ether sulfone)
DMSO	Dimethyl sulfoxide	**PIMs**	Polymers of intrinsic microporosity
EA	Ethanoanthracene	**SBF**	Spirobifluorene
FTIR	Fourier transform infrared spectroscopy	**SBI**	Spirobisindane
HCl	Hydrochloric acid	**S_NAr**	Nucleophilic aromatic substitution
HCP	Hyper-crosslinked polymer	**TB**	Tröger’s base
IMFV	Internal molecular free volume	**TFTPN**	Tetrafluoroterephthalonitrile
IUPAC	International Union of Pure and Applied Chemistry	**TGA**	Thermo-gravimetric analysis
MeOH	Methanol	**THF**	Tetrahydrofuran
MOF	Metal organic frameworks	**Trip**	Triptycene
Mp	Melting point	**TTSBI**	5,5',6,6'-Tetrahydroxy-3,3,3',3'-tetramethyl-1,1'- spirobisindane

Table of Contents

Chapter 1: Introduction

1.1 Porous Materials

Porous materials are characterized by containing cavities, channels or interstices, where the depth of the voids exceeds their width. According to the International Union of Pure and Applied Chemistry (IUPAC), porous materials are further classified into three groups based on their predominant pore sizes: microporous (< 2 nm), mesoporous (2-50 nm), and macroporous (> 50 nm) materials.[1] Additionally, micropores are further classified into two subcategories: ultramicroporous (< 0.7 nm) and supermicropores (> 0.7 nm).[2]

In addition to their width, pores can be also categorised based on their accessibility to external fluids (**Fig 1.1**). Pores that are completely isolated from their surroundings are described as closed pores (**a**). These pores can influence the macroscopic properties such as the bulk density, mechanical strength and thermal conductivity of the materials. However, they are not associated with fluid flow and gas adsorption. In contrast, pores that are connected to external surface are referred to as open pores (**b-f**). Among them, some may be open only at one end (**b** and **f**), and are described as blind pores. Others may be open at two ends (**e**), which are described as through pores. Pores can also be classified according to their shape, they can be cylindrical (**c** and **f**), ink-bottle-shaped (**b**), and funnel-shaped (**d**).[1]

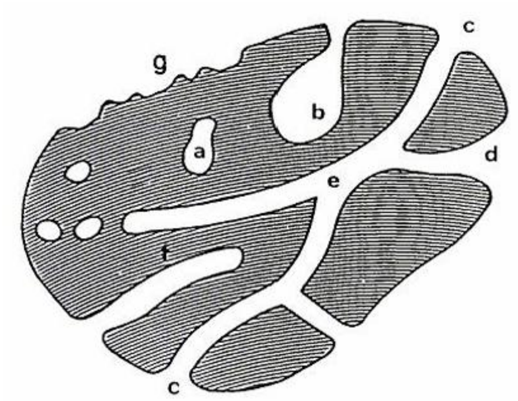

Fig 1.1 Schematic cross-section of a porous solid.[1] Reproduced from Pure & Appl. Chem. 1994, 66, 1739–1758, © 2013 Walter de Gruyter GmbH, Berlin/Boston.

1.2 Surface Area

Some important parameters such as specific surface area, pore volume and pore size distribution of porous materials can greatly influence their performance in various applications.[3-5] There are many established techniques to characterise the pore structures. It should be noted that different methods are based on specific physical principles and the nature of the probe used (e.g., atom or molecule), and therefore each method is only applicable within a certain pore-size range.[1] Consequently, the selection of the appropriate method should start from both the material investigated and its intended application.[6] **Figure 1.2** illustrates the ranges of validity of a selection of methods commonly used to characterise the pore structure.

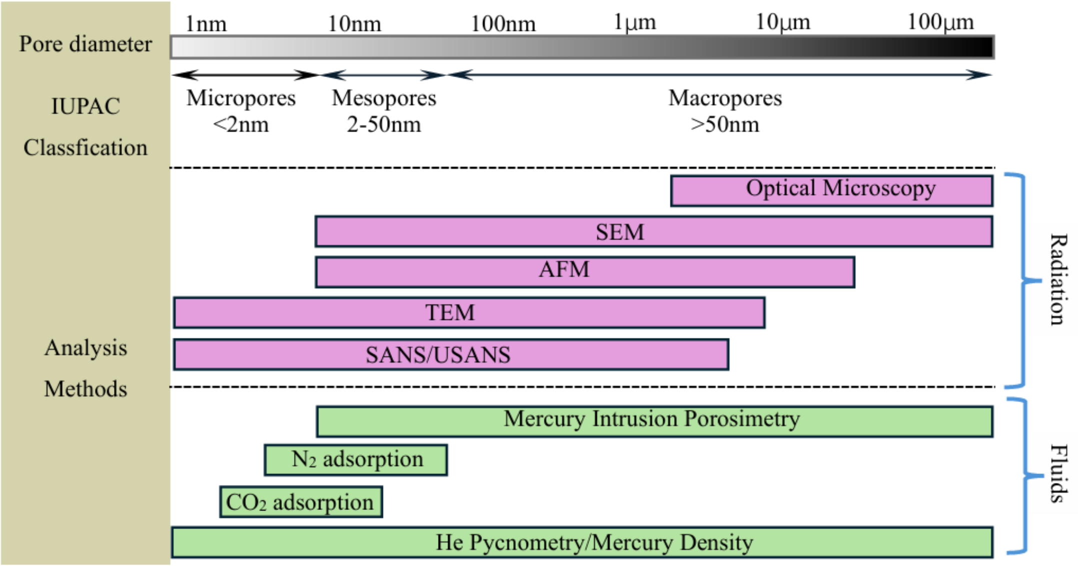

Fig 1.2 Measuring ranges of methods to characterise the pores (modified from[7]).

Gas adsorption measurement is the most widely used technique for the characterisation of microporous materials (e.g., carbons, zeolites and organic polymers). Depending on the nature of the interactions, adsorption can be physical (physisorption) or chemical (chemisorption). Physisorption is driven by weak intermolecular interactions such as van der Waals forces, whereas chemisorption involves the formation of chemical bonds. In gas adsorption technique, physisorption is utilised to determine the surface area, pore volume, and pore size distribution of microporous materials. Nitrogen (at 77 K) is the commonly used adsorbate for determining the specific surface area and mesopore size distribution. Carbon dioxide (at 273 K) is the recommended probe molecule to obtain a reliable assessment of the micropore size distribution.[6]

The gas adsorption measurement procedure is described as following: prior to the measurement, the sample is degassed under high vacuum at elevated temperature to obtain a clean surface and then placed into a sample cell. The construction of the isotherm typically involves a point-by-point process through the controlled introduction and removal of known amounts of gas, allowing sufficient time for equilibration at each point. The specific surface area can be then calculated using Brunauer–Emmett–Teller (BET) theory,[8] an extension of Langmuir theory.[9]

For the evaluation of adsorption data, it is recommended that adsorption isotherms be presented in graphical form according to their qualitative nature. The adsorption isotherms of porous materials can be classified into six types according to IUPAC (**Figure 1.3**).

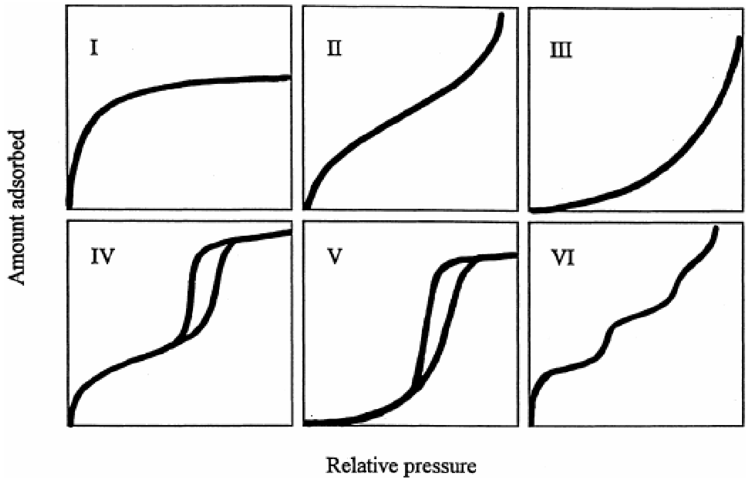

Fig 1.3 The IUPAC classification of adsorption isotherms.[10]

Type I isotherms are typically observed for microporous materials, where a steep uptake occurs at very low relative pressure due to enhanced adsorbent-adsorptive interactions in narrow micropores, resulting in micropore filling at very low relative pressure. The adsorption reaches a limiting uptake as nearly all available micropores are filled, and this limiting uptake is determined by the accessible micropore volume rather than by the internal surface area.[2, 10]

Type II isotherms are commonly observed in nonporous or macroporous materials with unrestricted monolayer-multilayer adsorption up to high relative pressure. The knee in the curve usually represents the completion of monolayer adsorption and the transition into multilayer adsorption.[2, 10]

Type III isotherms are relatively uncommon and typically observed when adsorbate-adsorbate interactions dominate over adsorbate-adsorbent interactions. This leads to the adsorbed molecules clustering around the most favorable sites on the surface of nonporous or macroporous materials. In contrast to a Type II isotherm, the amount adsorbed remains finite at the saturation pressure rather than forming an identifiable monolayer.[2, 10]

Type IV isotherms are typically observed in mesoporous materials and exhibit a hysteresis loop, resulting from capillary condensation occurring in mesopores. The adsorption reaches a limiting uptake at high relative pressures. The initial stage of the Type IV isotherm is associated with monolayer-multilayer adsorption, as it follows the same trend to the corresponding section of a Type II isotherm.[2, 10]

Type V isotherm is very similar to that of Type III, and this can be attributed to relatively weak adsorbent–adsorbate interactions; however, it occurs with certain porous adsorbents.[2, 10]

Type VI are characterised by stepwise multilayer adsorption on a uniform non-porous surface. The step-height indicates the monolayer capacity for each adsorbed layer, whereas the steepness of the step depends on the system and temperature.[2, 10]

1.3 Microporous Materials

Microporous materials have been widely used in the field of catalysis, adsorption, separation and energy storage over the past decades.[11-15] Due to their huge technological potential and advances in synthesis, microporous materials are still a rapidly developing field, attracting significant research interest and driving innovation across various industries. In addition to well-established commercial materials such as zeolites and activated carbons, numerous functional porous materials have emerged, including hyper-crosslinked polymers (HCPs), covalent organic frameworks (COFs), metal-organic frameworks (MOFs), and polymers of intrinsic microporosity (PIMs).[16-18]

1.3.1 Activated Carbons

Activated carbons are porous, amorphous carbon-based material composed of graphitic layers.[19] Activated carbons are generally produced from a variety of carbon-rich materials such as coal, wood and lignite.[20-21]The synthesis of activated carbon typically involves two main stages: pyrolysis carbonization of the precursor material and the activation process, activation can be performed using either physical or chemical techniques. Carbonization is a thermal decomposition stage in which carbon precursors are converted into carbon-rich materials at relatively high temperatures while restricting the access of reactive gases, such as oxygen. During this process, volatile compounds are released in gaseous form, contributing to the formation of a porous structure.[22-23] The physical activation generally involves a partial gasification process using steam, carbon dioxide or hot air mixtures with a high temperature of 800-1000 °C.[24-25] Chemical activation typically involves the use of acid or base activators, followed by thermal treatment at 400–600 °C in an inert gas atmosphere.[26-27]

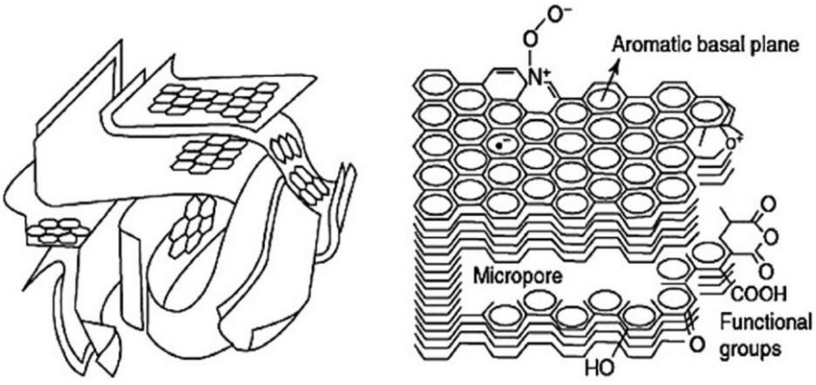

Fig 1.4 Structural model of activated carbons.[28] Reproduced from P. T. Moseley *et al.*, J. Energy Storage 2018, 19, 272–290. License (CC BY NC ND).

Activated carbons have been recognised as one of the oldest microporous materials with a long history of commercial applications. The highly porous structure of activated carbons contributes to their exceptionally large surface area, typically ranging from 700 to 1200 m^2 g^{-1}, and their superior adsorption capacity, which gives them the potential to be excellent adsorbents.[29] Activated carbons possess a well-organized pore structure, ranging from macropores and mesopores to micropores, along with a wide range of surface functional groups present on the surface of activated carbons such as hydroxyl and carboxyl (**Fig 1.4**).[30] Due to these unique properties, activated carbons have been widely used for a wide range of applications, including carbon dioxide capture,[31] water treatment,[32] gas separation[19] and heavy metal adsorption.[33]

1.3.2 Zeolites

Zeolites are another class of well-established microporous materials with a crystalline aluminosilicate framework. Typical zeolites are constructed from corner-sharing SiO_4 and AlO_4 tetrahedra units bridged through oxygen atoms (**Fig 1.5**), forming a three-dimensional framework with well-defined pore size and high thermal stability.[34] The term 'zeolite' was first coined by the Swedish mineralogist Alex F. Cronstedt in 1756, when he observed the mineral sample producing large amount of steam upon heating.[35-36] The well-ordered structure and compositional tunability of zeolites result in interconnected channels with narrow and uniform pore size distributions ranging from 4 to 20 Å.[37]

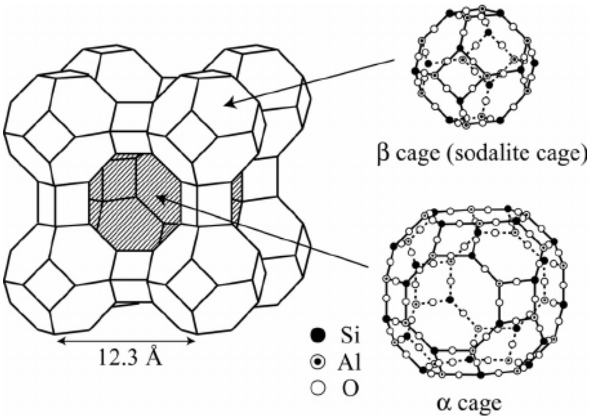

Fig 1.5 Schematic representation of the framework structure of aluminosilicate zeolite A.[38]

The isomorphous substitution of SiO_4 with AlO_4 introduces a negative charge, which is compensated by extra-framework cations, such as Na^+, K^+, Mg^{2+}, and Ca^{2+}. These cations could then be easily exchanged with other cations in solution. These cations reside within the pores and cavities of the zeolite framework and can be either organic or inorganic without destroying the structure, including alkylammonium, alkali metals, alkaline earth metals, and other metal species.[39] Their type and distribution significantly influence the physicochemical properties of zeolites.[40] Due to their well-ordered framework, compositional richness and commercial availability, zeolites have been used in numerous applications, such as catalysts,[41] ion exchangers,[42] adsorbents[43] and separation.[44]

1.3.3 Hyper-Crosslinked Polymers (HCPs)

Hyper-crosslinked polymers (HCPs) represent a class of organic porous materials that possess a rigid and highly crosslinked network structure. In the early 1970s, Davankov *et al*. first introduced the HCPs, which exhibit a more extensively crosslinked network than conventional crosslinked polystyrene.[45] HCPs was then rapidly came into routine practice by the end of the1990s.[46] The preparation of HCPs is achieved by extensive post-crosslinking of linear polystyrene networks in their swollen state via Friedel-Crafts alkylation reactions.[47] **Fig 1.6** illustrates the process involved in preparing HCPs. Initially, a linear or lightly crosslinked polystyrene precursor is stirred in a suitable solvent until it becomes swollen. Then, a Lewis-acid catalyst (e.g., $FeCl_3$ and $AlCl_3$) and an external crosslinker are added to generate crosslinks, leading to the extensive crosslinking of the polymers.[48]

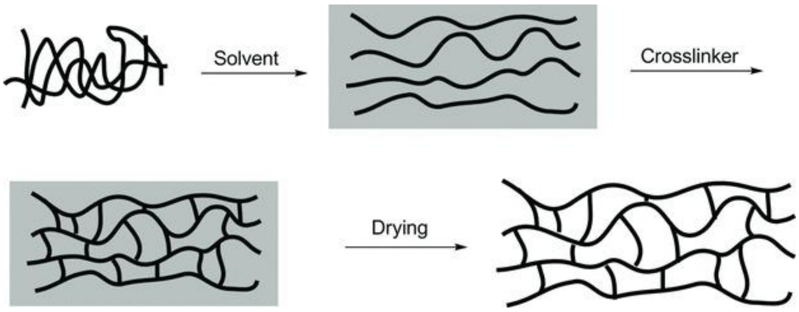

Fig 1.6 Schematic representation of post-crosslinking synthesis of HCPs.[49]

The formation of a high level of crosslinking leads to microporous structures, while the rigid networks prevent their collapse, ensuring permanent porosities, high surface areas, and large micropore volumes.[47] The inexpensive monomers, simple reactions, and mild synthesis conditions make HCPs promising candidates for addressing environmental pollution and energy challenges. As a result, HCPs have shown great potential in various catalytic and energy-related applications such as gas separation,[50] catalysis,[51] energy storage,[52] adsorption.[53]

1.3.4 Metal Organic Frameworks (MOFs)

Metal-organic frameworks (MOFs), also known as porous coordination polymers (PCPs), are a class of well-established microporous materials. MOFs are constructed from metal ions or metal clusters and organic linkers via coordination bonds, resulting a porous structure with large surface area and structuraltunability.[54-55] Depending on the geometries of the organic linkers and the coordination modes of the metal ions, their structures can be designed towards a specific application.

MOFs have a long history ,the discovery of MOFs is commonly attributed to the work of Yaghi *et al*. in 1995.[56-57] A classic example is MOF-5 (**Fig 1.7**), which consists of tetrahedral $[Zn_4O]^{6+}$ clusters connected by three 1,4-benzenedicarboxylate ligands, forming a 3D cubic network with a high surface area of 3500 m^2 g^{-1}.[58]

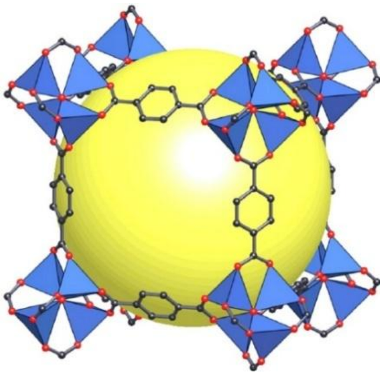

Fig 1.7 Structure of MOF-5, showing ZnO_4 tetrahedra (blue) connected by benzene dicarboxylate linkers and the resulting porosity within the framework (yellow sphere).[59] Reproduced with permission from O. M. Yaghi *et al*., Nature 2003, 423, 705–714, © 2003 Springer Nature. License ID: 6154081204523.

Since then, MOFs have rapidly gained significant research interest, leading to the development of an unlimited number of MOFs with diverse combinations of metal ions and organic linkers.[60] Among them, some well-known examples include HKUST-1, UIO-66, ZIF-8 and MIL-101, each of which exhibits unique structural features and properties. Typically, MOFs demonstrate tunable pore structure, ultrahigh porosity and incredibly large surface areas (ranging from 1000 to 10000 m^2 g^{-1}),[61-62] thus exceeding those of traditional porous materials such as zeolites and carbons. They also exhibit exceptional chemical and thermal stabilities, making them well-suited for metal-complex functionalization. Due to these unique features, MOFs have been widely exploited in applications such as gas storage and separation,[63-64] catalysis,[65] energy storage[66] and drug delivery.[67] The precise control over MOF assembly is expected to advance this field into new frontiers of synthetic chemistry, enabling access to far more sophisticated materials.[68]

1.3.5 Covalent Organic Frameworks (COFs)

Covalent organic frameworks (COFs) are another class of crystalline microporous material, constructed solely from light elements (H, B, C, N, Si and O) via covalent bonds. The first COFs (COF-1 and COF-5) were reported by Yaghi *et al.* in 2005 (**Scheme 1.8**).[69] COF-1 was synthesized through self-condensation of 1,4-benzenediboronic acid (BDBA), while COF-5 was prepared by co-condensation of 1,4-benzenediboronic acid (BDBA) and hexahydroxy triphenylene (HHTP). COF-1 and COF-5 exhibit high thermal stability (up to 500–600 °C), permanent porosity, and high surface areas (711 and 1590 m^2 g^{-1}, respectively).[69]

The topology of COFs determines their unique pore structures. Based on the dimensionality of their building units, COFs can be classified as either two-dimensional (2D) or three-dimensional (3D). The first 3D COFs were also reported by Yaghi *et al.* in 2007 (**Fig 1.9**).[70] Generally, 3D COFs can be designed using tetrahedral blocks that undergo either self-condensation or co-condensation with a triangular unit.[71] To date, most COFs exhibit 2D structures. Compared to 2D COFs, 3D COFs generally have higher surface areas and lower densities but are less common due to the limited diversity of tetrahedral building blocks.[72-73]

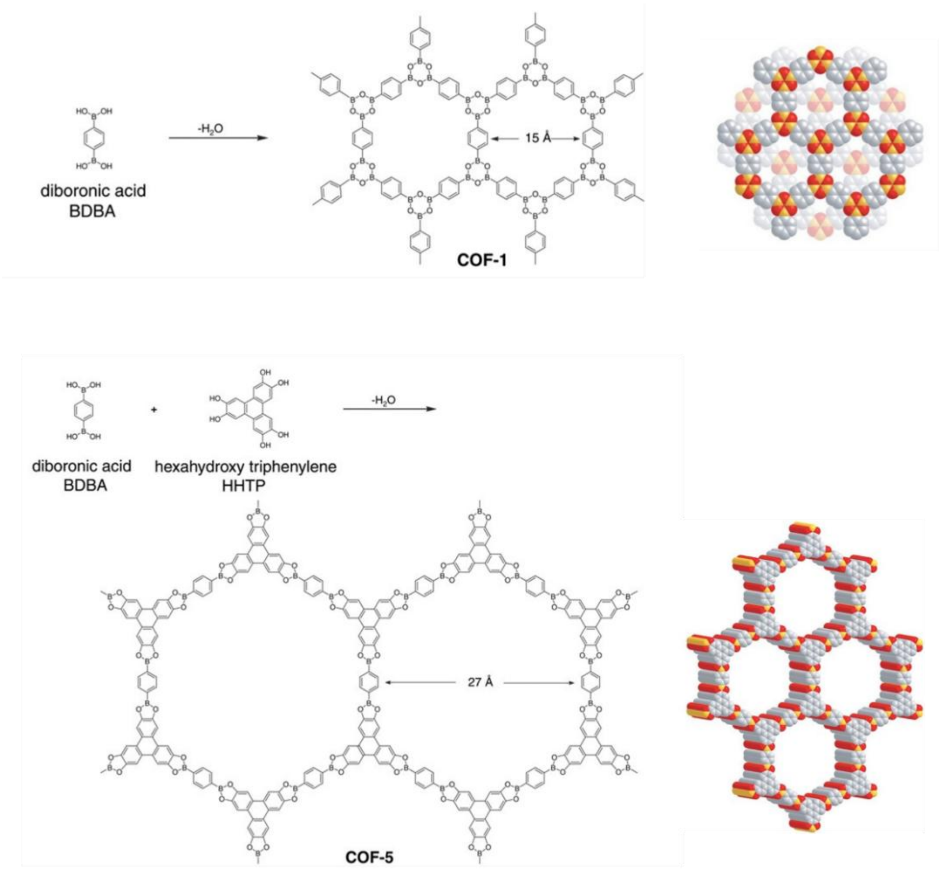

Scheme 1.8 Condensation routes and structural representations of COF-1 and COF-5.[69] Reproduced with permission from O. M. Yaghi *et al.*, Science 2005, 310, 1166–1170, © 2005 AAAS. License ID: 6154090872476.

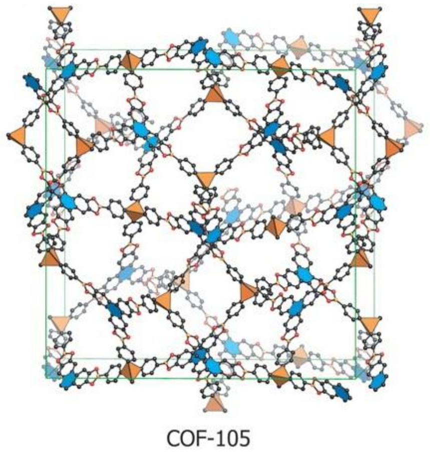

Fig 1.9 Structural representation of COF-105 with a 3D framework.[70] Reproduced with permission from H. M. El-Kaderi *et al.*, Science 2007, 316, 268-272, © 2007 AAAS. License ID: 6154091511199.

Due to their high thermal stability, permanent porosity, low mass density, and unique topology, COFs have been widely used in various applications, including gas storage and separation,[74-75] catalysis,[76] optoelectronics,[77] and sensing.[78]

1.4 Polymers of Intrinsic Microporosity (PIMs)

Polymers of Intrinsic Microporosity (PIMs) are a unique class of amorphous organic microporous materials that were first reported by McKeown *et al.* in 2004.[79] Unlike other conventional microporous materials (e.g., HCPs, MOFs, and COFs), most PIMs possess a non-network structure and are freely soluble in organic solvents.[79-80] The initial PIMs were synthesised via an aromatic nucleophilic substitution (S_NAr) reaction based on dibenzodioxin formation between a biscatechol and a tetrahalide-containing monomer. For example, the first PIM (named PIM-1) was prepared through the S_NAr reaction between the commercially available monomers 5,5',6,6'-tetrahydroxy-3,3,3',3'-tetramethyl-1,1'-spirobisindane (SBI) and 2,3,5,6-tetrafluoro-1,4-dicyanobenzene (TFTPN) (**Fig 1.10**). The reported PIM-1 was obtained as a fluorescent yellow powder and exhibited high molecular weight along with a large BET surface area (850 m^2 g^{-1}).[79]

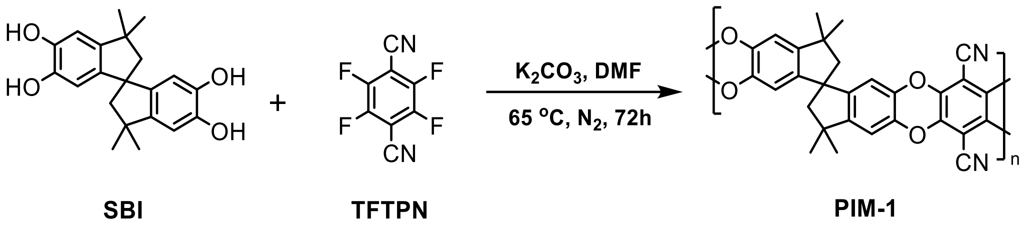

Fig 1.10 Synthesis of PIM-1.

Previously, PIMs have been defined as polymers that provide "continuous network of interconnected, intermolecular voids, which form as a direct consequence of the shape and rigidity of the component macromolecules".[81] Recently, a revised definition of a PIM was proposed as a "Polymer that is composed of a fully (or predominantly) fused-ring macromolecular chain that is fixed in a 2D or 3D random coil conformation due to sites of contortion, such as bridged bicyclic or spirocyclic units, so that they pack space inefficiently in the solid state" (**Fig 1.11**).[82]

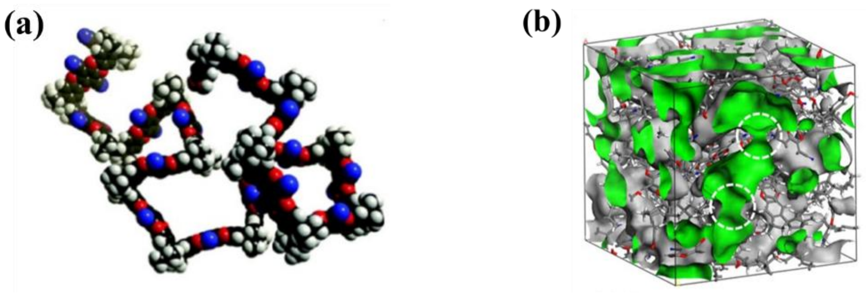

Fig 1.11 **(a)** Rigid and contorted molecular structure, and **(b)** inefficient chain packing model of PIM-1.[83-84] Reproduced with permission from N. B. McKeown, Curr. Opin. Chem. Eng. 2022, 36, 100785, © 2022 Elsevier. License ID: 6154130029950.

Generally, PIMs comprise two fundamental components: firstly, a structural unit featuring concavities that introduce a site of contortion into the polymer chain, and secondly, a linking group (e.g., dibenzodioxin linkages or imide linkages) that fuses the structural unit together during polymerisation but prohibits rotation along the polymer chain (**Fig 1.12**).[82]

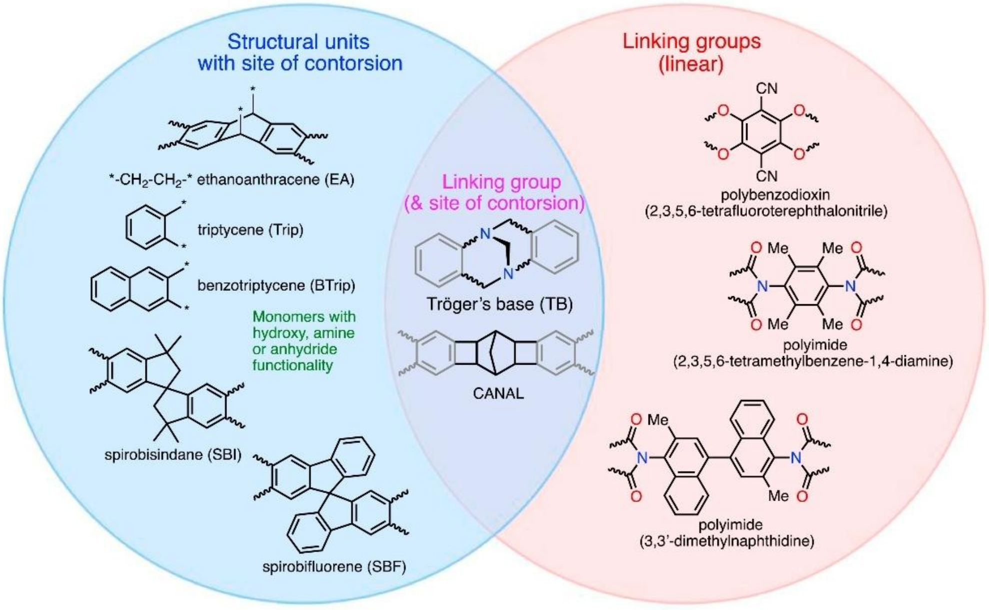

Fig 1.12 The components and modular concept of designing PIMs.[82] Reproduced with permission from N. B. McKeown, Polymer 2020, 202, 122736, © 2020 Elsevier. License ID: 6154750545055.

As an example, PIM-1, the structural unit is spirobisindane (SBI), which provides rigidity and a contorted backbone, and the linking group is a benzodioxin-based fused ring unit. A wide range of structural units have been employed to design PIMs, including spirobisindane (SBI), spirobifluorene (SBF) and highly rigid bridged bicyclic units, such as ethanoanthracene (EA), triptycene (Trip), benzotriptycene (BTrip) and Tröger's base (TB). Currently, PIMs are predominantly prepared using step-growth polymerisations based on the formation of polydibenzodioxin, polyimide, and Tröger's base (TB).[82, 85] Additionally, a new class of PIMs can be prepared using the recently developed Catalytic Arene Norbornene AnnuLation (CANAL) polymerisation.[86-87]

The unique solution-processability of PIMs allows them to be fabricated into practical forms such as films and membranes, which can serve as efficient molecular sieves, thereby offering great potential for membrane-based applications such as gas separation[80, 88] and energy storage.[89-90] Particularly, PIMs are known to be one of the top-performing materials for gas separation, due to their rigid and contorted macromolecular structures, which provide exceptionally high permeability and selectivity. Since the initial synthesis of PIMs, considerable efforts have been dedicated to expanding their structural diversity through the development of a wide range of building blocks and to continuously enhancing their gas separation performance. As a result, the gas permeability data from PIM-1and PIM-7 contributed to defining the 2008 upper bounds for multiple gas pairs due to their high permeability and moderate selectivity.[88, 91] Subsequent developments of highly ultra-microporous PIMs (e.g., PIM-EA-TB, PIM-TRIP-TB, KAUST-PI-1 and TRIM-1), fine-tuned through the incorporation of unique bridged-bicyclic units (**Fig 1.13**), have exhibited enhanced separation performance and redefined the 2015 upper bounds for H_2/N_2, O_2/N_2 and H_2/CH_4.[92-95]

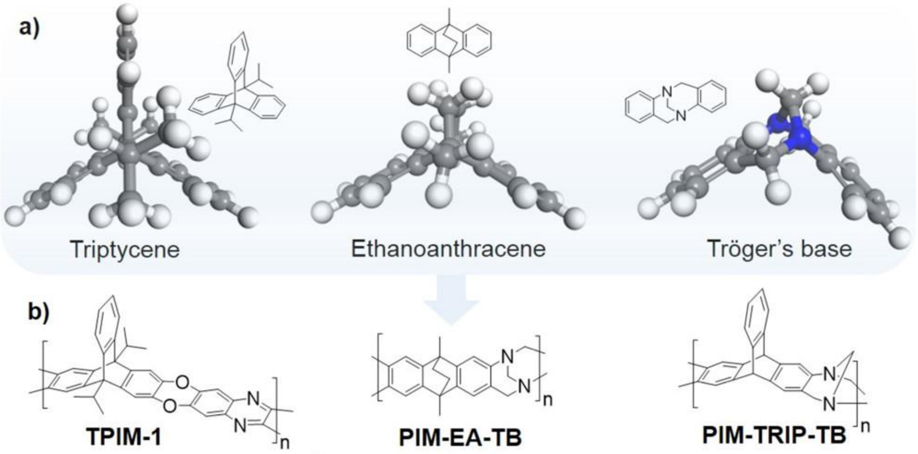

Fig 1.13 (a) Bridged-bicyclic building blocks, and **(b)** representative PIMs derived from those building blocks.[95] Reproduced with permission from R. Swaidan *et al.*, ACS Macro Lett. 2015, 4, 947-951, © 2015 American Chemical Society. License ID: 6154130879418.

In 2019, the McKeown group reported a series of ultra-permeable ladder PIMs with rigid 2D chains based on benzotriptycene (BTrip) structural units, which exhibited remarkable ideal selectivity for most gas pairs of importance due to enhanced molecular sieving resulting from increased chain rigidity.[96-97] The gas permeation properties of these benzotriptycene-based PIMs (**Fig 1.14**) redefined the most up-to-date upper bounds for CO_2/CH_4 and CO_2/N_2 separations. However, the limited solubility of these benzotriptycene-based PIMs in high-boiling-point solvents such as quinoline for fabricating self-standing films restricts their industrial applicability.

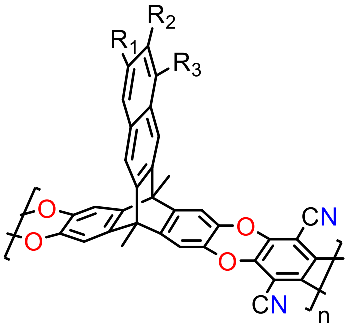

Fig 1.14 Structural representation of benzotriptycene-based PIMs.

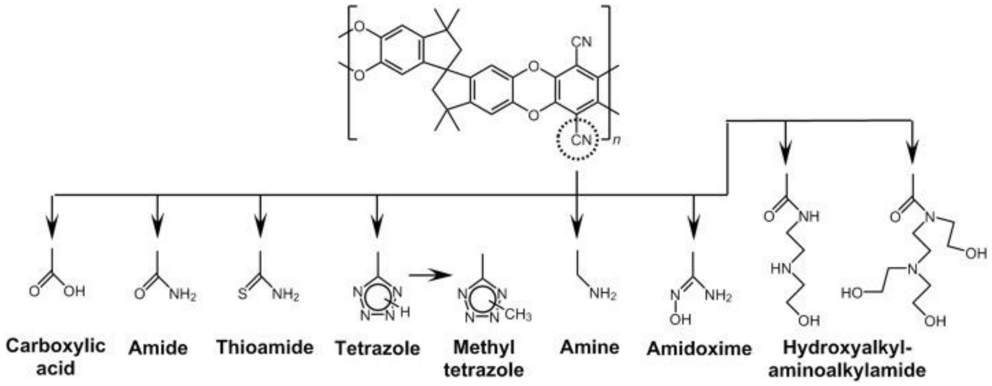

Fig 1.15 Chemical modifications of PIM-1.[98]

The unique structure of PIMs offers these organic polymers with a range of distinctive properties, including chain rigidity, large surface area, high free volume, excellent thermal stability and good solution processibility. Additionally, PIMs can be modified by the incorporation of functional groups (e.g., carboxylic acid and amine) via reactions of nitrile groups (**Fig 1.15**).[99-100] Post-polymerization modification is a useful strategy to tailor the properties and extend the structural diversity of PIMs.

1.5 Project Aims

As summarised in the previous section, PIMs show great potential as gas separation membranes due to their high free volume and intrinsic microporosity generated from their contorted and rigid polymer backbones. It has been suggested that increasing the chain rigidity of polymers could enhance their size-sieving properties, and increasing the interchain distances could increase gas permeability.[101-102] PIMs composed of rigid bridged bicyclic units such as triptycene (Trip) conform well to the PIMs design concept for generating rigid polymer backbones. Indeed, triptycene-based PIMs (e.g., PIM-Trip-TB and TPIM-1) with high selectivity redefined the 2015 upper bounds for O_2/N_2, H_2/N_2 and H_2/CH_4.[95] However, their synthesis is generally complex, typically requiring multiple reaction steps.

This project had the objective of investigating easily prepared novel bridged bicyclic monomers for the synthesis of PIMs with enhanced gas separation performance. The potential of the two triptycene-like units, naphthopleiadene (NP) and benzopleiadene (BP), was considered to investigate, as these structural units possess high rigidity and may be assembled using more accessible synthetic methods. From a historical perspective, prior to this work (and that of Amin *et al.*),[103] only the BP structural unit had been reported by Lansbury, who also suggested the nomenclature.[104] In this work, post-polymerisation modifications at the nitrile groups of PIMs were also considered to improve the gas separation performance.

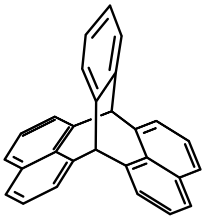

NP

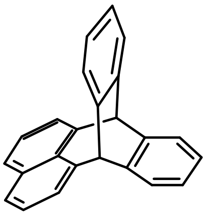

BP

Chapter 2: Synthesis of Naphthopleiadene-Based Polymers

As noted above, triptycene is a bridged bicyclic hydrocarbon composed of three benzene rings symmetrically around two sp^3-hybridized bridgehead carbons (**Figure 2.1**).[105] The unique 3D paddlewheel-like rigid structure of triptycene results in its derivatives being widely used in supramolecular chemistry[106-108] and material science.[109-111]

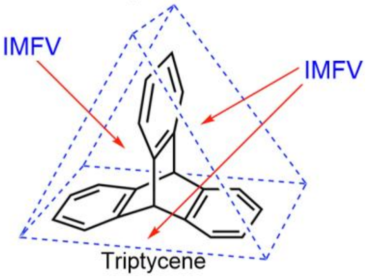

Figure 2.1 Structure of triptycene showing intramolecular free volume (IMFV).[103]

Indeed, functionalised triptycenes have attracted significant attention for the design of high-performance microporous polymers due to their large internal molecular free volume (IMFV) originating from their shape-persistent local cavities.[112-113] For example, McKeown *et al.* reported the highly microporous triptycene-based network polymer (Trip-PIMs), which exhibits a high BET surface area of up to 1605 m^2 g^{-1} and an impressive hydrogen adsorption capacity (1.83% by mass at 1 bar/77 K).[114-115] Furthermore, triptycene-based ladder polymers have shown great promise for the development of high-performance gas separation membranes.[93-94]

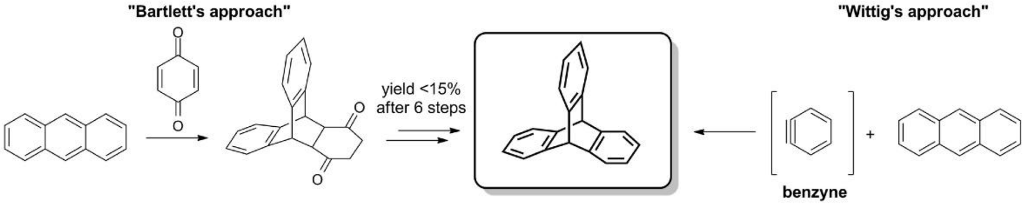

Figure 2.2 General synthetic approaches for the preparation of triptycenes.[116] Reproduced from M. Woźny et al., Molecules 2021, 27, 250, licensed under CC BY 4.0.

Despite the outstanding properties of these triptycene-derived polymers, their synthesis typically requires complex multi-step procedures, expensive reagents, and demanding purification processes.[115] Most triptycene derivatives are still prepared via the Diels–Alder reaction (**Figure 2.2**) between anthracenes and a reactive benzyne intermediate (Wittig's approach) or an appropriate dienophile (Bartlett's approach).

Amin *et al*. from the McKeown group recently introduced a new class of triptycene-like compounds known as naphthopleiadenes (NPs).[103] These compounds feature a unique bridged bicyclic framework with in-built hydroxyl functionality (**Figure 2.3**). Their structures consist of a single benzene ring and two naphthalene units fused via two bridging carbon atoms. The NPs possess a larger intramolecular free volume (IMFV) than triptycene due to the greater width of their naphthalene units. Unlike typical triptycene derivatives that require multi-step synthesis, NPs can be readily prepared via a simple one-step reaction from commercially available 2,7-dihydroxynaphthalene and phthalaldehyde. The readily prepared NPs combined with their unique structures demonstrate great potential for use in polymers.[103]

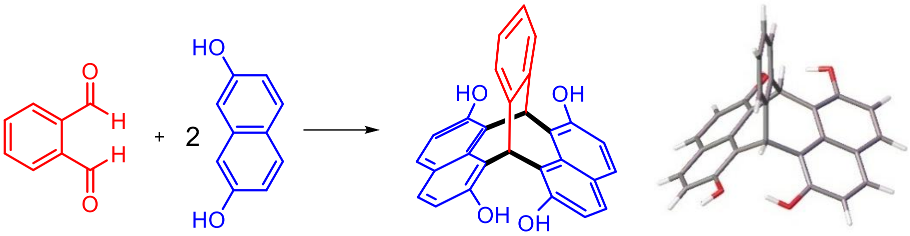

Figure 2.3 Synthesis of naphthopleiadene (NP) and its crystal structure (CCDC 2286805).[103]

As described previously in **Section 1.4**, PIMs based on triptycene derivatives exhibited excellent gas separation performance due to their highly rigid polymer backbones. Therefore, NPs, which possess bulkiness and rigidity comparable to those of traditional triptycenes, provide a useful structural unit for the preparation of PIMs used in gas separation membranes. Amin *et al*. reported that polymers derived from the NPs (**Figure 2.4**) exhibit a high average molecular weight ($M_n = 140{,}000\ \mathrm{g\ mol^{-1}}$).[103] However, films of NP-based PIMs cast from DMF solutions were too fragile to be used for gas permeability measurements. In this chapter, a series of functionalised NP monomers was prepared from 2,7-dihydroxynaphthalene and various aromatic 1,2-dialdehydes. To further investigate the gas separation performance of NP-based polymers, copolymers incorporating these functionalised NP monomers with PIM-1 were prepared.

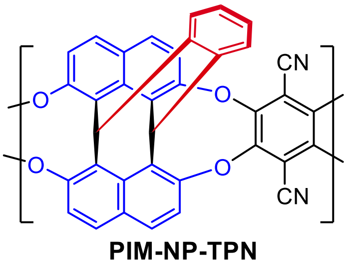

Figure 2.4 Chemical structure of the NP-based polymer PIM-NP-TPN.[103]

2.1 Synthesis of NP monomers (NPs)

Acid-mediated reactions between phthalaldehyde and electron-rich aromatic compounds were considered for the synthesis of triptycene derivatives. However, these reactions appear to afford 9-phenyl anthracenes via a six-membered-ring carbocation intermediate.[117-119] Our recently published study demonstrated that triptycene-like compounds can be readily prepared via the acid-mediated double addition of 2,7-disubstituted naphthalene units to aromatic 1,2-dialdehydes, in which the formation of a seven-membered ring carbocation intermediate prevents subsequent aromatization.[103] Beginning from commercially available starting materials, the initial NP monomer was obtained in high yield (70%) by heating a mixture of 2,7-dihydroxynaphthalene and phthalaldehyde in acidified methanol. In this work, a further three substituted-NP monomers were synthesised by replacing phthalaldehyde with 4,5-disubstituted-1,2-benzenedialdehydes in the reaction, while adjusting the reaction conditions according to the reactivity of the respective dialdehyde precursors.

Synthesis of benzo-substituted naphthopleiadene (BNP)

The precursor, 2,3-naphthalenedialdehyde **(1)**, was synthesised through a one-pot reaction following the reported procedure (**Scheme 2.1**).[120] The dialdehyde **(1)** was prepared by condensation of phthalaldehyde with butanedial, which was generated in situ from the hydrolysis of 2,5-dimethoxytetrahydrofuran. 2,3-Naphthalenedialdehyde **(1)** was purified by sublimation at 130 °C, affording a yield of 25%.

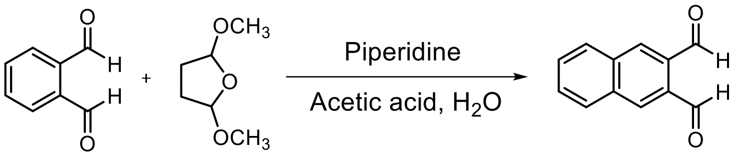

(1)

Scheme 2.1 Synthesis of 2,3-naphthalenedialdehyde **(1)**.

After the successful synthesis of 2,3-naphthalenedialdehyde **(1)**, its subsequent reaction with 2,7-dihydroxynaphthalene was conducted to obtain its corresponding naphthopleiadene (NP) derivative (**Scheme 2.2**). An initial attempt was carried out following the procedure described by Amin *et al.*, in which all starting materials were dissolved in methanol with several drops of conc. HCl. However, this condition afforded the benzo-substituted naphthopleiadene (BNP) **(2)** in very low yield. It was found that increasing the amount of conc. HCl led to the formation of the BNP **(2)** structure with a high yield of 90%. Single crystals of the synthesised BNP **(2)** were obtained via recrystallisation from methanol by slow cooling.

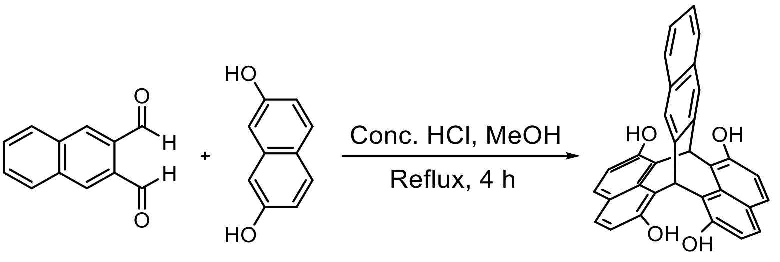

BNP (2)

Scheme 2.2 Synthesis of benzo-substituted naphthopleiadene (BNP) **(2)**.

The product was analysed by ^{1}H NMR spectroscopy, where the presence of characteristic bridgehead protons at 7.08 ppm strongly indicates the successful formation of the BNP **(2)** structure (**Figure 2.5**). And a singlet at 9.96 ppm represents aromatic hydroxyl groups (Ar-OH). The X-ray crystal structure (**Figure 2.6**) provides further confirmation of the bridged bicyclic structure of BNP **(2)**.

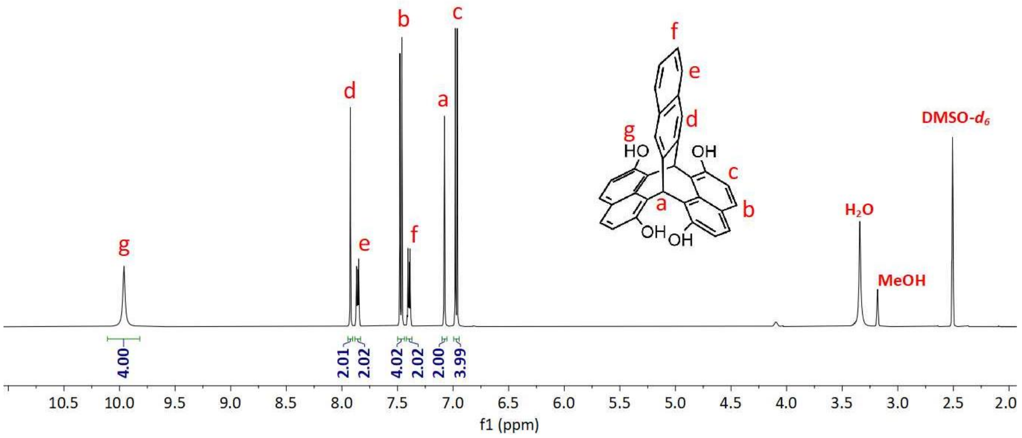

Figure 2.5 ^{1}H NMR of benzo-substituted naphthopleiadene (BNP) **(2)**.

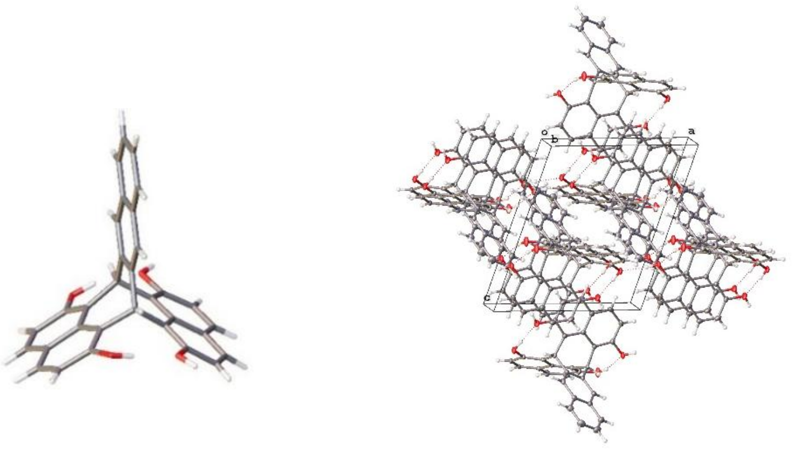

Figure 2.6 X-ray crystal structure (CCDC 2286808) and molecular packing of (BNP) **(2)**. The crystal packing image shows the hydrogen bonding interactions between hydroxyls (red) in the solid state.

Synthesis of dimethoxy-substituted naphthopleiadene (DMNP)

The precursor, 4,5-dimethoxyphthalaldehyde **(5)** was synthesised starting from commercially available 3,4-dimethoxybenzoic acid, prepared through a three-step synthesis following the reported procedure (**Scheme 2.3**).[121] 3,4-Dimethoxybenzoic acid was converted into a lactone **(3)** via an acid-catalysed cyclisation reaction with formaldehyde. The desired dialdehyde **(5)** was prepared by reduction of the lactone **(3)**, followed by Swern oxidation of the resulting alcohol **(4)**.

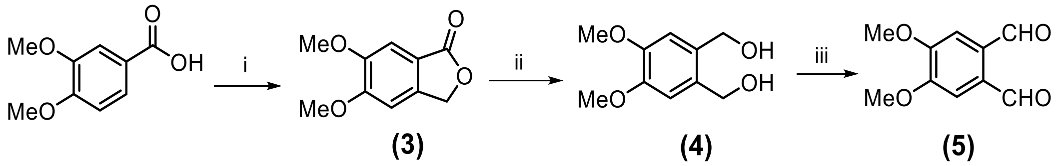

Scheme 2.3 Synthesis of 4,5-dimethoxyphthalaldehyde **(5)**. i) Paraformaldehyde, conc. HCl, 80 °C, 6 h; ii) $LiAlH_4$, dry THF, reflux, 4 h; iii) oxalyl chloride, DMSO, TEA, dry DCM, -78 °C, 60 min → rt, 60 min.

After the successful synthesis of 4,5-dimethoxyphthalaldehyde **(5)**, the subsequent reaction with 2,7-dihydroxynaphthalene was investigated to obtain its corresponding naphthopleiadene (NP) derivative (**Scheme 2.4**). Initial attempts to react 4,5-dimethoxyphthalaldehyde **(5)** with 2,7-dihydroxynaphthalene were performed in methanol with conc. HCl as the catalyst. However, no reaction was observed, even in the presence of a large excess of conc. HCl. Finally, DMNP **(6)** was successfully obtained, with a yield of 75%, in strongly acidic conditions using a mixture of acetic acid (AcOH) and triflic acid (TFSA). No reaction was observed in a further comparison using AcOH and conc. HCl (**Table 2.1**). Single crystals of the synthesised DMNP **(6)** were obtained via recrystallisation from a mixture of acetone and methanol by slow evaporation.

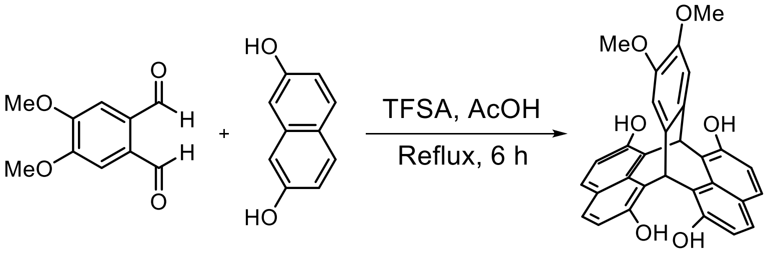

DMNP (6)

Scheme 2.4 Synthesis of dimethoxy-substituted naphthopleiadene (DMNP) **(6)**.

The product was analysed by ^{1}H NMR spectroscopy, where the presence of characteristic bridgehead protons at 6.65 ppm strongly indicates the successful formation of the DMNP **(6)** structure (**Figure 2.7**). The X-ray crystal structure (**Figure 2.8**) provides further confirmation of the bridged bicyclic structure of DMNP **(6)**.

Table 2.1 Optimisation of reaction conditions to synthesise DMNP **(6)**.

Solvent	Catalyst	Temperature	Yield (%)
MeOH	Conc. HCl (3 drops)	Reflux	N
MeOH	Conc. HCl (1 ml)	Reflux	N
AcOH	Conc. HCl (1 ml)	Reflux	N
AcOH	TFSA (3 drops)	Reflux	50 %
AcOH	TFSA (0.1 ml)	Reflux	75 %

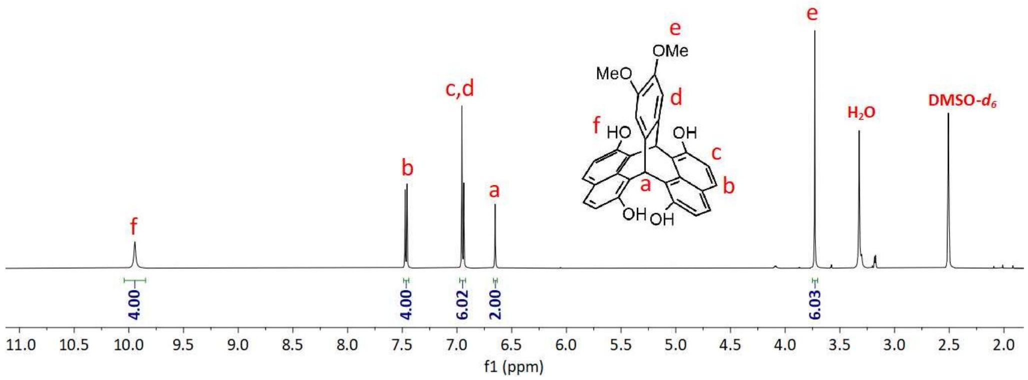

Figure 2.7 ^{1}H NMR of dimethoxy-substituted naphthopleiadene (DMNP) **(6)**.

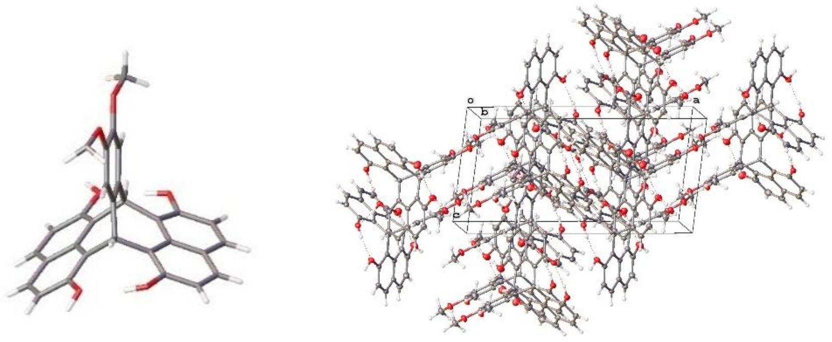

Figure 2.8 X-ray crystal structure and molecular packing of (DMNP) **(6)**. The crystal packing image shows the hydrogen bonding interactions between hydroxyls (red) in the solid state.

Synthesis of triethylene glycol monomethyl ether (TEG)-substituted naphthopleiadene (TEGNP)

The precursor, 4,5-diTEG-phthalaldehyde **(11)**, was synthesized following a procedure similar to that used for 4,5-dimethoxyphthalaldehyde **(5)**. The synthesis began with the etherification of 5,6-dihydroxy-1(3H)-isobenzofuranone **(7)** using triethylene glycol monomethyl ether

(TEG) **(8)** in the presence of K_2CO_3 and DMF (**Scheme 2.5**). The 4,5-diTEG-phthalaldehyde **(11)** was then prepared by reduction of the TEG-functionalised lactone **(9)**, followed by Swern oxidation of the resulting alcohol **(10)**. The dialdehyde **(11)** was isolated by column chromatography as a colorless oil.

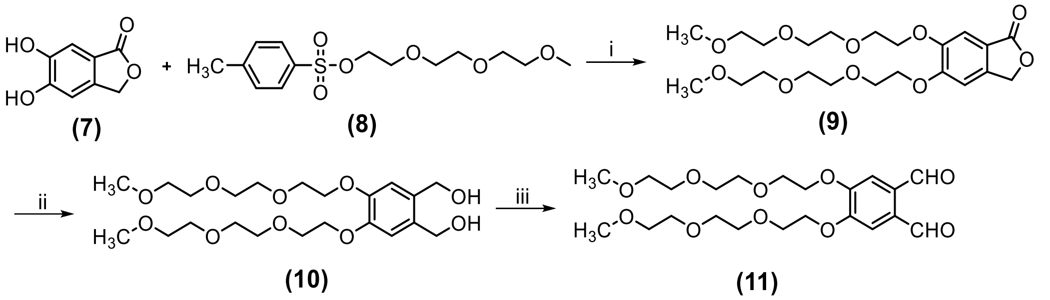

Scheme 2.5 Synthesis of 4,5-dimethoxyphthalaldehyde **(11)**. i) K_2CO_3, DMF, 90 °C, 12 h; ii) $LiAlH_4$, dry THF, reflux, 4 h; iii) oxalyl chloride, DMSO, TEA, dry DCM, -78 °C, 60 min → rt, 60 min.

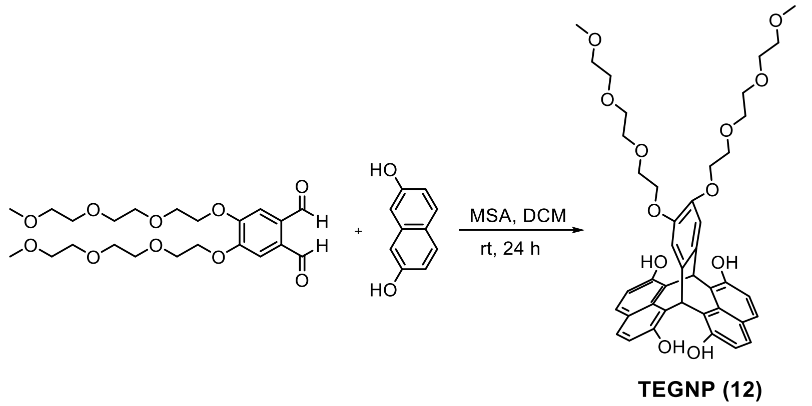

Scheme 2.6 Synthesis of triethylene glycol monomethyl ether-substituted naphthopleiadene (TEGNP) **(12)**.

Triethylene glycol monomethyl ether (TEG)-substituted naphthopleiadene (TEGNP) **(12)** was synthesised in the presence of methanesulfonic acid (MSA) and DCM (**Scheme 2.6**). TEGNP **(12)** was obtained as an orange solid characterised by a lower melting point (80 °C) compared to other NPs (> 300 °C).

The product was analysed by ^{1}H NMR spectroscopy, where the presence of characteristic bridgehead protons at 6.64 ppm strongly indicates the successful formation of the TEGNP **(12)** structure (**Figure 2.9**). And a singlet at 9.93 ppm represents aromatic hydroxyl groups (Ar-OH).

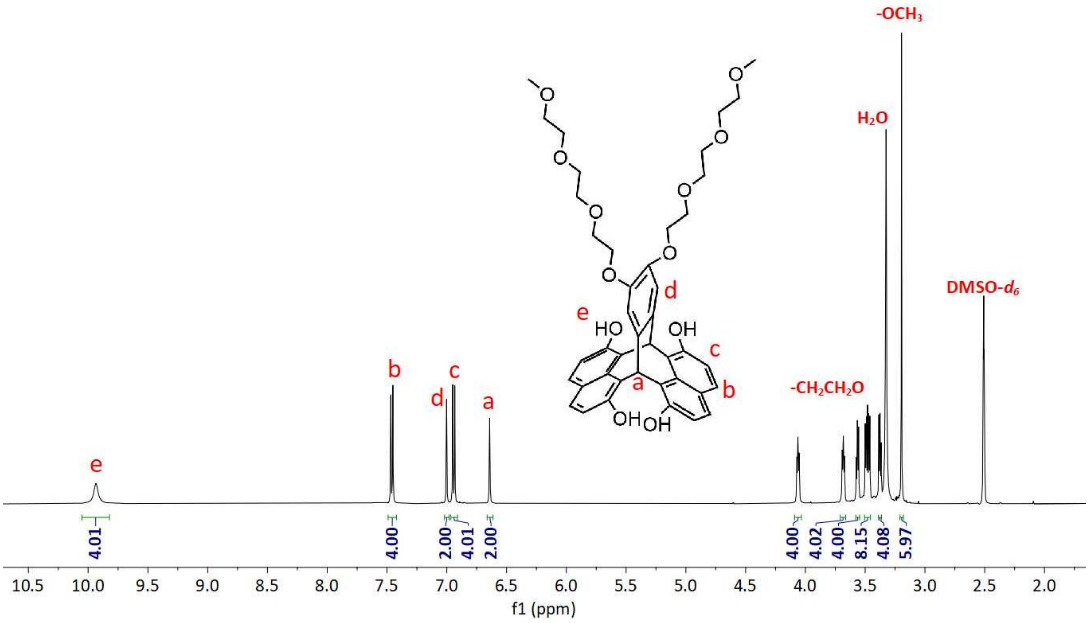

Figure 2.9 ^{1}H NMR of triethylene glycol monomethyl ether-substituted naphthopleiadene (TEGNP) **(12)**.

2.2 Synthesis of NP-based copolymers (PIM-NPs)

Amin *et al*. reported the synthesis of a non-network polymer (PIM-NP-TPN) by reacting the initial NP with an equimolar amount of commercially available 2,3,5,6-tetrafluorophthalonitrile (TFTPN) in the presence of K_2CO_3 and dry DMF at 65 °C for 72 h under nitrogen protection (**Scheme 2.7**).[103] However, films of PIM-NP-TPN cast from DMF solutions were too fragile to be used for gas permeability measurements. This poor film-forming property was possibly due to the excessive rigidity of the tribenzo-1,4-dioxonine linking group.[103]

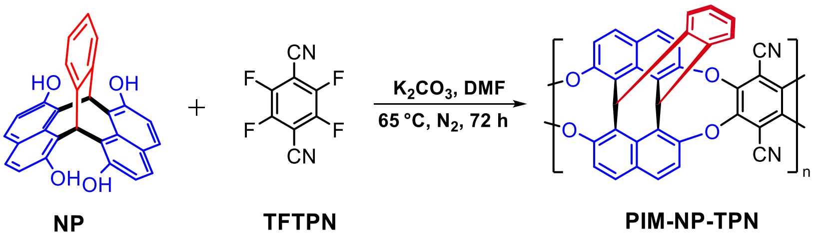

Scheme 2.7 Synthesis of PIM-NP-TPN.

In an attempt to explore the effect of NP units on the performance of gas separations, a series of NP-based copolymers were synthesised by reacting functionalised NPs and TTSBI (the monomer used for PIM-1) with TFTPN at varying molar ratios. These copolymers are denoted as PIM-BNP$_x$, PIM-DMNP$_x$ and PIM-TEGNP$_x$, where "x" represents the molar ratios of NPs relative to TTSBI (**Scheme 2.8**). The polymerisation conditions for copolymers with varying monomer ratios were the same as those used for homopolymer PIM-NP-TPN.

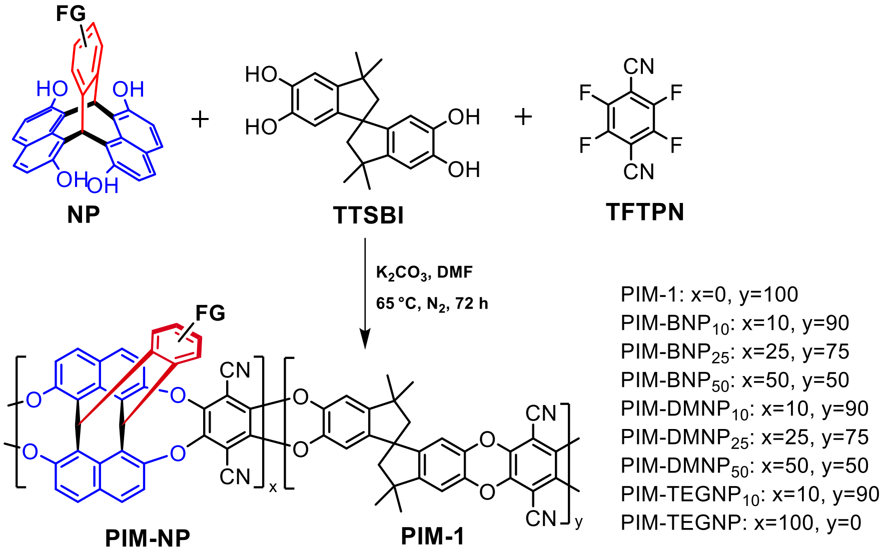

Scheme 2.8 Synthesis of copolymers, PIM-BNP$_x$, PIM-DMNP$_x$ and PIM-TEGNP$_x$.

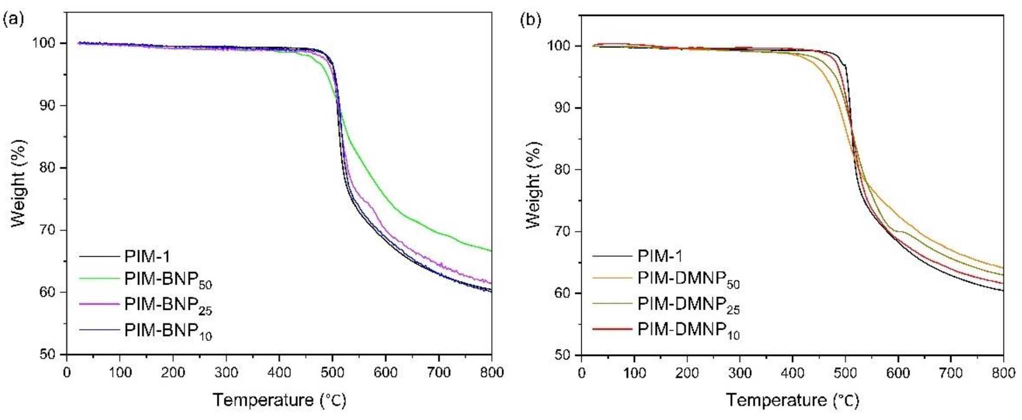

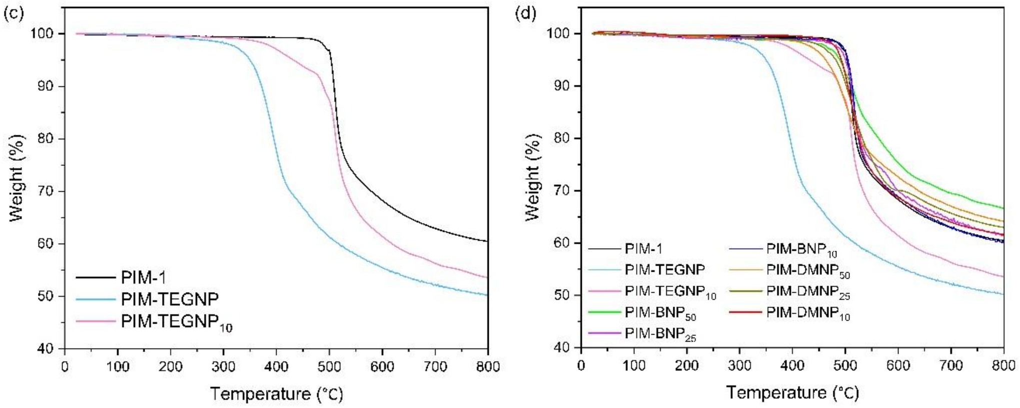

Figure 2.10 TGA analysis of (a) PIM-BNP$_x$, (b) PIM-DMNP$_x$, (c) PIM-TEGNP$_x$, and (d) an overall comparison of these copolymers.

Thermal gravimetric analysis (TGA) of copolymers PIM-BNP$_x$, PIM-DMNP$_x$, PIM-TEGNP$_x$ and PIM-1 are shown in **Fig 2.10**. For copolymers PIM-BNP$_x$ and PIM-DMNP$_x$, increasing the content of BNP or DMNP monomer results in lower weight loss at 800 °C (**Fig 2.10a and b**). In contrast, the homopolymer PIM-TEGNP and copolymer PIM-TEGNP$_{10}$ show higher weight loss at 800 °C than PIM-1 (**Fig 2.10c**). As observed from **Fig 2.10d**, the copolymers PIM-BNP$_x$ and PIM-DMNP$_x$ exhibit higher thermal stability than PIM-TEGNP and PIM-TEGNP$_{10}$.

2.3 Physical properties and microporosity analysis

The physical properties of copolymers PIM-BNP$_x$, PIM-DMNP$_x$ and PIM-TEGNP$_x$ are summarised in **Table 2.2** for comparison. The copolymers containing 10% of BNP, DMNP, or TEGNP units each have good solubility in $CHCl_3$. When BNP or DMNP contents exceed 10%, the copolymers are only soluble in high boiling point solvents such as NMP. Additionally, the homopolymer PIM-TEGNP are soluble in DMF or DMSO.

Copolymers with lower contents of BNP, DMNP or TEGNP (≤ 25 mol%) resulted in robust self-standing films, as shown in **Fig 2.11**. And copolymers with a content of BNP or DMNP (50 mol%) were also able to form self-standing films, but these films could not survive the methanol treatment, making them unsuitable for gas permeability measurement. The brittle film formation of PIM-BNP$_{50}$ and PIM-DMNP$_{50}$ can be attributed to the high fraction of highly rigid NP units, which restricts the mobility of the polymer chains. The homopolymer PIM-TEGNP shows very poor film-forming property and gives only small, fragile pieces. The prepared films of these copolymers have been to Institute on Membrane Technology, National Research Council of Italy (CNR-ITM) for gas separation studies.

Table 2.2 physical properties of copolymers

Polymer	Yield (%)	Solubility	SA_{BET}[a] (m^2 g^{-1})	V_{Total}[b] (ml g^{-1})	CO_2 uptake[c] (mmol g^{-1})
PIM-1	97%	$CHCl_3$	709	0.55	2.19
PIM-BNP$_{10}$	95%	$CHCl_3$	728	0.52	2.05
PIM-BNP$_{25}$	97%	NMP	741	0.54	2.54
PIM-BNP$_{50}$	97%	NMP	733	0.48	2.36
PIM-DMNP$_{10}$	98%	$CHCl_3$	666	0.47	2.10
PIM-DMNP$_{25}$	96%	NMP	699	0.59	2.28
PIM-DMNP$_{50}$	97%	NMP	683	0.56	2.23
PIM-TEGNP$_{10}$	90%	$CHCl_3$	559	0.34	2.06
PIM-TEGNP	92%	DMF, DMSO	0.18	0.005	0.34

[a] BET surface area (SA_{BET}) was calculated from N_2 adsorption isotherm obtained at 77 K. [b] Total pore volume (V_{Total}) was estimated from N_2 adsorption at $P/P_o = 0.98$. [c] CO_2 uptake at 1 bar and 273 K.

PIM-BNP$_{10}$ **PIM-BNP$_{25}$** **PIM-BNP$_{50}$** **PIM-DMNP$_{10}$**

PIM-DMNP$_{25}$ **PIM-DMNP$_{50}$** **PIM-TEGNP$_{10}$** **PIM-TEGNP**

Figure 2.11 Films of copolymers, PIM-BNP$_x$, PIM-DMNP$_x$ and PIM-TEGNP$_x$.

The N_2 adsorption-desorption isotherms of synthesised polymers are presented in **Fig 2.12**. All copolymers PIM-BNPx, PIM-DMNPx, and PIM-TEGNP$_x$ exhibit high N_2 uptake at low relative pressure (P/Po < 0.1), indicating significant microporosity, whereas the homopolymer PIM-TEGNP shows negligible N_2 uptake, suggesting a non-porous structure. Among them, copolymers with 10% contents of BNP, DMNP or TEGNP show reduced N_2 adsorption capacity than PIM-1. The shapes of the N_2 isotherms are similar for all these copolymers, with distinct hysteresis between the adsorption and desorption isotherms, which can be attributed to swelling of the polymer during N_2 adsorption. Most copolymers exhibit similar BET surface areas (SA_{BET}) in the range of 666 - 741 m^2 g^{-1} and are comparable to that of PIM-1, whereas the copolymer PIM-TEGNP$_{10}$ shows a lower SA_{BET} of 559 m^2 g^{-1} (**Table 2.2**). For the homopolymer PIM-TEGNP, the SA_{BET} (0.18 m^2 g^{-1}) is extremely low, indicating a non-porous structure.

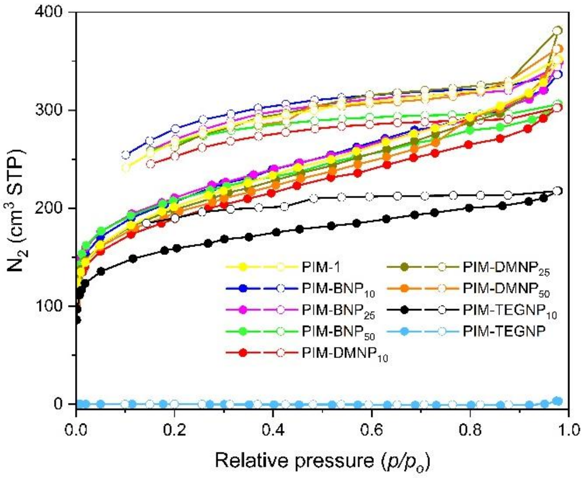

Figure 2.12 N_2 adsorption (filled circle) and desorption (open circle) isotherms of copolymers PIM-BNP$_x$, PIM-DMNP$_x$, PIM-TEGNP$_x$ and PIM-1.

Fig 2.13 illustrates the CO_2 adsorption isotherms at 273 K for the polymers, and their pore size distribution (PSD) were calculated using the density functional theory (DFT) model. Copolymers containing a low fraction of NP units (PIM-BNP$_{10}$, PIM-DMNP$_{10}$ and PIM-TEGNP$_{10}$) demonstrate a reduced CO_2 uptake compared to PIM-1(**Fig 2.13a**). With a higher content of NP units (≥ 25 %), the copolymers exhibit higher CO_2 uptake than PIM-1, indicating a greater concentration of ultra-micropores (< 0.7 nm) (**Fig 2.13b**). However, the homopolymer PIM-TEGNP with a non-porous structure shows much lower CO_2 adsorption capacity.

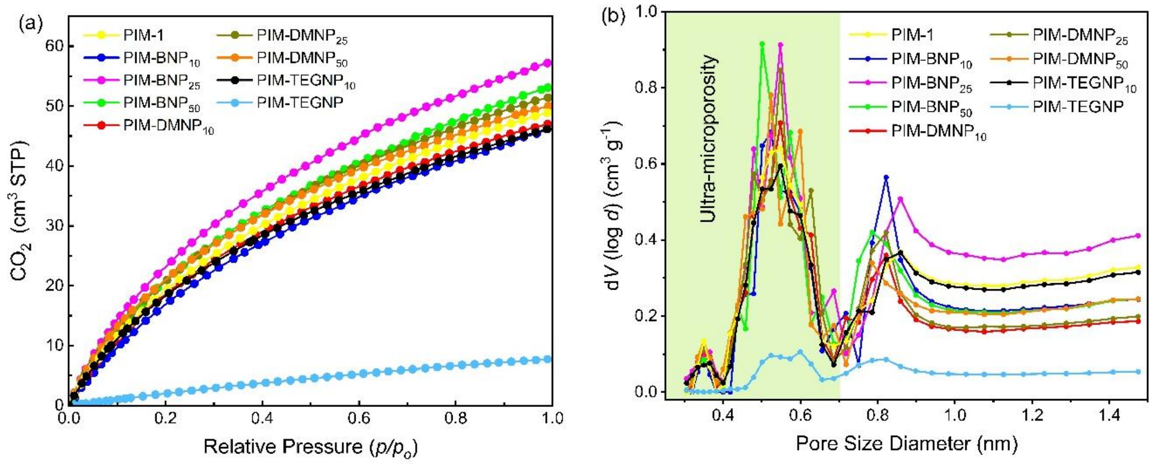

Figure 2.13 (a) CO_2 adsorption isotherms of copolymers, PIM-BNP$_x$, PIM-DMNP$_x$, PIM-TEGNP$_x$ and PIM-1 and (b) their pore size distributions (PSD) calculated from CO_2 adsorption data using non-local density functional theory (NLDFT) model.

Chapter 3: Synthesis of Benzopleiadene-based Polymers

Triptycene-derived ladder polymers exploit the rigidity and internal molecular free volume (IMFV) of triptycene derivatives, which makes them promising candidates for high-performance gas separation membranes.[122] Indeed, McKeown *et al.* proposed the latest revision for the important CO_2/CH_4 and CO_2/N_2 upper bounds using data from ultrapermeable and highly selective 2D ribbon-shaped benzotriptycene-based ladder polymers (PIM-TMN-Trip and PIM-Btrip).[96-97] However, most triptycene derivatives used as scaffolds for these ladder polymers are still predominantly prepared via the Diels–Alder reaction between a prefunctionalised anthracene and an appropriate dienophile, such as PIM-BTrip-TB[123] and PIM-Btrip[97]. Consequently, their synthesis generally requires multistep reactions involving high temperatures and expensive reagents (**Scheme 3.1**).

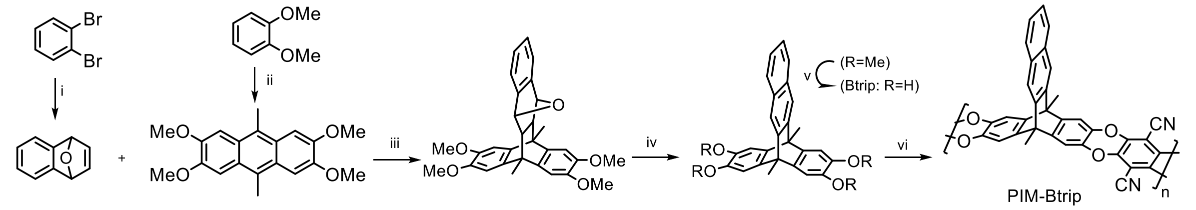

Scheme 3.1 Synthesis of PIM-Btrip. i. *n*-BuLi, furan, THF, -78 °C, 1.5 h; ii. Acetaldehyde, *c*H_2SO_4, CH_3CN, 0 °C, 2 h; iii. DMF, 250 °C, 7 bar, 2 h, microwave irradiation; iv. TFA, rt, 24 h; v. BBr_3, DCM; vi. 2,3,5,6-Tetrafluoropthalonitrile, K_2CO_3, DMF, 65 °C, 96 h.

Motivated by our long-term interest in identifying useful rigid structural units for the construction of PIMs, here we report a simple, one-step synthesis of a benzopleiadene (BP) compound, which features a novel bridged bicyclic framework composed of two catechol units and a single naphthalene core fused at two bridgehead carbon centres. BP exhibits a highly rigid structure and well-defined concavities, which provide intermolecular free volume (IMFV) comparable to that of benzotriptycene (Btrip). In addition, the readily prepared BP compound possesses in-built hydroxyl functionality, allowing for its direct utilization in subsequent synthesis of ladder polymers based on dibenzodioxin formation. In this chapter, BP-based PIMs and their properties will be discussed.

3.1 Synthesis of BP-based polymers (PIM-BP)

3.1.1 Synthesis of BP monomer

Acid-mediated reactions between phthalaldehyde and electron-rich aromatic compounds were considered for the synthesis of triptycene derivatives. However, these reactions appear to afford 9-phenyl anthracenes via a six-membered-ring carbocation intermediate.[117-119] As described in previous chapter, our recently study demonstrated that triptycene-like compounds can be readily prepared via the acid-mediated double addition of 2,7-disubstituted naphthalene units to aromatic 1,2-dialdehydes, in which the formation of a seven-membered ring carbocation intermediate prevents the subsequent aromatization.[103] To further explore the generality of this synthetic strategy, we proposed a reverse design by swapping the electron-rich and electrophilic components, in which the electron-donating groups are introduced onto the benzene ring, while the aldehyde functionalities are incorporated into the naphthalene scaffold. On consideration of this mechanism, it was anticipated that a benzopleiadene (BP) compound with in-built tetra-hydroxyl functionality could be formed via the double addition of catechol to 1,8-naphthalene dialdehyde (**Scheme 3.2**).

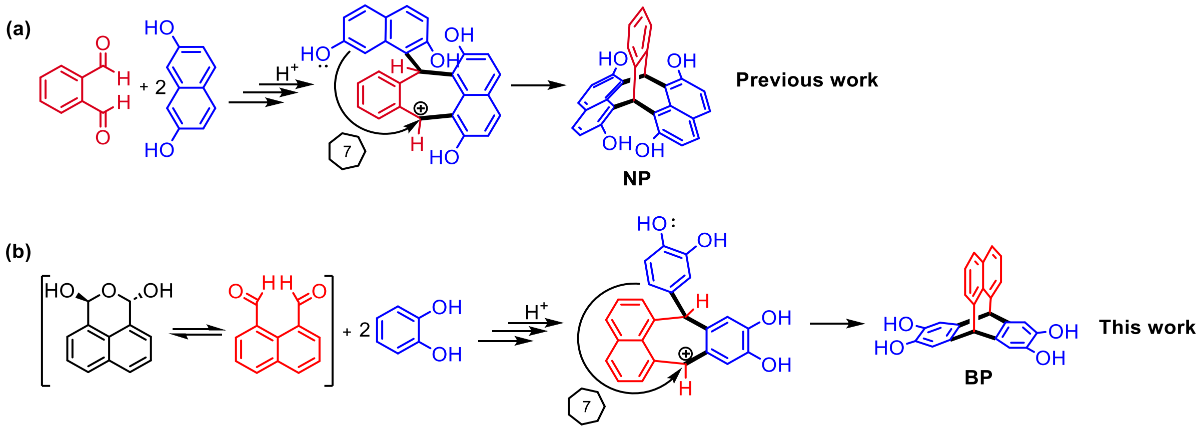

Scheme 3.2 Proposed partial reaction mechanisms for the formation of (a) naphthopleiadene (NP) from phthalaldehyde and 2,7-dihydroxynaphthalene via a seven-membered ring carbocation intermediate,[103] and (b) benzopleiadene (BP) from 1,8-naphthalenedialdehyde hydrate and catechol.

The newly designed monomer 9,10,14,15-tetrahydroxybenzopleiadene (**BP**) **(15)** was prepared by refluxing a mixture of 1,8-naphthalene dialdehyde hydrate **(14)** and catechol in acetic acid in the presence of concentrated H_2SO_4 (**Scheme 3.3**). The required dialdehyde hydrate precursor **(14)** was efficiently obtained via sodium borohydride reduction of acenaphthoquinone,[124] followed by Criegee oxidation of the resulting diol **(13)** using lead tetraacetate.[125] BP **(15)** was isolated via silica gel column chromatography with a yield of 35%. Single crystals of the synthesised BP **(15)** were obtained via recrystallisation from a mixture of acetone and toluene by slow evaporation.

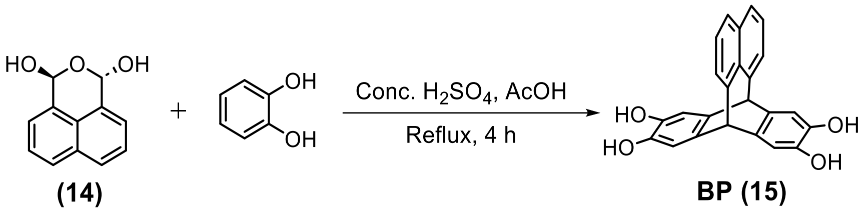

Scheme 3.3 Synthesis of 9,10,14,15-tetrahydroxybenzopleiadene (BP) **(15)**.

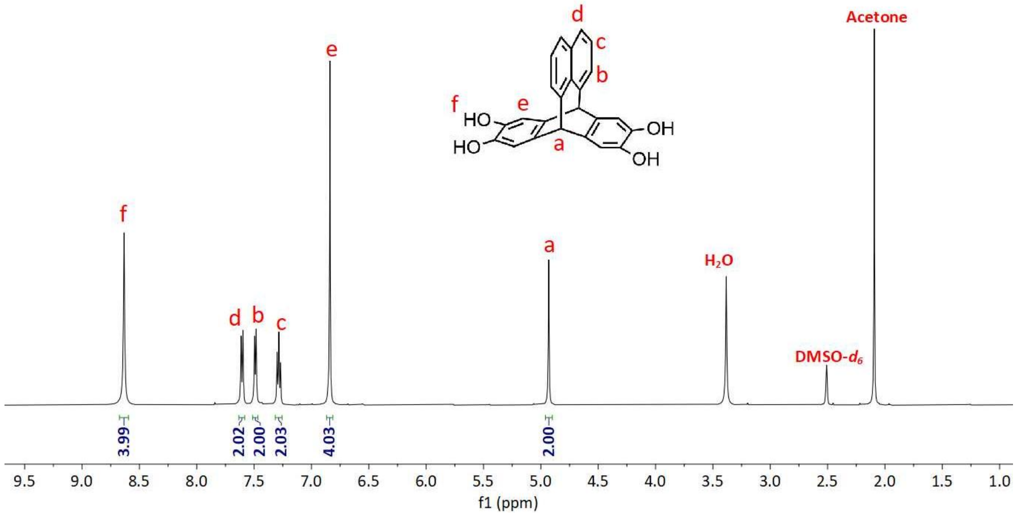

Figure 3.1 ^1H NMR of 9,10,14,15-tetrahydroxybenzopleiadene (BP) **(15)**.

The product was analysed by ^1H NMR spectroscopy, where the presence of characteristic bridgehead protons at 4.93 ppm strongly indicates the successful formation of the BP **(15)** structure (**Figure 3.1**). And a singlet at 8.63 ppm represents aromatic hydroxyl groups (Ar-OH).

The X-ray crystal structure (**Figure 3.2**) provides further confirmation of the bridged bicyclic structure of BP **(15)**.

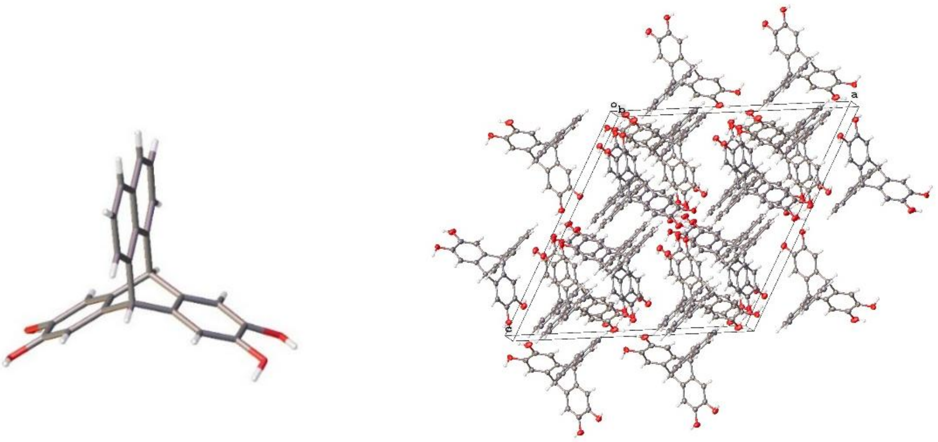

Figure 3.2 X-ray crystal structure and molecular packing of 9,10,14,15-tetrahydroxybenzopleiadene (BP) **(15)**. The crystal packing image shows the hydrogen bonding interactions between hydroxyls (red) in the solid state.

3.1.2 Synthesis of BP-based polymers (PIM-BP)

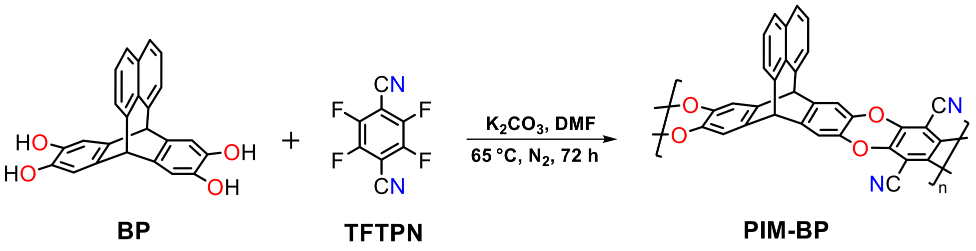

Scheme 3.4 Structure and synthesis of PIM-BP.

In this work, a polymer (PIM-BP) (**Scheme 3.4**) was prepared from the synthesised BP **(15)** monomer and 2,3,5,6-tetrafluoroterephthalonitrile (TFTPN) via the well-established polymerisation based on the formation of dibenzodioxin linkages, which have been commonly used in PIM synthesis. However, PIM-BP was found to be soluble only in high boiling point solvents such as quinoline. Though robust self-standing films of PIM-BP were successfully cast from its quinoline solution, quinoline is not an ideal solvent due to its high toxicity, strong and persistent smell, and the difficulty of complete removal during post-processing. These drawbacks limit its practical applicability, especially in large-scale or environmentally sensitive membrane fabrication.

To address this limitation, a series of copolymers composed of BP **(15)**, commercially available TTSBI (the monomer used for PIM-1) and TFTPN were synthesised in a one-step polycondensation reaction. These copolymers are denoted as PIM-BP$_x$, where "x" represents the molar ratios of BP **(15)** relative to TTSBI (**Scheme 3.5**). The polymerisation conditions for copolymers with varying monomer ratios were the same as those used for PIM-BP.

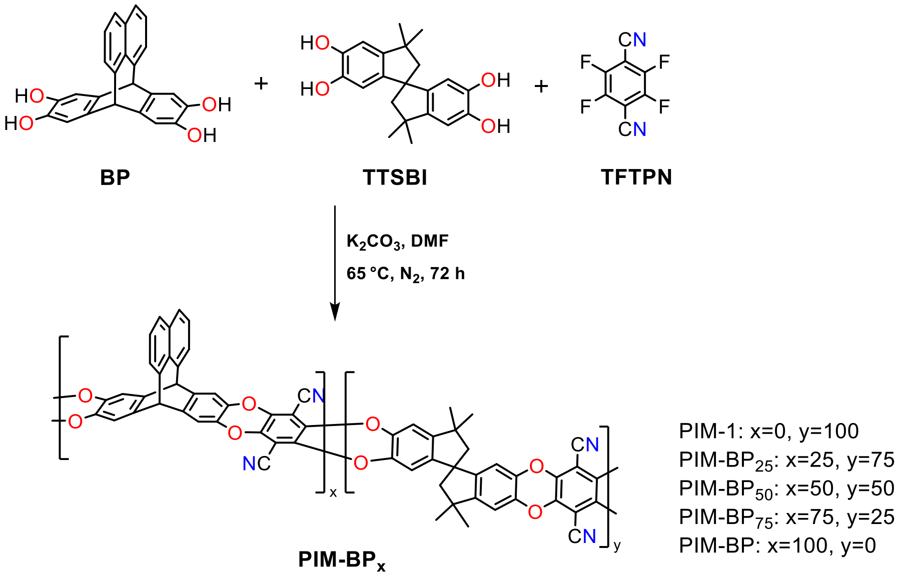

Scheme 3.5 Structure and synthesis of copolymers PIM-BP$_x$.

The TGA data for the PIM-BP homopolymer, PIM-BP$_x$ copolymers and PIM-1 are shown in **Figure 3.3**, and all the polymers demonstrate good thermal stability as expected. The homopolymer PIM-BP exhibits a high onset decomposition temperature at around 558 °C and a weight loss of 29.2% at 800 °C, while PIM-1 shows a higher weight loss of 39.6% at the same temperature. This difference is due to the BP predominantly being compose of aromatic components. The copolymers (PIM-BP$_{25}$, PIM-BP$_{50}$ and PIM-BP$_{75}$) exhibit a similar onset decomposition temperature at around 500 °C and lower weight loss at 800 °C compared to PIM-1. These findings indicate that PIM-BP possesses excellent structural stability, which is essential for its potential use in high-temperature environments.

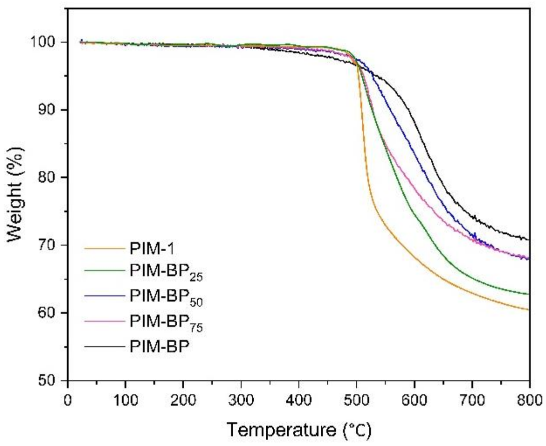

Figure 3.3 TGA analysis of PIM-BP homopolymer and PIM-BP$_x$ copolymers.

3.1.3 Physical properties and microporosity analysis of BP-based polymers

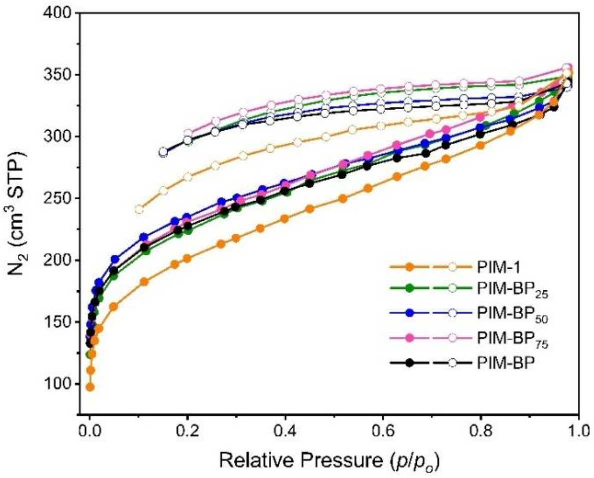

Figure 3.4 N_2 adsorption (filled circle) and desorption (open circle) isotherms of PIM-BP homopolymer and PIM-BP$_x$ copolymers at 77 K.

The N_2 adsorption-desorption isotherms of PIM-BP homopolymer and PIM-BP$_x$ copolymers are presented in **Fig 3.4**, and the corresponding physical properties are summarised in **Table 3.1** for comparison. In their powdered form, both PIM-BP homopolymer and PIM-BP$_x$ copolymers adsorb a large amount of N_2 at 77 K under low relative pressure ($P/P_0 < 0.1$), indicating significant microporosity. All BP-based polymers exhibit a significant increase in

BET surface area (SA_{BET}) in the range of 789-830 m^2 g^{-1} compared to PIM-1 (709 m^2 g^{-1}). The shapes of the N_2 isotherms are similar for BP-based polymers and PIM-1, with distinct hysteresis between the adsorption and desorption isotherms, which can be attributed to swelling of the polymer during N_2 adsorption.

Table 3.1 Physical properties of homopolymer PIM-BP and copolymers PIM-BP$_x$.

Polymer	Solubility	SA$_{\mathrm{BET}}$[a] (m^2 g^{-1})	V_{Total}[b] (ml g^{-1})	CO_2 uptake[c] (mmol g^{-1})
PIM-1	$CHCl_3$	709	0.55	2.19
PIM-BP$_{25}$	$CHCl_3$	789	0.54	2.68
PIM-BP$_{50}$	NMP	830	0.53	2.90
PIM-BP$_{75}$	NMP	813	0.55	2.72
PIM-BP	Quinoline	800	0.53	3.08

[a] BET surface area (SA_{BET}) was calculated from N_2 adsorption isotherm obtained at 77 K. [b] Total pore volume (V_{Total}) was estimated from N_2 adsorption at $P/P_o = 0.98$. [c] CO_2 uptake at 1 bar and 273 K.

For CO_2 uptake at 273 K, all BP-based polymers show similar isotherms with higher CO_2 adsorption capacity than PIM-1 (**Fig. 3.5a**) and exhibit a trend of enhanced CO_2 uptake with increasing BP content, indicating a greater concentration of ultramicropores (< 0.7 nm) after incorporation of BP units (**Fig. 3.5b**).

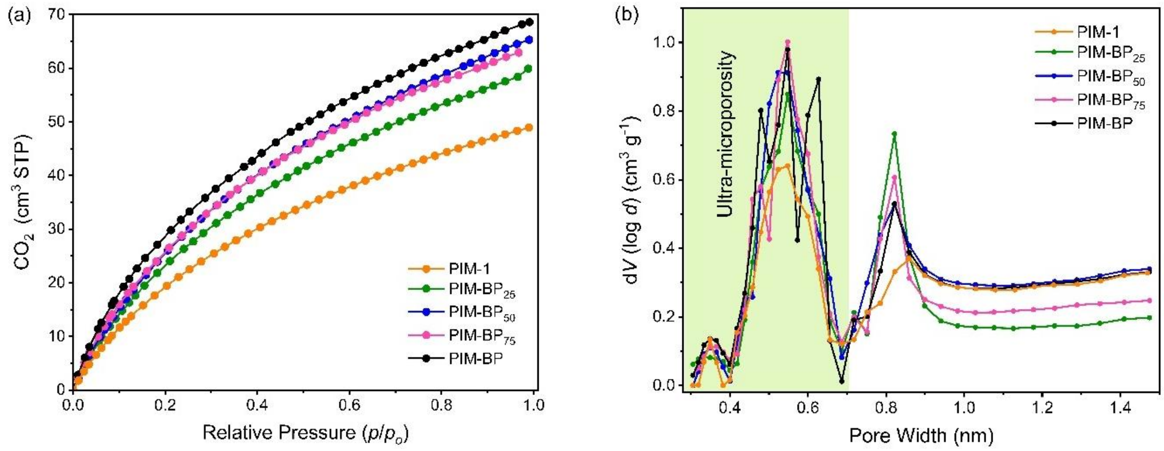

Figure 3.5 (a) CO_2 adsorption isotherms of BP-based polymers and PIM-1 and (b) their pore size distributions (PSD) calculated from CO_2 adsorption data using non-local density functional theory (NLDFT) model.

The flexible free-standing membrane of PIM-BP_{25} was cast from its chloroform solution, while those of PIM-BP_{50} and PIM-BP_{75} were obtained from their NMP solutions. The membrane of the homopolymer PIM-BP was cast from its quinoline solution (**Figure 3.6**).

PIM-BP_{25} **PIM-BP_{50}**

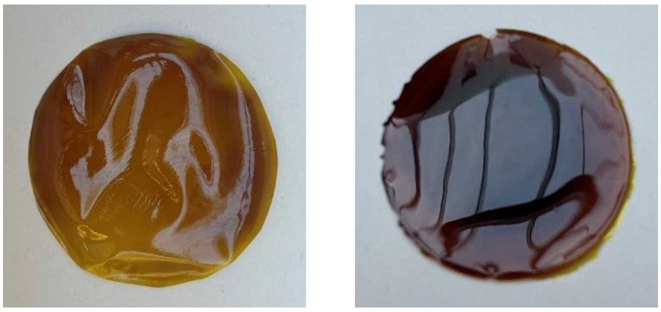

PIM-BP_{75} **PIM-BP**

Figure 3.6 Films of PIM-BP homopolymer and PIM-BP_x copolymers.

3.1.4 Gas transport properties of BP-based polymers

Single gas permeabilities were measured on freshly methanol-treated membranes, and the results are compared with those of reported PIM-Btrip, a representative material defining the 2019 upper bound for CO_2/N_2 and CO_2/N_2. These gas permeability data are summarised in **Table 3.2**. The gas permeability order for BP-based polymers is $CO_2 > H_2 > He > O_2 > CH_4 > N_2$, whereas in PIM-1, O_2 permeability is higher than that of He. This indicates that the incorporation of BP units enhances the size-sieving property, favouring the transport of small gas molecules. This can be attributed to the greater concentration of ultramicropores (< 0.7 nm) in all BP-based polymers (**Fig. 3.5b**). The reported PIM-Btrip demonstrates more pronounced size-sieving behavior than BP-based polymers, as its H_2 permeability is as high as that of CO_2.

Compared with the equivalent data for PIM-1, the incorporation of a small amount of BP units in PIM-BP_{25} leads to a significant reduction in gas permeability. However, gas permeability tends to increase with an increasing amount of BP unit and is highest for PIM-BP_{75}. And it is apparent that even a small amount of BP units in PIM-BP_{25} significantly enhances the ideal gas selectivity. Moreover, PIM-BP_{75} shows both higher gas permeability and markedly higher gas selectivity than PIM-1. The homopolymer PIM-BP shows gas permeabilities generally comparable to those of the reported polymer PIM-Btrip, with the exception of lower permeabilities for H_2 and He. This may be due to the lower intramolecular free volume (IMFV) of the BP units compared to that of the Btrip units.

Table 3.2 Membrane thickness (l, μm), gas permeabilities (P_A, Barrer;) and ideal selectivities (P_A/P_B) of freshly methanol treated and aged films measured at 25 °C and 1 bar.

Polymer	l [μm]	Permeability (Barrer)[a]						Selectivity					
		N_2	O_2	CO_2	CH_4	H_2	He	CO_2/CH_4	CO_2/N_2	O_2/N_2	H_2/N_2	H_2/CH_4	He/N_2
PIM-1	96	653	2072	12211	1153	4930	1938	10.6	18.7	3.2	7.6	4.3	3.0
(33 days)[b]	96	452	1656	8833	657	4558	1881	13.4	19.5	3.7	10.1	6.9	4.2
PIM-BP_{25}	72	188	765	4540	276	2530	1087	16.4	24.1	4.1	13.4	9.2	5.8
(30 days)	72	122	527	2887	155	1890	851	18.6	23.7	4.3	15.5	12.2	7.0
PIM-BP_{50}	73	256	1179	6689	330	4423	1898	20.3	26.1	4.6	17.3	13.4	7.4
(30 days)	73	162	759	4052	186	2721	1113	21.7	25.0	4.7	16.8	14.6	6.9
PIM-BP_{75}	79	476	2125	12328	634	6793	2628	19.4	25.9	4.5	14.3	10.7	5.5
(30 days)	79	298	1457	7759	353	5315	2137	22.0	26.0	4.9	17.8	15.6	7.2
PIM-BP	90	334	1603	8847	441	5665	2111	20.1	26.5	4.8	17.0	12.9	6.3
(131 days)	90	127	673	3301	135	2819	1171	24.5	26.0	5.3	22.2	21.0	9.2
(321 days)	90	112	584	3131	120	2358	967	26.2	28.0	5.2	21.1	19.7	8.6
PIM-Btrip[97]	64	339	1800	9200	412	9430	3960	22.3	27.1	5.31	27.8	22.9	11.7
(120 days)	64	200	1160	6040	237	7180	3020	25.5	30.2	5.8	35.8	30.3	12.7
(371 days)	64	154	997	5150	163	7730	3620	31.6	33.4	6.5	50.2	47.4	23.5

[a] 1 Barrer = 10^{-10} cm^3_{STP} cm cm^{-2} s^{-1} cm Hg^{-1}. [b] Number in parenthesis is the ageing days after methanol treatment.

Gas transport through a polymer is described by the solution diffusion model[126-127] with $P_A = D_A \times S_A$, where D_A is the diffusivity coefficient, and S_A is the solubility coefficient for gas A. Therefore, the ideal selectivity (P_A/P_B) for a polymer can be expressed as the product of the diffusivity selectivity (D_A/D_B) and solubility selectivity (S_A/S_B). The effect of the BP unit on the gas transport properties was investigated by the analysis of diffusivity coefficients, diffusivity selectivity (**Table 3.3**), solubility coefficients and solubility selectivity (**Table 3.4**). A comparison with the reported PIM-Btrip is also presented. Due to the high diffusion rates of H_2 and He, which make accurate measurement difficult, the analysis of diffusivity and solubility will focus on the larger gases (N_2, O_2, CO_2, and CH_4).

Table 3.3 Gas diffusion coefficients D (10^{-12} m^2s^{-1}) and diffusivity selectivities (D_A/D_B) of freshly methanol treated and aged films measured at 25 °C and 1 bar.

Polymer	l [μm]	*Diffusivity coefficient*				*Diffusivity selectivity*		
		N_2	O_2	CO_2	CH_4	CO_2/CH_4	CO_2/N_2	O_2/N_2
PIM-1	96	144.2	397.3	172.3	63.9	2.70	1.20	2.76
(33 days)[b]	96	84.9	290.1	121.0	31.2	3.88	1.43	3.42
PIM-BP_{25}	72	40.1	158.1	58.0	13.1	4.43	1.45	3.94
(30 days)	72	27.9	112.7	43.0	8.5	5.06	1.54	4.04
PIM-BP_{50}	73	46.9	200.6	73.8	15.2	4.86	1.57	4.28
(30 days)	73	33.1	148.1	52.0	9.2	5.65	1.57	4.47
PIM-BP_{75}	79	118.8	483.3	175.4	34.0	5.16	1.48	4.07
(30 days)	79	67.9	319.2	121.5	20.2	6.01	1.79	4.70
PIM-BP	90	37.1	189.1	51.4	8.0	6.43	1.39	5.10
(131 days)	90	15.6	83.2	25.5	4.0	6.38	1.63	5.33
(321 days)	90	15.1	79.4	25.5	4.22	6.04	1.69	5.25
PIM-Btrip[97]	64	48.6	274	88.3	11.9	7.42	1.82	5.64
(120 days)	64	30.2	183	61.6	9.3	6.62	2.04	6.06
(371 days)	64	18.9	122	34.7	4.7	7.38	1.84	6.46

The gas diffusivity coefficients of PIM-BP_{25} and PIM-BP_{50} are lower than those of PIM-1 but show a gradual increase with higher BP content. The solubility coefficients of all gases for all copolymers show only small variations as the BP content changes. Therefore, the low gas permeability observed in PIM-BP$_{25}$ and PIM-BP$_{50}$ is due to their reduced diffusivity coefficients. Similarly, the higher CO_2 and O_2 permeabilities of PIM-BP$_{75}$ compared to those of PIM-1 can be attributed to its higher diffusivity coefficients (**Table 3.3**). In contrast, the high CO_2 and O_2 permeabilities for the homopolymer PIM-BP are primarily due to its significantly high solubility coefficients (**Table 3.4**). The CO_2/CH_4 and O_2/N_2 diffusivity selectivities for PIM-BP$_x$ copolymers are improved by increasing BP content and are highest for the PIM-BP homopolymer. This trend is illustrated by the correlation between the diffusivity coefficients (D_A) and the square of the effective gas diameter (d^2_{eff}) (**Fig. 3.7**). It has been well established that the steepness of the slope for the correlation between d^2_{eff} and D_A of O_2, CO_2, N_2 and CH_4 is a good indicator of the diffusivity selectivity for a polymer.[128]

Table 3.4 Gas solubility coefficients S ($\mathrm{cm^3_{STP}\ cm^{-3}\ bar^{-1}}$) and solubility selectivities (S_A/S_B) of freshly methanol treated and aged films measured at 25 °C and 1 bar of feed pressure.

Polymer	l [μm]	*Solubility coefficient*					*Solubility selectivity*		
		N_2	O_2	CO_2	CH_4		CO_2/CH_4	CO_2/N_2	O_2/N_2
PIM-1	96	3.4	3.9	53.2	13.5		3.94	15.65	1.15
(33 days)[b]	96	4.0	4.3	54.8	15.8		3.47	13.7	1.08
PIM-BP$_{25}$	72	3.5	3.6	58.7	15.8		3.72	16.77	1.03
(30 days)	72	3.3	3.5	50.4	13.6		3.71	15.27	1.06
PIM-BP$_{50}$	73	4.1	4.4	68.0	16.3		4.17	16.59	1.07
(30 days)	73	3.7	3.8	58.5	15.2		3.85	15.81	1.03
PIM-BP$_{75}$	79	3.0	3.3	52.7	14.0		3.76	17.57	1.1
(30 days)	79	3.3	3.4	47.9	13.1		3.66	14.52	1.03
PIM-BP	90	6.8	6.4	129.2	41.6		3.11	19.0	0.94
(131 days)	90	6.1	6.1	97.2	25.2		3.86	15.93	1.0
(321 days)	90	5.5	5.5	92.2	21.3		4.33	16.76	1.0
PIM-Btrip[97]	64	5.2	4.9	78.2	26.1	-	3.0	15.04	0.94
(120 days)	64	5.0	4.8	73.6	19.1	-	3.85	14.72	0.96
(371 days)	64	6.1	6.1	111	25.8	-	4.30	18.20	1.0

The slope of D_A versus d^2_{eff} is steeper for the PIM-BP$_x$ copolymers than for PIM-1, with the PIM-BP homopolymer exhibiting the steepest slope. This enhanced molecular sieving property is attributed to the greater rigidity of the BP unit compared to the SBI unit. In contrast, their CO_2/CH_4 solubility selectivity remains constant, while the O_2/N_2 solubility selectivity stays close to unity. As expected, the notable improvements in CO_2/CH_4 and O_2/N_2 selectivities for PIM-BP$_x$ copolymers and PIM-BP homopolymer result from their enhanced diffusivity selectivities (**Table 3.3**). As a result, their gas permeability data all lie above the 2008 upper bounds for O_2/N_2 and CO_2/CH_4 due to the size-sieving behaviour of the polymers. In particular, the data points for both the PIM-BP$_{75}$ copolymer and PIM-BP homopolymer lie on the 2019 CO_2/CH_4 and 2015 O_2/N_2 upper bounds (**Fig. 3.8**).

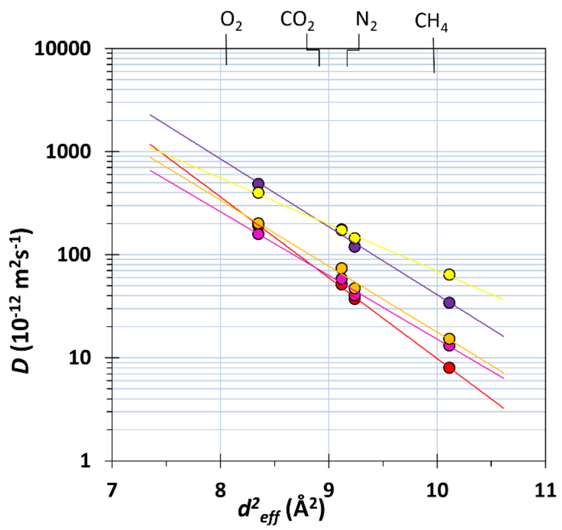

Figure 3.7 Correlation of diffusivity coefficients (D_A) with the square of the effective gas diameter (d^2_{eff}) (O_2 = 2.89, CO_2 = 3.02, N_2 = 3.04, CH_4 = 3.18 Å) for freshly methanol treated films of PIM-BP$_{25}$ (●), PIM-BP$_{50}$ (●), PIM-BP$_{75}$ (●), PIM-BP (●)and PIM-1(●).

CO_2 separations are more complex than those primarily governed by diffusivity selectivity (e.g., O_2/N_2), as CO_2 solubility (S_{CO_2}) plays a dominant role in transport, particularly in CO_2/N_2 separations, due to the similar effective diameters of the two gas molecules. In general, the improved CO_2/N_2 selectivities observed for all BP-based polymers primarily result from their higher solubility selectivity compared to PIM-1 (**Table 3.4**). As expected, PIM-BP$_{75}$ exhibits a promising CO_2/N_2 separation performance, with a CO_2 permeability of 12328 Barrer and CO_2/N_2 selectivity of 25.9, placing it slightly above the newly defined 2019 CO_2/N_2 upper bound (**Fig. 3.8**). The homopolymer PIM-BP exhibits a CO_2/N_2 separation performance comparable to that of the reported PIM-Btrip. Notably, while the high CO_2/N_2 selectivity of PIM-BP originates from its high solubility selectivity, that of PIM-Btrip is primarily attributed to its diffusivity selectivity.

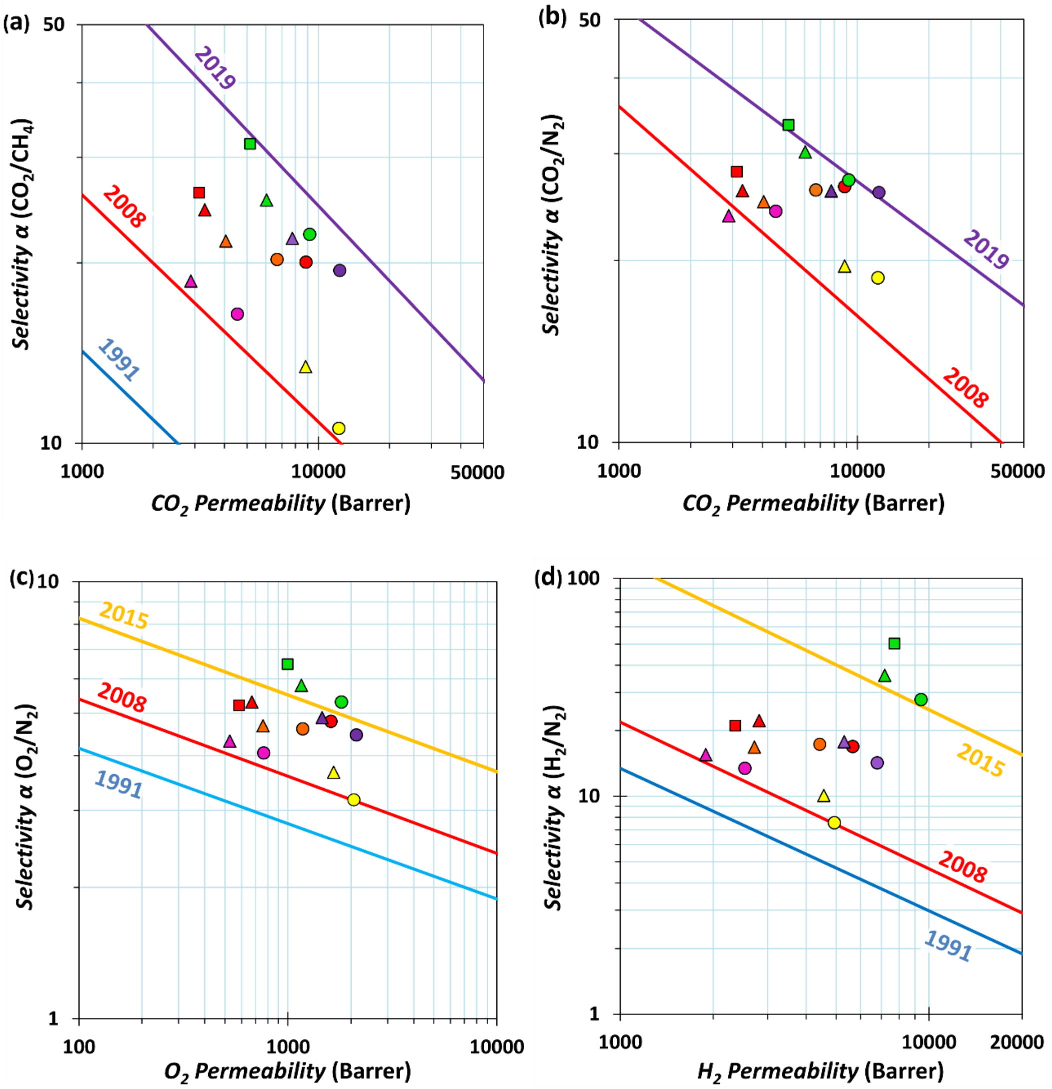

Figure 3.8 Robeson plots for the (a) CO_2/CH_4, (b) CO_2/N_2, (c) O_2/N_2 and (d) H_2/N_2 gas pairs showing the position of the gas permeability data for films of PIM-BP$_{25}$ (●, ▲) PIM-BP$_{50}$ (●, ▲), PIM-BP$_{75}$ (●, ▲), PIM-BP (●, ▲, ■), PIM-Btrip[97] (●, ▲, ■)and PIM-1(●, ▲). Freshly methanol treated samples are indicated as circles (○) and further aging are indicated as (△, □). The upper bounds are represented by blue lines (1991), red lines (2008), yellow lines for O_2/N_2 and H_2/N_2 (2015), purple lines for CO_2/CH_4 and CO_2/N_2 (2019).

Physical ageing is a typical phenomenon for glassy polymers, where polymer chains pack more tightly over time, leading to the reduction in gas permeability accompanied by an increase in gas selectivity for all gas pairs. This is especially relevant for high free volume polymers such as PIMs, which lose a large amount of permeability over time. Ageing studies were performed on the films to investigate the impact of the BP unit on gas permeability (**Table 3.2**). Overall, both PIM-BP$_x$ copolymers and the PIM-BP homopolymer experience a reduction in gas permeabilities along with an increase in CO_2/CH_4 and O_2/N_2 selectivity during ageing. This is because ageing decreases the diffusivity coefficient for all polymers but enhances the diffusivity selectivity (**Table 3.3**). However, a slightly reduction in CO_2/N_2 selectivity was observed for all BP-based polymers after short-term aging, while PIM-Btrip and PIM-1 showed an increase in CO_2/N_2 selectivity.

3.2 Amidoxime modified PIM-BP

The work of polymers based on BP proves that BP is a promising building block for gas separation membranes. However, the homopolymer PIM-BP could only be cast into films using high boiling point solvent such as quinoline. Post-polymerisation modifications at the nitrile groups have resulted in polymers with good solution processability and improved gas separation performance.[99, 129-130]

In 2012, Patel *et al.* reported a non-invasive post-modification of PIMs via amidoxime functionalisation. The amidoxime-functionalised PIM-1 (AO-PIM-1) can be synthesised by a rapid reaction of the nitrile groups with hydroxylamine under reflux conditions. AO-PIM-1 demonstrates improved CO_2 uptake capacity due to the strong affinity of the amidoxime functionality for CO_2. After functionalisation, AO-PIM-1 still have good processability and is soluble in polar aprotic solvents such as dimethylformamide (DMF) and dimethyl sulfoxide (DMSO).[131] In addition, AO-PIM-1 demonstrates enhanced ideal selectivities for CO_2/CH_4 and CO_2/N_2 in pure-gas permeation measurements, as well as stable mixed-gas CO_2/CH_4 selectivities across a 20 bar pressure range in mixed-gas permeation measurements.[129]

More recently, Chen *et al.* from McKeown's group reported amidoxime-functionalised PIMs based on dibenzomethanopentacene (DBMP) unit. The unmodified PIM-DBMP proved only partially soluble in quinoline and gave very brittle films from its quinoline solution. After functionalisation, the PIM-DBMP-AO showed improved solution processability and was well-soluble in NMP, from which robust, self-standing films could be cast.[132] In addition, PIM-DBMP-AO exhibits improved gas selectivities for CO_2/N_2, CO_2/CH_4, O_2/N_2, H_2/N_2 and H_2/CH_4 due to its enhanced size-sieving property. This is attributed to the hydrogen bonding between the amidoxime groups, which tightens the microstructure in polymer. Due to the exceptional gas selectivity combined with high permeability, the data for PIM-DBMP-AO were located above the 2015 upper bounds for O_2/N_2, H_2/N_2 and H_2/CH_4.

3.2.1 Synthesis of amidoxime modified PIM-BP (AO-PIM-BP)

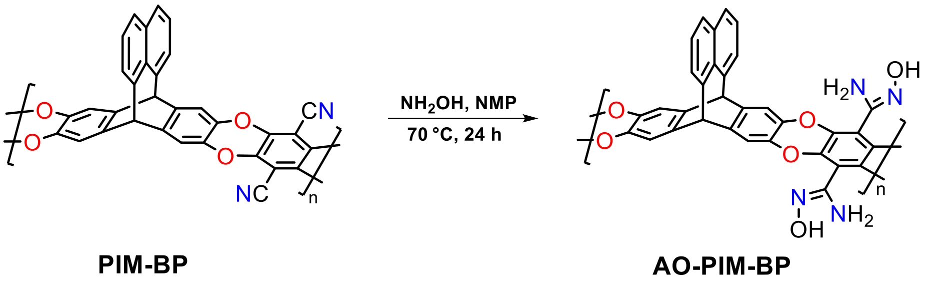

Scheme 3.6 Structure and synthesis of amidoxime-functionalised PIM-BP (AO-PIM-BP).

The amidoxime modified PIM-BP (AO-PIM-BP) was synthesised according to the literature procedure reported by Patel *et al.*[131] PIM-BP was reacted with hydroxylamine in NMP at 70 °C for 1 day (**Scheme 3.6**). The resulting polymer AO-PIM-BP was obtained as a light brown powder. Successful conversion of nitrile to amidoxime groups was confirmed by FTIR spectroscopy. The characteristic nitrile stretching band at 2239 cm^{-1} completely disappears in AO-PIM-BP, accompanied by the appearance of two new broad bands at 3350 and 3478 cm^{-1}, corresponding to the stretching vibrations of OH and NH_2 respectively (**Figure 3.9a**). The bands at 1643 and 912 cm^{-1} are assigned to the C=N and N-O stretching vibrations of amidoxime groups.

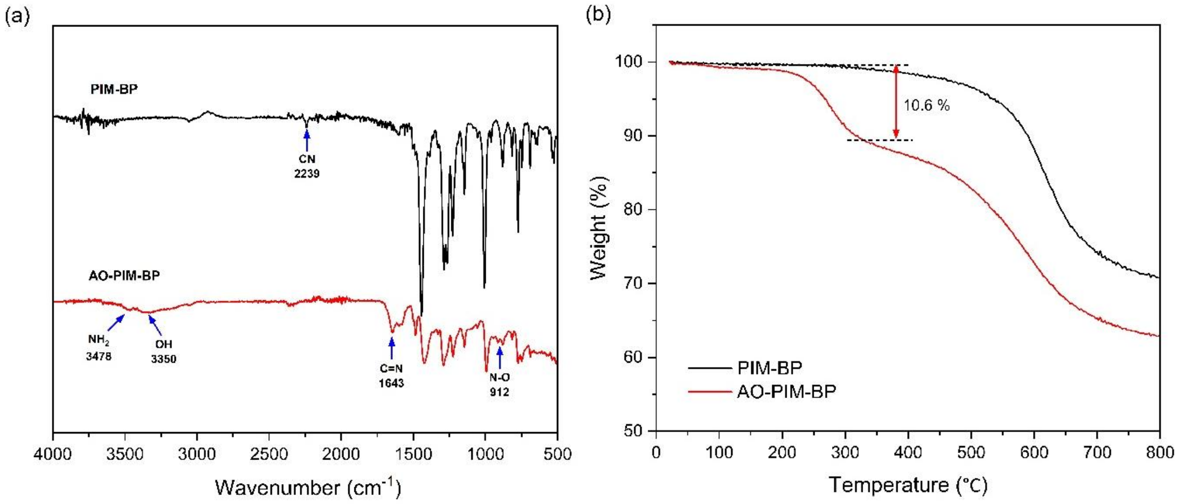

Figure 3.9 (a) FTIR spectra and (b) TGA spectra of PIM-BP and AO-PIM-BP

TGA analysis of AO-PIM-BP shows two-step decomposition (**Figure 3.9b**), which is similar to AO-PIM-1[131]. The weight loss of 10.6 % in the range of 200-322 °C is attributed to thermal decomposition of the amidoxime group, followed by a second decomposition temperature at over 500 °C.

3.2.2 Physical properties and microporosity analysis of AO-PIM-BP

Table 3.5 Physical properties of AO-PIM-BP.

Polymer	Solubility	SA_{BET}[a] (m^2 g^{-1})	V_{Total}[b] (ml g^{-1})	CO_2 uptake[c] (mmol g^{-1})
PIM-BP	Quinoline	800	0.53	3.08
AO-PIM-BP	NMP	-	-	-
PIM-1	$CHCl_3$	709	0.55	2.19
AO-PIM-1[129]	DMSO, NMP	577	0.28	2.74

[a] BET surface area (SA_{BET}) was calculated from N_2 adsorption isotherm obtained at 77 K. [b] Total pore volume (V_{Total}) was estimated from N_2 adsorption at $P/P_o = 0.98$. [c] CO_2 uptake at 1 bar and 273 K.

The incorporation of AO groups into PIM-BP leads to an improvement in solubility. AO-PIM-BP exhibits good solubility in NMP, whereas the unmodified PIM-BP is only soluble in quinoline. Therefore, free-standing films of AO-PIM-BP were successfully prepared by casting from its NMP solutions. The N_2 and CO_2 adsorption isotherms, as well as the corresponding BET data, are not presented here due to ongoing maintenance problems with the gas adsorption instrument in our laboratory.

3.2.3 Gas transport property

Single gas permeabilities were measured using freshly methanol treated films of AO-PIM-BP. A comparison of gas permeability data for AO-PIM-BP, PIM-BP, and the reported AO-PIM-1 is summarised in **Table 3.6**. The gas permeability order for AO-PIM-BP is $H_2 > CO_2 > He > O_2 > N_2 > CH_4$. In the case of unmodified PIM-BP, the most permeable gas is CO_2, following the order of $CO_2 > H_2 > He > O_2 > CH_4 > N_2$. As described in **Section 3.1.4**, PIM-BP exhibits exceptional size-sieving properties, while AO-PIM-BP demonstrates even more pronounced size-sieving behaviour with significantly higher gas selectivities, favouring the transport of smaller gases. However, the gas permeability of AO-PIM-BP is much lower than that of PIM-BP, as expected from the trade-off relationship. AO-PIM-BP shows both higher gas permeability and selectivity compared to the reported AO-PIM-1. The improved size-sieving properties of AO-PIM-BP can be attributed to synergistic effect of highly rigid polymer backbones and hydrogen bonding network.

Table 3.6 Membrane thickness (l, μm), gas permeabilities (P_A, Barrer) and ideal selectivities (P_A/P_B) of AO-PIM-BP, PIM-BP and reported AO-PIM-1.

Polymer	l [μm]	Permeability (Barrer)[a]						Selectivity					
		N_2	O_2	CO_2	CH_4	H_2	He	CO_2/CH_4	CO_2/N_2	O_2/N_2	H_2/N_2	H_2/CH_4	He/N_2
AO-PIM-BP[b]	127	31.5	250	1189	19.6	2380	979	60.7	37.7	7.9	75.6	121.4	31.1
PIM-BP[b]	90	334	1603	8847	441	5665	2111	20.1	26.5	4.8	17.0	12.9	6.3
AO-PIM-1[c]	_	33	147	1153	34	912	412	34	35	4.5	27.6	26.8	12.5

[a] 1 Barrer = 10^{-10} cm^3_{STP} cm cm^{-2} s^{-1} cm Hg^{-1}. [b] T=25 °C, 1 bar. [c] T=35 °C, 2 bar.[129]

The diffusivity coefficients, solubility coefficients, diffusivity selectivities and solubility selectivities for AO-PIM-BP are listed in **Table 3.7** and **Table 3.8** to show the effect of amidoxime functionality on the gas transport properties. The gas diffusivity coefficients of larger gases (N_2, O_2, CO_2, and CH_4) in AO-PIM-BP are significantly reduced compared to those in PIM-BP while their solubility coefficients remain comparable. Therefore, the reduced diffusivity coefficients are the primary cause of the permeability reduction for larger gases (N_2, O_2, CO_2, and CH_4) in AO-PIM-BP (**Table 3.7)**. The gas diffusivity coefficient of H_2 exhibits minimal variation in AO-PIM-BP compared to PIM-BP, whereas that of He is significantly enhanced, indicating enhanced size-sieving properties. Consequently, the reduced permeabilities of smaller gases (He and H_2) primarily result from their decreased solubility coefficients (**Table 3.8)**.

Table 3.7 Gas diffusion coefficients *D* (10^{-12} m^2s^{-1}) and diffusivity selectivities (D_A/D_B) of of AO-PIM-BP, PIM-BP and reported AO-PIM-1.

Polymer	*l* [μm]	*Diffusivity coefficient*						*Diffusivity selectivity*					
		N_2	O_2	CO_2	CH_4	H_2	He	CO_2/CH_4	CO_2/N_2	O_2/N_2	H_2/N_2	H_2/CH_4	He/N_2
AO-PIM-BP[a]	127	2.9	24.3	5.6	0.4	3670	27320	14.0	1.93	8.38	1266	9175	9421
PIM-BP[a]	90	37.1	189	51.4	8.0	3784	4055	6.43	1.39	5.10	102	473	109
AO-PIM-1[b]	_	9.9	40.6	24.6	2.6	_	_	9.5	2.5	4.1	_	_	_

[a] T=25 °C, 1 bar. [b] T=35 °C, 2 bar.[129]

Table 3.8 Gas solubility coefficients *S* (cm^3_{STP} cm^{-3} bar^{-1}) and solubility selectivities (S_A/S_B) of AO-PIM-BP, PIM-BP and reported AO-PIM-1.

Polymer	*l* [μm]	*Solubility coefficient*						*Solubility selectivity*					
		N_2	O_2	CO_2	CH_4	H_2	He	CO_2/CH_4	CO_2/N_2	O_2/N_2	H_2/N_2	H_2/CH_4	He/N_2
AO-PIM-BP[a]	127	8.1	7.7	160	33.2	0.49	0.03	4.82	19.8	0.95	0.06	0.01	0.004
PIM-BP[a]	90	6.8	6.4	129	41.6	1.12	0.39	3.11	19.0	0.94	0.16	0.03	0.06
AO-PIM-1[b]	_	3.3	3.6	46.8	13.0	_	_	3.6	14.2	1.1			

[a] T=25 °C, 1 bar. [b] T=35 °C, 2 bar.[129]

The diffusivity selectivity of small gases over large gases is greatly improved, as illustrated by the correlation between the diffusivity coefficients (D_A) and the square of the effective gas diameter (d^2_{eff}) (**Fig. 3.10**). A clearly steeper slope of D_A versus d^2_{eff} is observed for AO-PIM-BP compared to PIM-BP, due to its enhanced size-sieving property. To be specific, AO-PIM-BP demonstrates significantly enhanced diffusivity selectivities compared to PIM-BP, by about 64% for O_2/N_2, 12-fold for H_2/N_2, 19-fold for H_2/CH_4, and 86-fold for He/N_2 (**Table 3.7**). As a result, AO-PIM-BP exhibits outstanding gas selectivities in separations dominated by diffusivity selectivity, with values of 7.9 (O_2/N_2), 75.6 (H_2/N_2), 121.4 (H_2/CH_4) and 31.1 (He/N_2) respectively (**Table 3.6**). In particular, AO-PIM-BP shows excellent H_2 separation performance, with a H_2 permeability of 2380 Barrer, H_2/N_2 selectivity of 75.6, and H_2/CH_4 selectivity of 121.4, which are among the best PIMs reported to date. The exceptional gas selectivity combined with high permeability positions AO-PIM-BP above the 2015 upper bounds for O_2/N_2, H_2/N_2 and H_2/CH_4 (**Fig. 3.11c, d and e**). In addition, the high He permeability (979 Barrer) along with improved He/N_2 selectivity (31.1) places AO-PIM-BP above the 2018 upper bound for He/N_2, whereas PIM-BP is located near the 1991 upper bound (**Fig. 3.11f**).

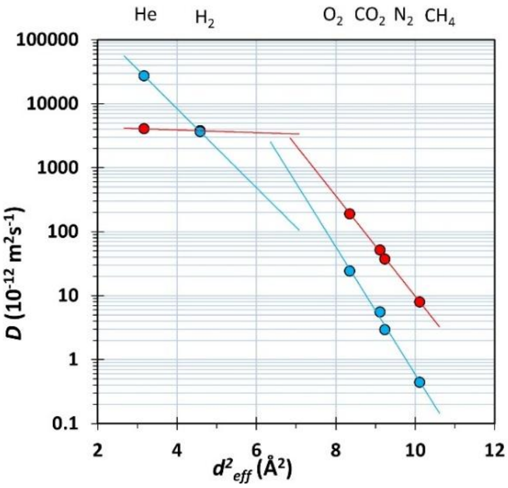

Figure 3.10 Correlation of diffusivity coefficients (D_A) with the square of the effective gas diameter (d^2_{eff}) (He = 1.78, H_2 = 2.14, O_2 = 2.89, CO_2 = 3.02, N_2 = 3.04, CH_4 = 3.18 Å) for freshly methanol treated films of AO-PIM-BP (●) and PIM-BP (●).

AO-PIM-BP shows a 24% increase in CO_2 solubility coefficients along with a 20% decrease in CH_4 solubility coefficients, resulting in a 55% enhancement in CO_2/CH_4 solubility selectivity compared to PIM-BP. This improvement is attributed to the strong affinity of the amidoxime group toward CO_2.[131] However, the reported AO-PIM-1 shows a reduction in both the CO_2 solubility coefficient and the CO_2/CH_4 solubility selectivity relative to PIM-1. Such interactions between the amidoxime group and CO_2 were not reflected from the solubility coefficients in the AO-PIM-1.[129] In addition, the diffusion-based size sieving effect in AO-PIM-BP leads to two-fold increase in CO_2/CH_4 diffusivity selectivity compared to PIM-BP. As a result, AO-PIM-BP exhibits a high CO_2/CH_4 gas selectivity, which is three-fold higher than that of PIM-BP due to the enhanced solubility selectivity and diffusivity selectivity. Therefore, the gas permeability data ($P_{CO_2} = 1189\ \text{Barrer}, \alpha_{CO_2/CH_4} = 60.7$) of AO-PIM-BP lies on the latest 2019 upper bound for CO_2/CH_4 (**Fig. 3.11a)**.

For CO_2/N_2, AO-PIM-BP possesses higher gas selectivity than PIM-BP but lower CO_2 permeability. Its gas permeability data lies on the 2008 upper bound for CO_2/N_2, whereas PIM-BP lies on the latest upper bound. The CO_2/N_2 separation performance ($P_{CO_2} = 1189\ \text{Barrer}, \alpha_{CO_2/N_2} = 37.7$) of AO-PIM-BP is similar to that of reported AO-PIM-1, with the data located at a similar position on the 2008 upper bound.

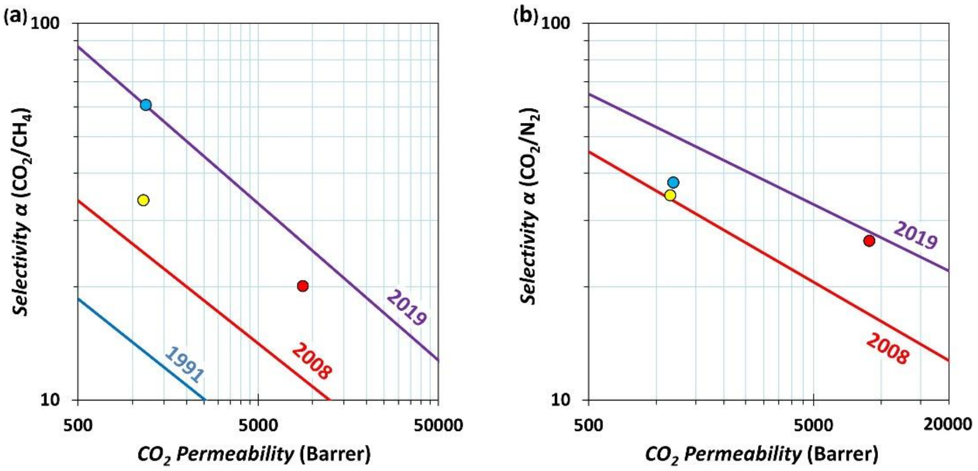

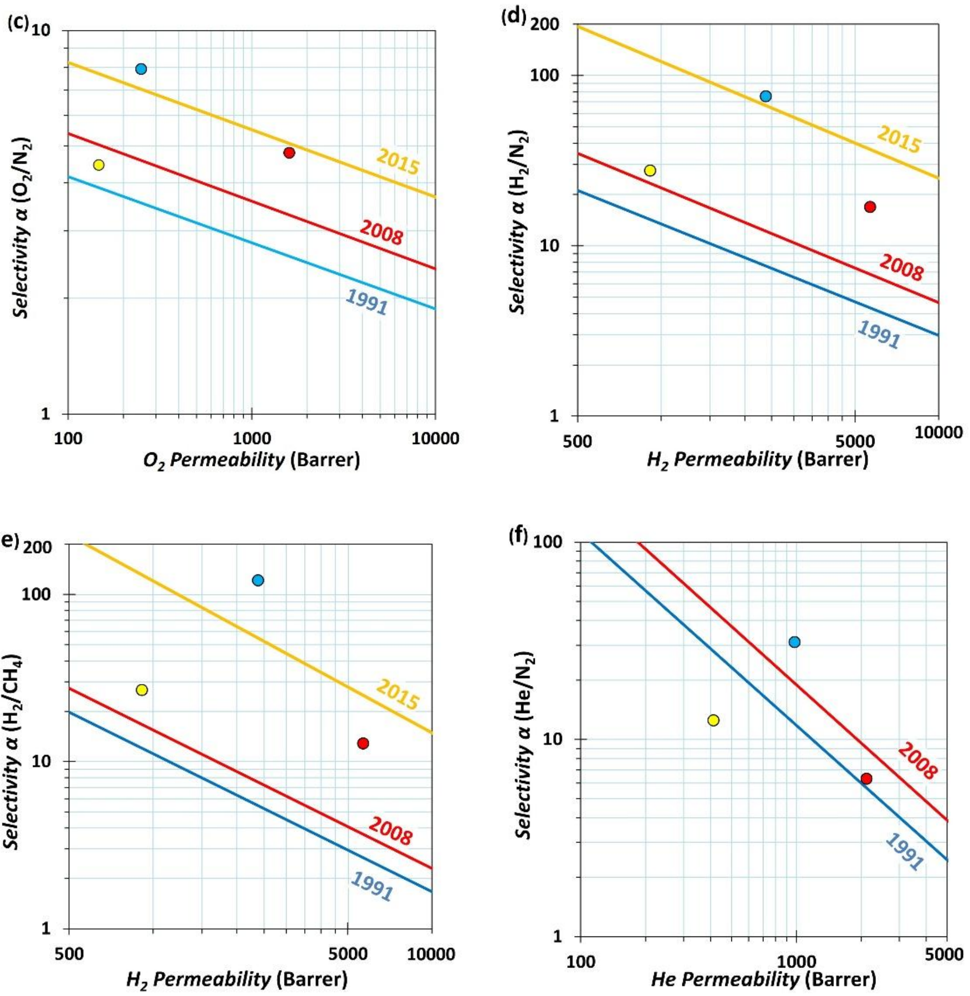

Figure 3.11 Robeson plots for the (a) CO_2/CH_4, (b) CO_2/N_2, (c) O_2/N_2, (d) H_2/N_2, (e) H_2/CH_4 and (f) He/N_2 gas pairs showing the position of the gas permeability data for freshly methanol treated films of AO-PIM-BP (●) PIM-BP (●) and AO-PIM-1[127] (●). The upper bounds are represented by blue lines (1991), red lines (2008), yellow lines for O_2/N_2, H_2/CH_4 and H_2/N_2 (2015), purple lines for CO_2/CH_4 and CO_2/N_2 (2019).

Overall, BP is an excellent building block for making PIMs with high gas separation performance. The unique structure of BP provides polymers with high chain rigidity and ultramicropores and thus leads to enhanced gas separation performance. In particular, PIM-BP homopolymer and PIM-BP$_{75}$ copolymer exhibit outstanding separation performance for gas pairs CO_2/CH_4, CO_2/N_2 and O_2/N_2, comparable to those of the upper bound-defining PIM-Btrip. In addition, PIM-BP$_{75}$ shows better solubility than both PIM-BP and the reported PIM-Btrip. Moreover, the simple three-step synthesis of BP is much easier than the multi-step, complicated synthesis of benzotriptycene (Btrip) monomer. These make BP-based polymers a great potential material for energy-efficient applications, such as natural gas or biogas upgrading (CO_2/CH_4), post-combustion carbon capture (CO_2/N_2) and oxygen or nitrogen enrichment of air (O_2/N_2). In addition, both chain rigidity and intermolecular hydrogen bonding provide AO-PIM-BP with extraordinary gas selectivity. The exceptional gas selectivity combined with high permeability positions AO-PIM-BP above the 2015 upper bounds for O_2/N_2, H_2/N_2 and H_2/CH_4. These make AO-PIM-BP a promising candidate for hydrogen economy applications such as hydrogen recovery from gas mixtures like H_2/N_2 and H_2/CH_4.

Chapter 4: Aryl Ether-Bridged Dinaphthalene (EDN)-derived Polymers

Microporous organic polymers (MOPs) with well-defined pore structures are widely investigated for membrane technologies. As described in previous chapters, polymers of intrinsic microporosity (PIMs), which combine gas sieving capability with solution processability, exhibit unique and exceptional gas separation properties and help define the state-of-the-art in membrane materials. However, dibenzodioxin-based ladder polymers, such as PIM-1 and PIM-Btrip, require highly functionalised monomers (biscatechols and aryl tetrafluorides), which limit the accessible structural diversity of PIMs. Another class of ether-bridged polymers, poly(arylene ether)s (PAEs), has been developed for various membrane-based applications including gas separation[133], proton exchange[134] and ion conduction.[135] Compared to the well-known ladder-type microporous PIMs, the non-ladder architecture of PAEs provides a tunable synthetic route that utilizes readily available aryl dihalides and bisphenol monomers.[136-137] However, the lack of intrinsic microporosity and limited free volume results in low gas permeability for PAEs such as poly(ether ether ketone) (PEEK).[133] Previous studies have demonstrated that intrinsically microporous PEEK with enhanced free volume can be achieved via the incorporation of bridged bicyclic or contorted monomers, such as triptycene units, into the polymer backbone.[134] Therefore, it is of interest to explore the properties of poly(ether ether ketone) (PEEK) and poly(ether ether sulfone) (PES) incorporating novel bridged bicyclic units.

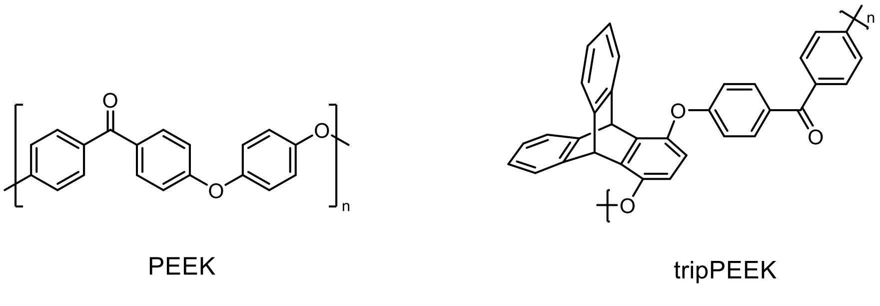

Figure 4.1 Structure of PEEK and tripPEEK[134] containing triptycene units.

4.1 Synthesis of aryl ether-bridged dinaphthalene (EDN) Monomer

The aryl ether-bridged dinaphthalene monomer (7,14-epoxy-7*H*,14*H*-cycloocta[1,2,3-*de*:5,6,7-*d*'*e*']dinaphthalene - EDN) **(16)** was unexpectedly prepared using the synthetic route shown in **Scheme 4.1**. An acid-mediated reaction between 1,8-naphthalene dialdehyde hydrate **(14)** and 2,7-dihydroxynaphthalene was conducted using acetic acid and conc. HCl under reflux for 6 h. The reaction mixture was poured into ice water, and the resulting precipitate was collected by filtration and washed with water, affording EDN **(16)** in high yield (93%) with high purity. The precursor 1,8-naphthalene dialdehyde hydrate **(14)** was synthesised as described in **Section 3.1.1**. The structure of EDN **(16)** is composed of two naphthalene units joined at their 1,8 (peri) by two carbon atoms between which is a bridging oxygen atom**.**

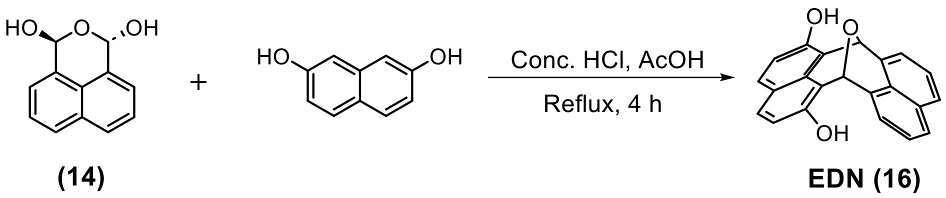

Scheme 4.1 Synthesis of 7,14-epoxy-7*H*,14*H*-cycloocta[1,2,3-*de*:5,6,7-*d*'*e*']dinaphthalene (EDN) **(16)**.

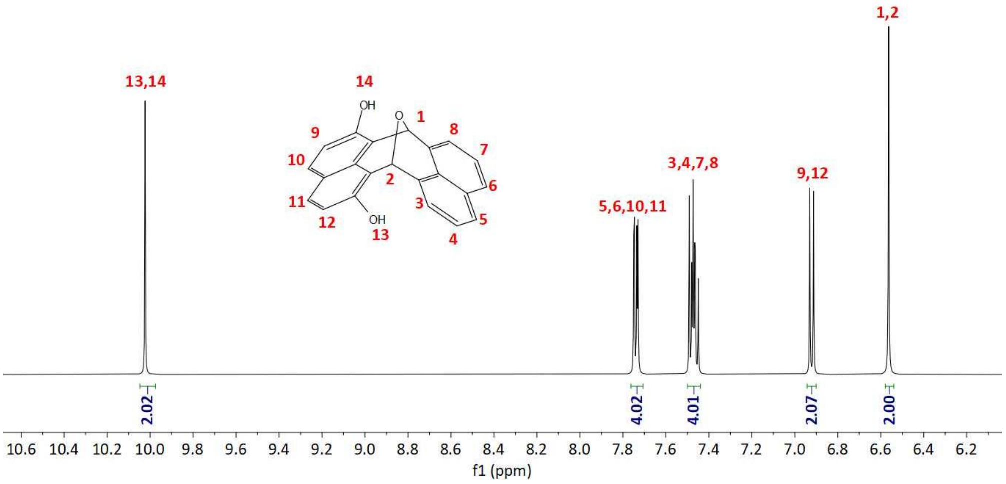

Figure 4.2 ^{1}H NMR of EDN **(16)** monomer.

The obtained product was analysed by ^{1}H NMR spectroscopy, where the presence of characteristic bridgehead protons at 6.56 ppm and a singlet at 10.02 ppm represents aromatic hydroxyl groups (Ar-OH) strongly indicates the efficient formation of the EDN **(16)** structure (**Figure 4.2**). The X-ray crystal structure (**Figure 4.3**) provides further confirmation of the bridged bicyclic structure of EDN **(16)**.

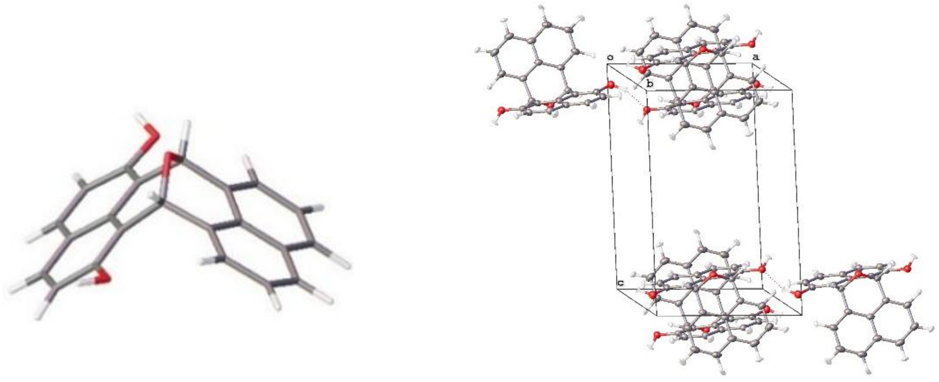

Figure 4.3 X-ray crystal structure and molecular packing of (EDN) **(16)**. The crystal packing image shows the hydrogen bonding interactions between hydroxyls (red) in the solid state.

4.2 Synthesis of EDN-derived polymers

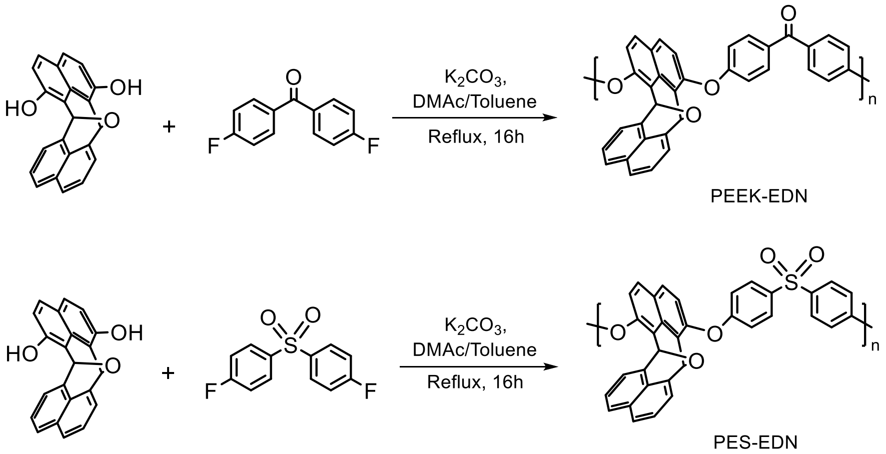

Scheme 4.2 Synthesis of PEEK-EDN and PES-EDN through SNAr reaction.

With the successfully synthesised bisphenol monomer in hand, polymerisation was conducted via an aromatic nucleophilic substitution (SNAr) reaction between the EDN monomer and cheaply available 4,4′-difluorobenzophenone (**Scheme 4.2**). The polymers were synthesised following the procedure reported by Toby *et al.*[135] An equimolar amounts of the EDN monomer and 4,4′-difluorobenzophenone were polymerized in the presence of K_2CO_3 in anhydrous DMAc and anhydrous toluene. The resulting polymer was then purified by reprecipitation from DMAc into methanol twice, affording the EDN-derived poly(ether-ether-ketone) (PEEK-EDN) as a light-brown solid. Similarly, EDN-derived poly(ether-ether-sulfone) (PES-EDN) was synthesised via the same procedure, using equimolar amounts of the EDN monomer and cheaply available 4,4′-difluorodiphenyl sulfone. The successful polymerisations were confirmed by FTIR and NMR analysis.

The FT-IR spectra of PEEK-EDN and PES-EDN are shown in **Figure 4.4**. Both spectra show characteristic peaks at 1590 cm^{-1} and 1490 cm^{-1} (aromatic C=C stretching), 1225 cm^{-1} (aromatic C–O–C stretching), and 1150 cm^{-1} (C–O–C stretching originating from EDN monomer), confirming the successful synthesis of PEEK-EDN and PES-EDN. The signal at 1655 cm^{-1} observed in PEEK-EDN corresponds to C=O stretching, while the peak at 1105 cm^{-1} observed in PES-EDN is attributed to the asymmetric S=O stretching.

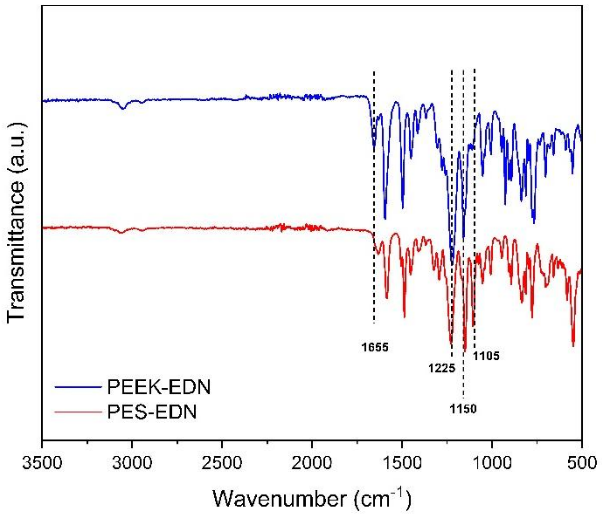

Figure 4.4 FT-IR spectra of PEEK-EDN and PES-EDN.

^{1}H NMR analysis further supports the FT-IR findings, confirming the chemical structure of each polymer (**Figure 4.5**). The bridgehead proton signal of PEEK-EDN was observed at 6.85 ppm, and the aromatic protons (Ar–H) appear in the range of 7.12–7.95 ppm. While the bridgehead proton signal of PES-EDN was observed at 6.70 ppm, and the aromatic protons (Ar–H) appear in the range of 7.03–8.00 ppm. It should be noted that part of the aromatic proton (Ar-H) signals may be overlapped by the solvent peak.

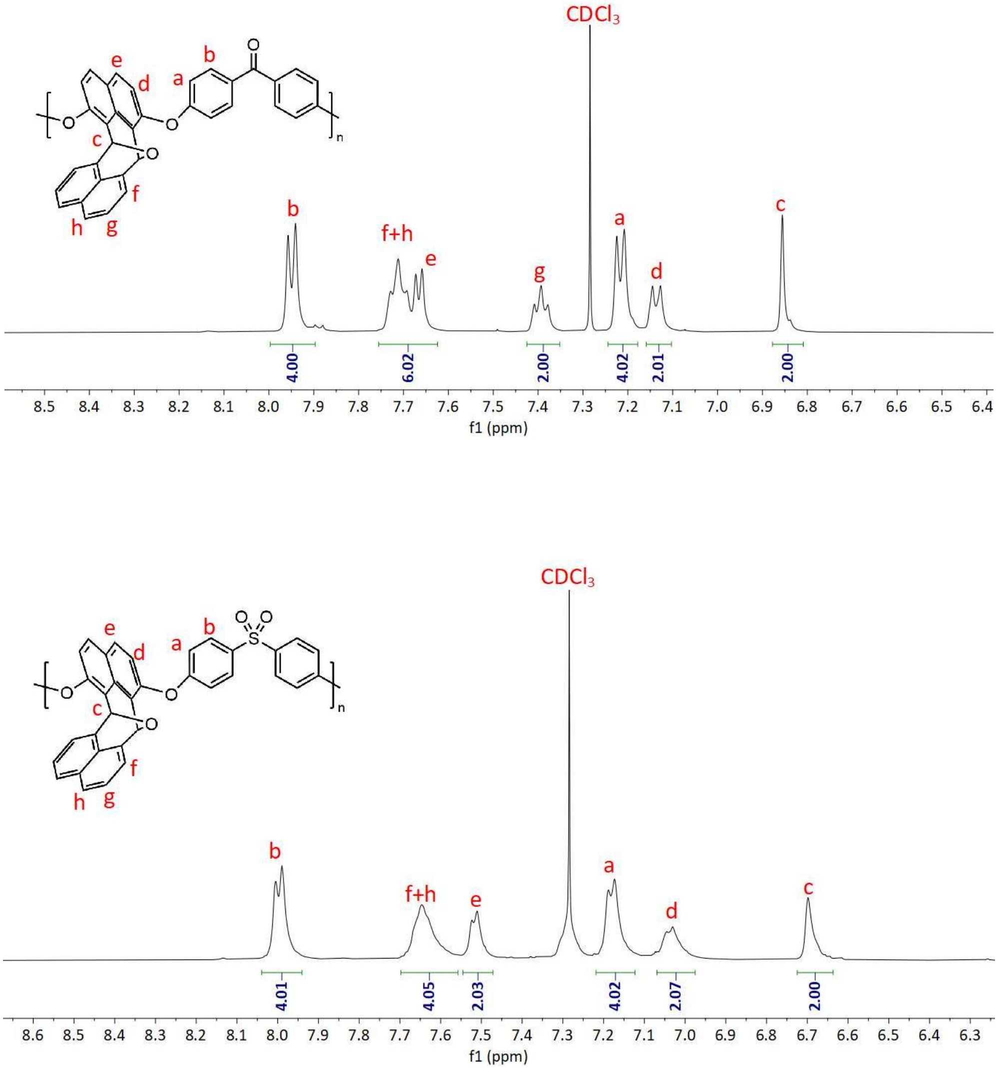

Figure 4.5 ^{1}H NMR of PEEK-EDN (top) and PES-EDN (bottom).

4.3 Physical properties and microporosity analysis of EDN polymers

Brunauer–Emmett–Teller (BET) analysis was used to evaluate the porosity of PEEK-EDN and PES-EDN. The N_2 adsorption-desorption isotherm of PES-EDN is presented in **Fig 4.6**, and the corresponding physical properties are summarised in **Table 4.1**. The data for PEEK-EDN is unavailable due to the ongoing maintenance problem of the gas adsorption instrument in our laboratory. PES-EDN shows a surface area (SA_{BET}) of only 39.73 m^2 g^{-1}, this value is significantly lower than that of traditional ladder-type PIMs (e.g., PIM-1 surface area: 709 m^2 g^{-1}). The N_2 isotherm of PES-EDN displays a type I profile (**Fig 4.6a**), characteristic of microporous materials, but with a low N_2 uptake at 77 K under low relative pressure ($P/P_0 < 0.1$).

Table 4.1 Physical properties of PEEK-EDN and PES-EDN.

Polymer	Solubility	SA_{BET}[a] (m^2 g^{-1})	V_{Total}[b] (ml g^{-1})	CO_2 uptake[c] (mmol g^{-1})
PEEK-EDN	Chloroform, NMP	-	-	-
PES-EDN	Chloroform, NMP	39.73	0.16	0.90

[a] BET surface area (SA_{BET}) was calculated from N_2 adsorption isotherm obtained at 77 K. [b] Total pore volume (V_{Total}) was estimated from N_2 adsorption at $P/P_o = 0.98$. [c] CO_2 uptake at 1 bar and 273 K.

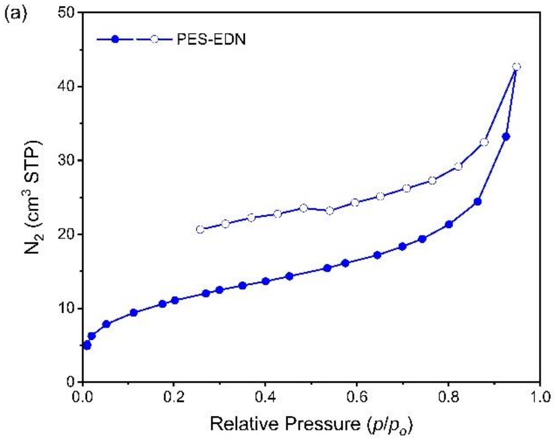

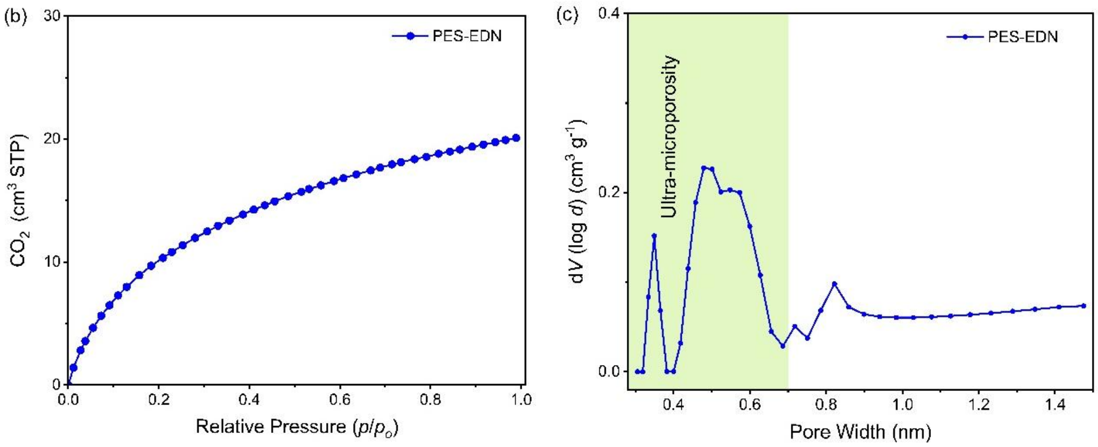

Figure 4.6 (a) N_2 adsorption isotherm at 77 K, (b) CO_2 adsorption isotherm at 273 K of PES-EDN, and (c) their pore size distributions (PSD) calculated from CO_2 adsorption data using non-local density functional theory (NLDFT) model.

The solubilities of the synthesised PEEK-EDN and PES-EDN were tested in different solvents, and both polymers exhibited good solubility in chloroform and NMP. Their solution processability was further examined by solution casting the polymers into thin films suitable for gas permeability measurements. Free standing films were successfully cast for both PEEK-EDN and PES-EDN, using chloroform as the solvent (**Figure 4.7**).

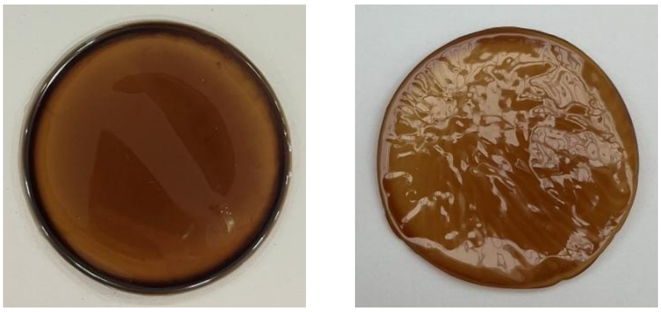

Figure 4.7 Solvent cast free-standing films of PEEK-EDN (left) and PES-EDN (right).

4.4 Gas transport property of EDN polymers

Single gas permeabilities were measured on freshly methanol-treated membranes. A comparison of gas permeability data for EDN polymers, PIM-1, and other reported PEEK polymers is summarised in **Table 4.2**. The gas permeability order for PEEK-EDN and PES-

EDN are H_2 > He > CO_2 > O_2 > N_2 > CH_4, whereas in PIM-1, CO_2 is most permeable. This indicates that PEEK-EDN and PES-EDN possess enhanced size-sieving properties, favouring the transport of smaller gas molecules. PEEK-EDN and PES-EDN exhibit a reduction in gas permeabilities coupled with an increase in gas selectivities for all gas pairs compared to PIM-1 (**Table 4.2**), following the trade-off relationship between gas permeability and selectivity.

Compared to other reported PEEK polymers (e.g., Am-PAFEK,[138] PEEK[139] and Ph-PEEK-3[139]), PEEK-EDN and PES-EDN exhibit similar gas permeabilities (O_2, N_2, CH_4 and CO_2), but higher gas selectivities for CO_2/CH_4, CO_2/N_2 and O_2/N_2. This is due to the unique structure of EDN that increases the backbone chain rigidity in the polymer and thus leads to improved gas selectivities.

Table 4.2 Gas permeabilities (P_A, Barrer) and ideal selectivities (P_A/P_B) of EDN polymers measured at 35 °C and 1 bar.

Polymer	Permeability (Barrer)[a]						Selectivity					
	N_2	O_2	CO_2	CH_4	H_2	He	CO_2/CH_4	CO_2/N_2	O_2/N_2	H_2/N_2	H_2/CH_4	He/N_2
PEEK-EDN	0.42	3.09	13.30	0.27	34.73	26.77	49.3	31.7	7.4	82.7	128.7	63.7
PES-EDN	0.76	4.52	25.90	0.68	50.96	38.63	38.1	34.1	5.9	67.1	74.9	50.8
PIM-1	653	2072	12211	1153	4930	1938	10.6	18.7	3.2	7.6	4.3	3.0
Am-PAFEK[138]	0.15	0.87	4.70	0.16	-	-	29.4	31.3	5.8	-	-	-
PEEK[139]	0.52	1.86	8.21	0.56	-	-	14.7	15.8	3.6	-	-	-
Ph-PEEK-3[139]	1.05	4.08	17.14	1.18	-	-	14.5	16.3	3.9	-	-	-

[a] 1 Barrer = 10^{-10} cm^3_{STP} cm cm^{-2} s^{-1} cm Hg^{-1}.

The diffusivity coefficients, solubility coefficients, diffusivity selectivities and solubility selectivities for PEEK-EDN and PES-EDN are listed in **Table 4.3** and **Table 4.4** to show the effect of EDN unit on the gas transport properties. The low gas permeability of EDN polymers is due to the low gas diffusivity coefficients for all gases (**Table 4.3**).

Table 4.3 Gas diffusion coefficients D (10^{-12} m^2s^{-1}) and diffusivity selectivities (D_A/D_B) of EDN polymers measured at 35 °C and 1 bar.

Polymer	*Diffusivity coefficient*						*Diffusivity selectivity*					
	N_2	O_2	CO_2	CH_4	H_2	He	CO_2/CH_4	CO_2/N_2	O_2/N_2	H_2/N_2	H_2/CH_4	He/N_2
PEEK-EDN	0.36	2.35	0.60	0.08	166.1	930	7.5	1.67	6.5	461	2076	2583
PES-EDN	0.73	4.31	1.12	0.14	243.7	1401	8.0	1.53	5.9	334	1741	1919
PIM-1	144	397	172	63.9	5525	7175	2.7	1.2	2.8	38.4	86.5	49.8

Table 4.4 Gas solubility coefficients S (cm^3_{STP} cm^{-3} bar^{-1}) and solubility selectivities (S_A/S_B) of EDN polymers measured at 35 °C and 1 bar.

Polymer	*Solubility coefficient*						*Solubility selectivity*					
	N_2	O_2	CO_2	CH_4	H_2	He	CO_2/CH_4	CO_2/N_2	O_2/N_2	H_2/N_2	H_2/CH_4	He/N_2
PEEK-EDN	0.88	0.98	16.66	2.63	0.16	0.02	6.3	18.9	1.1	0.18	0.06	0.02
PES-EDN	0.77	0.79	17.30	3.64	0.16	0.02	4.8	22.5	1.0	0.20	0.04	0.03
PIM-1	3.40	3.91	53.16	13.53	0.67	0.20	3.9	15.6	1.2	0.20	0.05	0.06

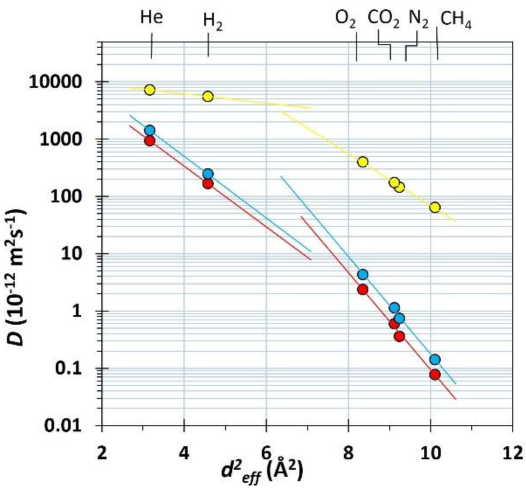

Figure 4.8 Correlation of diffusivity coefficients (D_A) with the square of the effective gas diameter (d^2_{eff}) (He = 1.78, H_2 = 2.14, O_2 = 2.89, CO_2 = 3.02, N_2 = 3.04, CH_4 = 3.18 Å) for freshly methanol treated films of PEEK-EDN (●), PES-EDN (●) and PIM-1 (●).

The diffusivity selectivity of small gases over large gases is higher than that of PIM-1, as illustrated by the correlation between the diffusivity coefficients (D_A) and the square of the effective gas diameter (d^2_{eff}) (**Fig. 4.8**). A clearly steeper slope of D_A versus d^2_{eff} is observed for EDN polymers compared to PIM-1, due to their enhanced size-sieving properties. The solubility selectivities of EDN polymers are similar to those of PIM-1 **(Table 4.4)**. Therefore, the higher diffusivity coefficients are the primary cause of the improved gas selectivities compared to PIM-1.

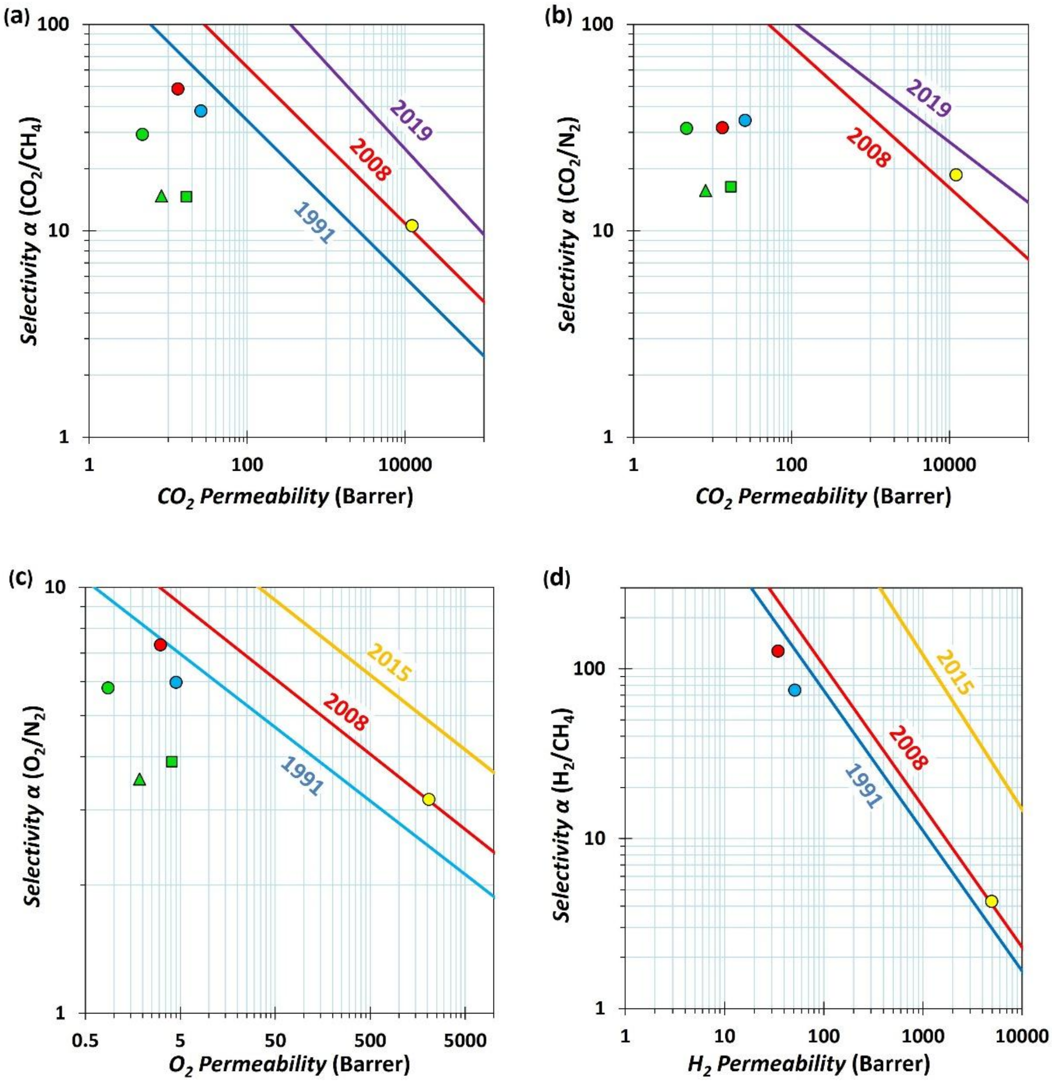

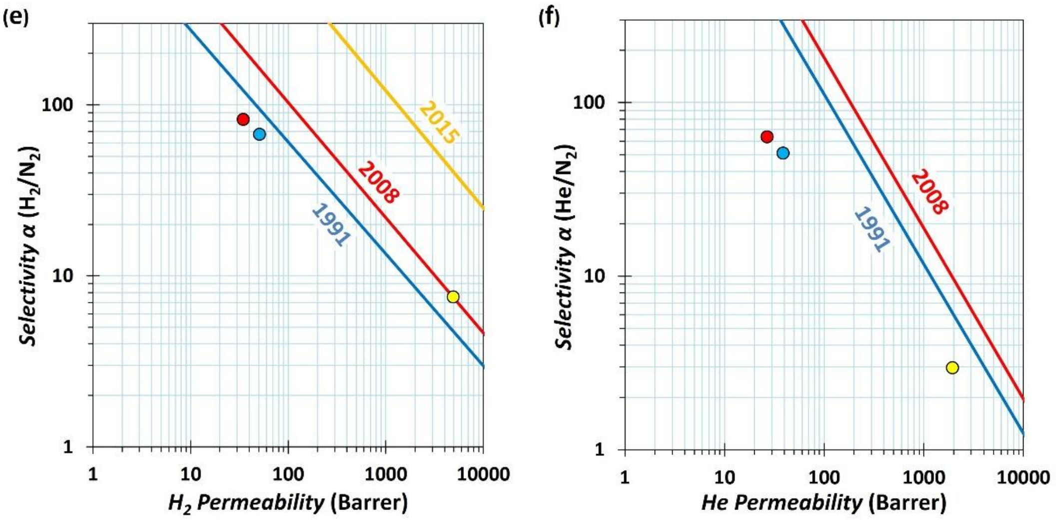

Figure 4.9 Robeson plots for the (a) CO_2/CH_4, (b) CO_2/N_2, (c) O_2/N_2, (d) H_2/CH_4, (e) H_2/N_2 and (f) He/N_2 gas pairs showing the position of the gas permeability data for freshly methanol treated films of PEEK-EDN (●), PES-EDN (●), PIM-1 (●), Am-PAFEK (●),[138] PEEK (▲)[139] and Ph-PEEK-3 (■).[139] The upper bounds are represented by blue lines (1991), red lines (2008), yellow lines for O_2/N_2, H_2/CH_4 and H_2/N_2 (2015), purple lines for CO_2/CH_4 and CO_2/N_2 (2019).

The data points for PEEK-EDN and PES-EDN are located close to the 1991 upper bound for CO_2/CH_4, O_2/N_2, H_2/N_2 and H_2/CH_4, whereas PIM-1 lies on the 2008 upper bound (**Figure 4.9**). EDN polymers exhibit higher gas selectivities for CO_2/CH_4, CO_2/N_2 and O_2/N_2, while maintaining comparable gas permeabilities to other PEEK polymers (Am-PAFEK, PEEK and Ph-PEEK-3). Therefore, the gas permeability data of EDN polymers shift upwards on the upper bound plot compared to other PEEK polymers.

Chapter 5: Synthesis of Functionalised Benzopleiadene via Intramolecular Friedel–Crafts Cycloalkylation

Since triptycene was first synthesized, great progress has been made in developing synthetic strategies and designing functional materials based on its unique structure.[109] The synthesis of functional triptycene derivatives still predominantly obtained through Diels–Alder reactions involving prefunctionalised anthracenes and either benzynes (Wittig's approach) or dienophiles (Bartlett's approach).[105, 140] These methods typically require multistep reactions and involve expensive starting materials and safety hazards in scaling up reactions that generate benzynes.[141-142] Consequently, the efficient and scalable synthesis of triptycene derivatives remains a significant challenge.

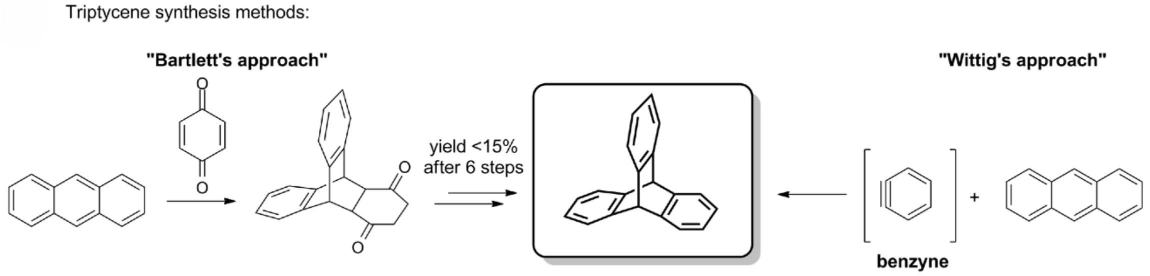

Figure 5.1 Representative synthetic routes to triptycene.[116] Reproduced from M. Woźny et al., Molecules 2021, 27, 250, licensed under CC BY 4.0.

5.1 Synthesis of dimethoxy-functionalised benzopleiadene (DMBP)

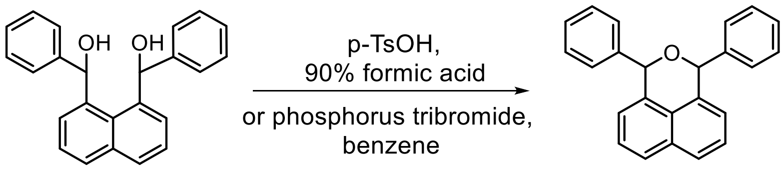

Scheme 5.1 The dehydration of 1,8-bis(phenylhydroxymethyl)naphthalene.

Letsinger *et al.* investigated the behaviour of 1,8-bis(phenylhydroxymethyl)naphthalene in acidic media and observed that the diol undergoes dehydration, resulting in the formation of a cyclic ether **(Scheme 5.1)**.[143]

Saitoh *et al.* reported the formation of a similar cyclic ether product derived from 1,8-disubstituted naphthalene using trifluoroacetic acid (TFA) as a catalyst **(Scheme 5.2)**. Subsequently, the use of 1,1,1,3,3,3-hexafluoro-2-propanol (HFIP) promoted deoxygenation of the cyclic ether, affording the desired dication.[144]

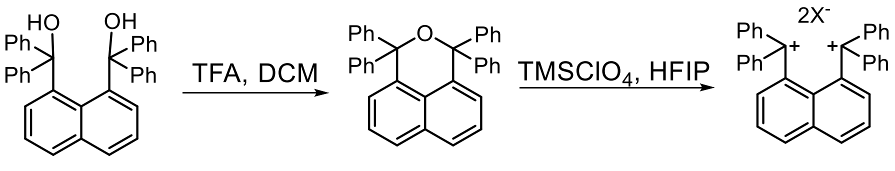

Scheme 5.2 Synthetic route of 1,8-bis(diphenylmethylium)naphthalene dication.

Barclay *et al.* found that 2,5-diphenylhexane-2,5-diol undergoes an intramolecular Friedel–Crafts cycloalkylation in the presence of aluminium chloride, leading to the formation of a bridged bicyclic structure, ethanoanthracene (EA), while nearly half of the product was identified as a cyclic ether formed via intramolecular dehydration **(Scheme 5.3)**.[145] Later, Malpass-Evans *et al.* reported a series of ethanoanthracene (EA) derivatives from aromatic-substituted diols via this double electrophilic aromatic substitution reaction.[146] Therefore, it was anticipated that a novel bridged bicyclic monomer, dimethoxy-functionalised benzopleiadene (DMBP), could be synthesised from readily accessible 1,8-disubstituted naphthalene via an intramolecular Friedel–Crafts cycloalkylation.

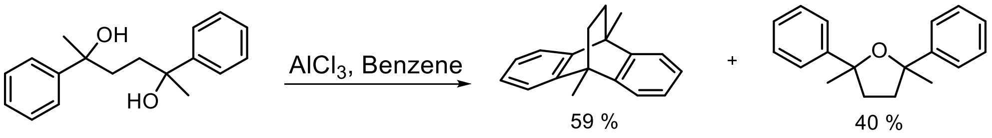

Scheme 5.3 Synthetic route of 9,10-substituted ethanoanthracene (EA) via intramolecular Friedel–Crafts cycloalkylation.

The required 1,8-benzoyl-2,7-dimethoxynaphthalene precursor **(17)** was prepared by a P_2O_5-MsOH (Eaton's reagent) mediated direct condensation of 2,7-dimethoxynaphthalene with benzoic acid.[147] The target monomer **(Scheme 5.4)** dimethoxy-functionalized benzopleiadene (DMBP) **(19)** was synthesised via reduction of precursor **(17)**, followed by an intramolecular Friedel–Crafts cyclialkylation of the corresponding diol **(18)**. The precursor **(17)** was reduced by lithium aluminium hydride ($LiAlH_4$), while the use of sodium borohydride ($NaBH_4$) proved ineffective, resulting in the recovery of starting material.

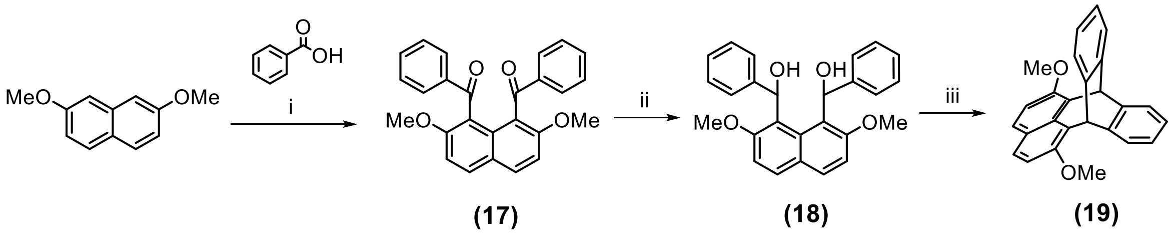

Scheme 5.4 The synthesis of monomer DBMP **(19)**. Reagent and conditions. i) Benzoic acid, P_2O_5-MsOH, 60 °C, 3h; ii) $LiAlH_4$, dry THF, rt, 15 h; iii) hexafluoro-2-propanol (HFIP), anhydrous $AlCl_3$, dry DCM, N_2, rt, 10 min.

The obtained DBMP **(19)** monomer was analysed by ^1H NMR spectroscopy (**Figure 5.2**), where the presence of characteristic bridgehead protons at 6.16 ppm strongly indicates the successful formation of the DBMP **(19)** monomer. The X-ray crystal structure (**Figure 5.3**) provides further confirmation of the bridged bicyclic structure of DMBP **(19)** monomer.

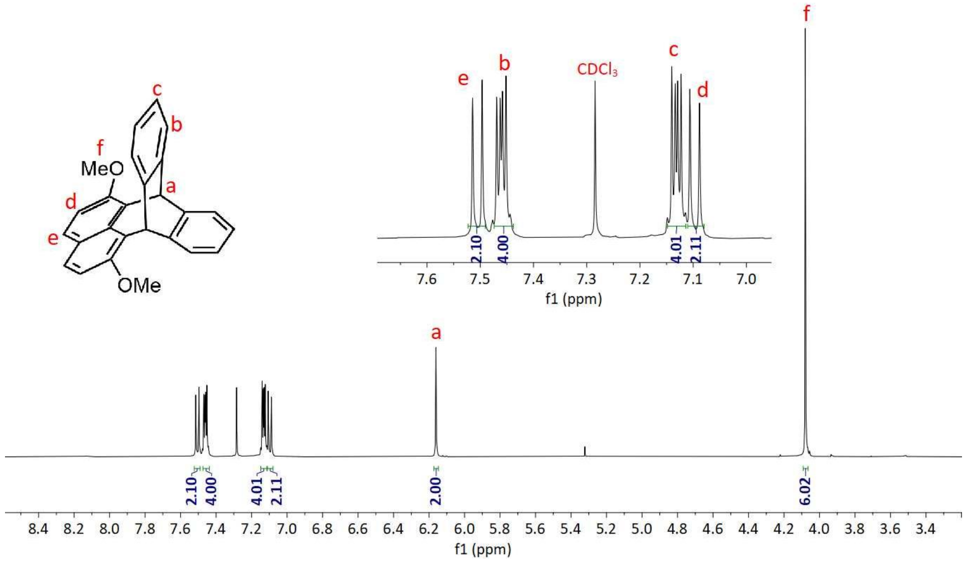

Figure 5.2 ^1H NMR of the DBMP **(19)** monomer and its X-ray crystal structure.

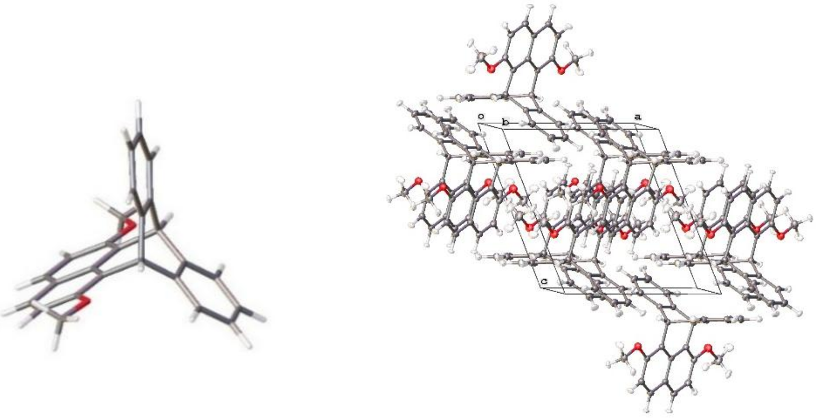

Figure 5.3 X-ray crystal structure and molecular packing of (DBMP) **(19)**. The crystal packing image shows an ordered π–π stacking along the main chain, while the methoxy groups extend into the interlayer space.

The DBMP **(19)** was then demethylated to obtain the dihydroxyl-functionalised monomer DHBP **(20)**. The demethylation reaction was performed using boron tribromide (BBr_3) in anhydrous DCM **(Scheme 5.5)**. DHBP **(20)** was obtained as a white solid with a yield of 85%. The successful demethylation was confirmed by the disappearance of -OMe peak in the ^{1}H NMR at 4.08 ppm, and the appearance of -OH peak at 9.75 ppm (**Figure 5.4**).

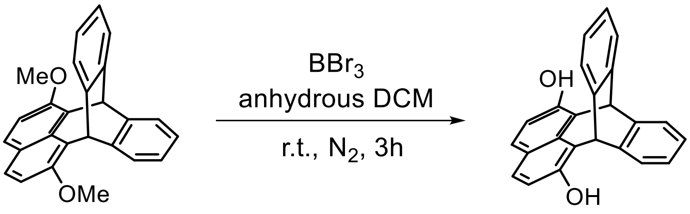

(19) **(20)**

Scheme 5.5 Demethylation of DMBP **(19)**.

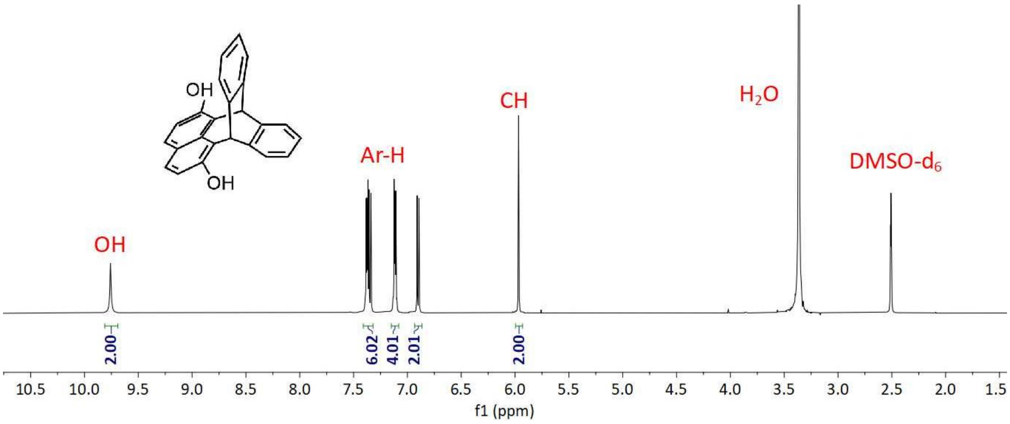

Figure 5.4 ^{1}H NMR of DHBP monomer **(20)**.

5.2 Synthesis of Poly(arylene ether nitrile) (PEN)

In addition to PEEK and PES discussed in **Chapter 4**, poly(arylene ether nitrile) (PEN) is another typical poly(arylene ether)s (PAEs) polymer. In this section, PEN based on DHBP and 2,6-difluorobenzonitrile (DFBN) as monomers was synthesised by the reaction of DHBP and DFBN in the presence of anhydrous DMF and K_2CO_3 under N_2 protection. The crude product was then purified by refluxing in methanol, affording the PEN-DHBP as a white powder **(Scheme 5.6)**. The solubility of the synthesised PEN-DHBP was tested in various solvents, however, it was found to be insoluble in common organic solvents such chloroform, THF, DMF, DMSO and NMP.

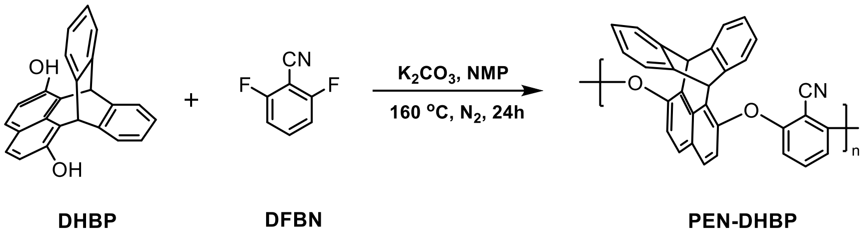

Scheme 5.6 Synthesis of PEN-DHBP.

The FTIR spectra of DHBP monomer and PEN-DHBP polymer are shown in **Figure 5.5**. The successful formation of PEN-DHBP was confirmed by FTIR analysis, as evidenced by the disappearance of the broad O-H stretching vibration at 3335 cm^{-1} and the appearance of two new peaks at 2230 cm^{-1} and 1030 cm^{-1}, corresponding to the C≡N stretching and the aromatic C-O-C stretching vibrations, respectively. The peak observed at 3021 cm^{-1} is attributed to the aromatic C-H stretching.

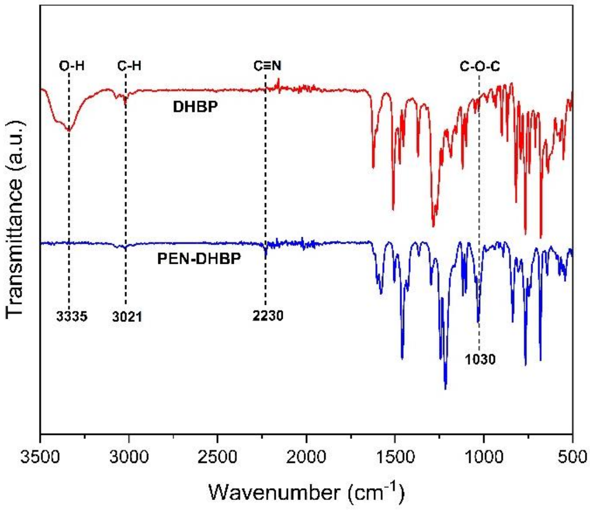

Figure 5.5 FTIR spectra of DHBP and PEN-DHBP.

5.3 Physical properties and microporosity analysis

The N_2 adsorption-desorption isotherm of PEN-DHBP is presented in **Fig 5.6a**. PEN-DHBP exhibits very low N_2 adsorption at low relative pressure ($P/P_0 < 0.1$), with a low apparent BET surface area of 86 m^2 g^{-1}. The distinct hysteresis between the adsorption and desorption isotherm can be attributed to swelling of the polymer during N_2 adsorption.

Fig 5.6b illustrates the CO_2 adsorption isotherm at 273 K for PEN-DHBP, and its pore size distribution (PSD) was calculated using the density functional theory (DFT) model. PEN-DHBP exhibits a significant CO_2 uptake of 22 cm^3/g, indicating a high concentration of ultramicropores (< 0.7 nm) in PEN-DHBP. The PSD curve further supports the great concentration of ultramicropores in PEN-DHBP (**Fig 5.6c**).

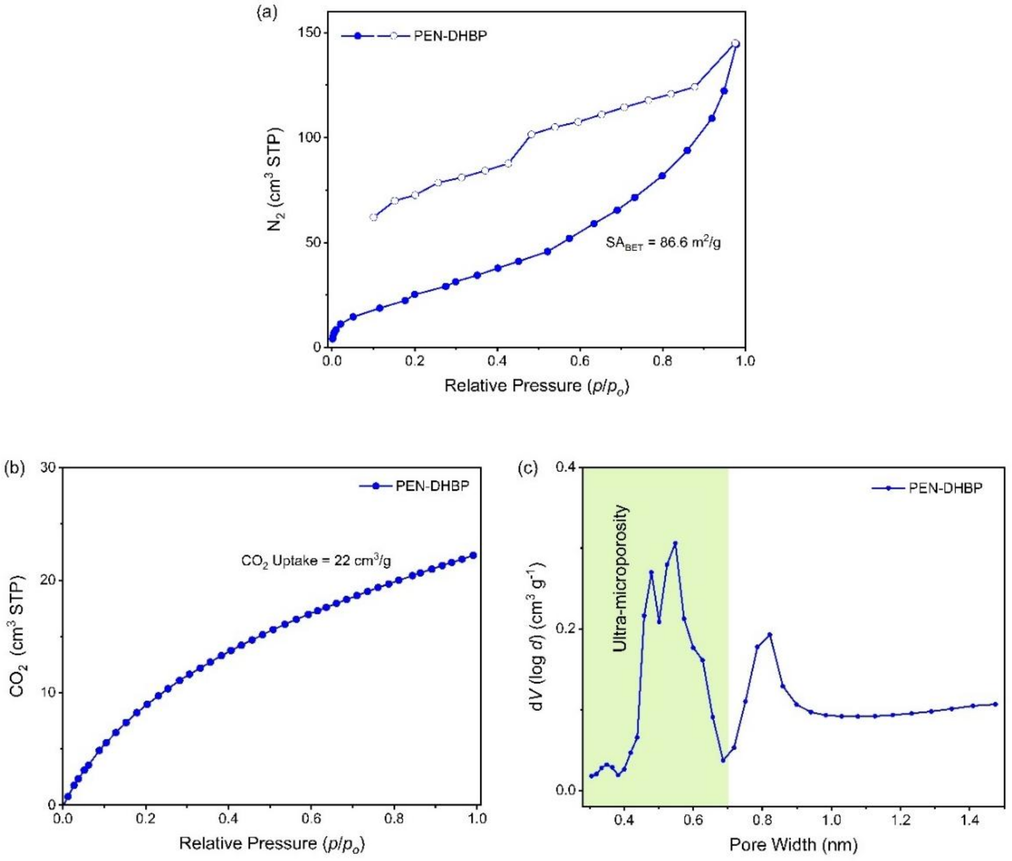

Figure 5.6 (a) N_2 adsorption isotherm at 77 K, (b) CO_2 adsorption isotherm at 273 K of PEN-DHBP, and (c) their pore size distributions (PSD) calculated from CO_2 adsorption data using non-local density functional theory (NLDFT) model.

Chapter 6: Conclusion

In chapter 2, three naphthopleiadene (NP)-based monomers (BNP, DMNP and TEGNP) were synthesised by introducing various functional groups onto the initial NP structure. Subsequently, a series of copolymers (PIM-BNP$_x$, PIM-DMNP$_x$ and PIM-TEGNP$_x$) based on these NP monomers were prepared. The substitution with different functional groups on the NP scaffold enabled modification of the polymer backbone, so that we could tune the physical and microporous properties. Among these polymers, copolymers PIM-BNP$_x$ and PIM-DMNP$_x$ exhibits large BET surface area, high CO_2 uptake and intrinsic microporosity. Robust self-standing films were obtained from these NP-based copolymers. The prepared films of these copolymers have been to Institute on Membrane Technology, National Research Council of Italy (CNR-ITM) for gas separation studies.

In chapter 3, benzopleiadene (BP), a novel bridged bicyclic framework composed of two catechol units and a single naphthalene core fused at two bridgehead carbon atoms, was designed and synthesised. BP proved to be an excellent building block for constructing PIMs with high gas separation performance. The unique structure of BP provides polymers with high chain rigidity and ultramicropores and thus leads to enhanced gas separation performance. In particular, PIM-BP homopolymer and PIM-BP$_{75}$ copolymer exhibit outstanding separation performance for gas pairs CO_2/CH_4, CO_2/N_2 and O_2/N_2, comparable to those of the upper bound-defining PIM-Btrip. These make PIM-BP and PIM-BP$_{75}$ great potential materials for energy-efficient applications, such as natural gas or biogas upgrading (CO_2/CH_4), post-combustion carbon capture (CO_2/N_2) and oxygen or nitrogen enrichment of air (O_2/N_2). The amidoxime-functionalised polymer (AO-PIM-BP) exhibits exceptional size-sieving properties. The ultra-high gas selectivity combined with high permeability positions AO-PIM-BP above the 2015 upper bounds for O_2/N_2, H_2/N_2 and H_2/CH_4. These make AO-PIM-BP a promising candidate for hydrogen economy applications such as hydrogen recovery from gas mixtures like H_2/N_2 and H_2/CH_4.

In chapter 4, a novel aryl ether-bridged dinaphthalene (EDN) monomer, structurally similar to the NP scaffold, was synthesised. The EDN mmonomer was used to prepare the linear polymers (PEEK-EDN and PES-EDN), from which robust self-standing films were successfully obtained. Both PEEK-EDN and PES-EDN demonstrate exceptional selectivities for CO_2/CH_4, H_2/N_2 and H_2/CH_4.

In chapter 5, a novel dimethoxy-functionalised benzopleiadene (DMBP) monomer, structurally based on the BP scaffold, was synthesised via an intramolecular Friedel–Crafts cycloalkylation. Dihydroxyl-functionalised monomer DHBP was synthesised via demethylation of DMBP. The potential use in polymer of DHBP was investigated. The potential of DHBP for polymer synthesis was investigated, and the resulting polymer, PEN-DHBP, was characterised as a microporous material.

Chapter 7: Future work

The gas permeability will be measured for copolymers PIM-BNP$_x$, PIM-DMNP$_x$ and PIM-TEGNP$_x$ that successfully form robust self-standing films. It is of great interest to investigate the impact of these functionalised NP monomers on the gas permeability of the resulting polymers. In addition, the copolymers PIM-BNP$_x$ and PIM-DMNP$_x$ demonstrate great concentration of ultra-micropores as well as high BET surafece, so it is anticipated that these copolymers will show potential for efficient gas separations.

Benzopleiadene (BP) has proven to be an excellent building block for constructing PIMs with high gas separation performance. Though BP was synthesised via simple one-step reaction, the yield is relatively low and requires column chromatography for purification. Therefore, optimisation of the reaction conditions will be carried out to obtain BP more efficiently. The N_2 and CO_2 adsorption isotherms will be measured for amidoxime-functionalised polymer (AO-PIM-BP) to analyse its microporosity properties. The diffusivity coefficients and solubility coefficients will be measured for all BP-based polymers to investigate their gas transport behaviours.

Unfortunately, the DHBP-based PEN was insoluble in common organic solvents, therefore, future work could optimism the polymerisation conditions of the PEN-DHBP to obtain polymers with good solution processibility. And then, attempts could be made to obtain robust self-standing films from PEN-DHBP suitable for gas permeability measurements.

Chapter 8: Experimental

8.1 Techniques

All reagents were purchased from commercial sources and used without further purification unless stated otherwise. Anhydrous N, N-dimethylformamide (DMF) and dimethylacetamide (DMAc) were purchased from Sigma-Aldrich. Dry dichloromethane (DCM), tetrahydrofuran (THF) and toluene were obtained from a Solvent Purification System (SPS facility). All air sensitive reactions were carried out under a nitrogen atmosphere using oven-dried apparatus. Thin-layer chromatography (TLC) was performed using aluminium-back plates coated with Merck Kieselgel 60 GF254. Column chromatography was conducted using silica gel (60 Å, 40-63 µm) chromatography grade from Fischer Scientific.

Melting points (MP)

Melting points were recorded using Stuart Digital Melting Point Apparatus with a maximum temperature of 300 °C and were uncorrected.

Fourier Transform Infrared Spectroscopy (FTIR)

Infrared transmission spectra of the powder or liquid samples were recorded using a Shimadzu IR Affinity-1S FTIR spectrophotometer in the range of 4000-400 cm^{-1}.

Nuclear Magnetic Resonance (NMR)

^{1}H NMR spectra were recorded in a suitable deuterated solvent using Avance Bruker AVA500 (500 MHz) or PRO500 (500 MHz) at 298K unless stated at a specific temperature, with ^{13}C NMR recorded at 125 MHz or 126 MHz respectively.

Mass Spectrometry (MS)

High-resolution mass spectrometry (HRMS) was performed by using a Fisonsn VG platform II quadruple instrument plus Thermos Finnigan MAT 900 XP, electron ionisation sector MS utilising electron impact (EI).

Breunauer-Emmett-Teller (BET) surface areas

Low-temperature N_2 (77 K) and CO_2 (273 K) adsorption/desorption isotherms were obtained using a Quantachrome Quadrasorb automated surface area analyser. Accurately weighed polymer samples (100 mg) were degassed for 12 hours under high vacuum at 110 °C prior to analysis.

8.2 Synthesis of Monomers

Naphthalene-2,3-dicarboxaldehyde (1)

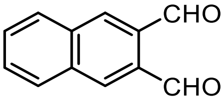

The compound naphthalene-2,3-dicarboxaldehyde **(1)** was synthesised according to the procedure reported by Mallouli *et al.*[148] A mixture of *o*-phthalaldehyde (10 g, 74.6 mmol), 2,5 dimethoxytetrahydrofuran (9.9 g, 74.6 mmol), acetic acid (5 ml), water (7.5 ml) and piperidine (5 drops) was refluxed for 12 hours. After cooling to room temperature, the resulting orange precipitate was filtered, washed with hydrochloric acid (10%), water and diethyl ether. Sublimation (130 °C) of the solid gave pale yellow needle-shaped crystals (3.4 g, 25%). Mp: 130 °C (Lit[148] 132 °C); FTIR (v, cm^{-1}): 3056, 2910, 2855, 1675; ^1H NMR (500 MHz, $CDCl_3$) δ 10.65 (s, 2H, CHO), 8.45 (s, 2H, Ar-H), 8.08 (m, 2H, Ar-H), 7.77 (m, 2H, Ar-H); ^{13}C NMR (125 MHz, $CDCl_3$) δ 192.49, 134.44, 132.86, 130.04, 129.66.

Tetrahydroxy-naphthopleiadene (BNP) (2)[103]

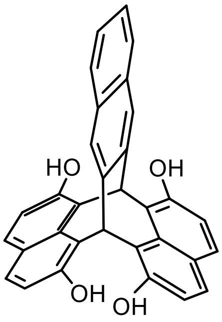

A solution of naphthalene-2,3-dicarboxaldehyde **(1)** (1 g, 5.43 mmol), 2,7-dihydroxynaphthalene (1.74 g, 10.86 mmol) and conc. HCl (1 ml) in methanol (20 ml) was heated at reflux for 5 h. After cooling to room temperature, the resulting precipitate was filtered, washed with water and methanol to afford **(2)** as white solid (2.3 g, 4.91 mmol, 90%). Mp: >300 °C; FTIR (ν, cm^{-1}): 3646, 3179, 1620, 1518, 1445; ^{1}H NMR (500 MHz, DMSO-d$_6$) δ 9.96 (s, 4H, OH), 7.92 (s, 2H, ArH), 7.86 (dd, J = 6.2, 3.2 Hz, 2H, ArH), 7.46 (d, J = 8.7 Hz, 4H, ArH), 7.40 (dd, J = 6.3, 3.2 Hz, 2H, ArH), 7.08 (s, 2H, CH), 6.96 (d, J = 8.7 Hz, 4H, ArH); ^{13}C NMR (125 MHz, DMSO-d$_6$) δ 152.12, 140.88, 134.03, 133.01, 128.99, 127.51, 126.24, 125.97, 125.16, 120.74, 115.60; HRMS (EI, m/z): [M+H]$^+$ calculated for $C_{32}H_{21}O_4$: 469.1434, found: 469.1433.

X-ray Crystallography: $C_{33.5}H_{26}O_{5.5}$, M_r = 516.54, triclinic, P-1 (No. 2), a = 10.4986(5) Å, b = 11.6083(6) Å, c = 12.2425(6) Å, α = 97.683(4)°, β = 106.716(4)°, γ = 100.894(4)°, V = 1374.87(12) Å^3, T = 120.01(10) K, Z = 2, Z' = 1, μ (Mo K$_\alpha$) = 0.084, 36195 reflections measured, 6729 unique (R_{int} = 0.0431) which were used in all calculations. The final wR_2 was 0.1457 (all data) and R_1 was 0.0598 (I≥2 σ(I)).

5,6-Dimethoxyisobenzofuran-1(3H)-one (3)

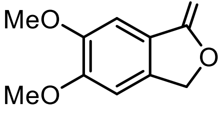

3,4-Dimethoxybenzoic acid (10 g, 54.89 mmol) and paraformaldehyde (16.47 g, 0.55 mol) were dissolved in 300 ml of conc. HCl (37%), and the mixture was heated at 80 °C for 6 h. The reaction mixture was cooled with an ice bath and then neutralized with aqueous ammonia solution (25%). The beige precipitate obtained was filtered, washed with water, and recrystallized from ethanol to yield **(3)** as white crystals (7.46 g, 38.42 mmol, 70%). Mp: 155 °C (Lit[149] 155 °C); FTIR (*v*, cm^{-1}): 3090, 3015, 2935, 2875, 2836, 1747, 1607, 1504, 1445, 1342, 1293, 1225; ^1H NMR (500 MHz, $CDCl_3$) δ 7.33 (s, 1H, Ar-H), 6.92 (s, 1H, Ar-H), 5.24 (s, 2H, CH_2), 4.00 (s, 3H, OCH_3), 3.96 (s, 3H, OCH_3); ^{13}C NMR (125 MHz, $CDCl_3$) δ 171.45, 154.91, 150.50, 141.06, 117.72, 106.20, 103.45, 69.16, 56.41, 56.30.

4,5-Dimethoxy-1,2-benzenedimethanol (4)

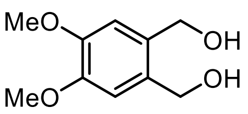

To a solution of 5,6-dimethoxyisobenzofuran-1(3H)-one **(3)** (7.4 g, 38.11 mmol) in dry THF (200 ml) was added $LiAlH_4$ (2.89g, 76.22 mmol) in small portions at 0 °C. The reaction mixture was heated to reflux for 4 h. After cooling to room temperature, the reaction was carefully quenched at 0°C by addition of water (3 ml), 15% NaOH solution (3 ml) and water (9 ml). Some anhydrous Na_2SO_4 was added to the mixture and stirred at room temperature for 10 min, then filtered through Celite. The solvent was removed under reduced pressure to yield **(4)** as colourless solid (6.9 g, 34.81 mmol, 91%). Mp: 108 °C (Lit[150] 108-109 °C); FTIR (*v*, cm^{-1}): 3457, 3331, 3004, 2971, 2925, 2850, 1612, 1511, 1450, 1284, 1209, 1100; ^1H NMR (500 MHz, DMSO-d_6) δ 6.99 (s, 2H, Ar-H), 4.98 (t, 2H, OH), 4.48 (d, 4H, CH_2); ^{13}C NMR (125 MHz, DMSO-d_6) δ 147.71, 132.25, 112.17, 60.63, 56.04.

4,5-Dimethoxyphthalaldehyde (5)

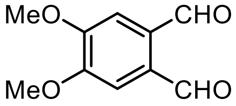

At -78 °C, a solution of DMSO (5.52 g, 70.63 mmol) in dry DCM (20 ml) was added dropwise to a solution of oxalyl chloride (5.64 g, 44.40 mmol) in dry DCM (100 ml). The resulting mixture was stirred for 10 min after the addition of DMSO was completed. A solution of diol **(4)** (4 g, 20.18 mmol) in dry DCM (60 ml) was added slowly and stirred for 60 min at -78 °C. Triethylamine (42.19 ml, 302.7 mmol) was added dropwise at -78 °C and then stirred for additional 60 min at room temperature. The reaction mixture was carefully quenched by addition of water (200 ml) and extracted with DCM. The combined organic layers were dried over Mg_2SO_4, and the solvent was removed under reduced pressure. The resulting solid was washed with sufficient water and then a small amount of ether to yield the aldehyde **(5)** as white solid (3.4 g, 17.51 mmol, 86%). Mp: 163 °C (Lit[151] 161.5-162.5 °C); FTIR (*ν*, cm^{-1}): 3080, 2988, 2920, 2855, 1674, 1570, 1500, 1452, 1276, 1220; ^1H NMR (500 MHz, $CDCl_3$) δ 10.60 (s, 2H, CHO), 7.48 (s, 2H, Ar-H), 4.04 (s, 6H, OCH_3); ^{13}C NMR (125 MHz, $CDCl_3$) δ 190.10, 153.22, 131.06, 111.63, 56.50.

Tetrahydroxy-naphthopleiadene (DMNP) (6)

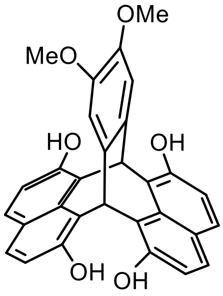

A solution of 4,5-dimethoxyphthalaldehyde **(5)** (1 g, 5.15 mmol), 2,7-dihydroxynaphthalene (2.06 g, 12.88 mmol) and trifluoromethanesulfonic acid (0.5 ml) in AcOH (25 ml) was heated at reflux for 6 h. After cooling to room temperature, the reaction mixture was poured into a mixture of methanol and water (100 ml, v/v:1/1), the resulting precipitate was filtered, washed with water and methanol to afford **(6)** as pale purple solid (1.85 g, 3.86 mmol, 75%). Mp: >300 °C; FTIR (*ν*, cm^{-1}): 3212, 2956, 1836, 1613, 1518, 1320, 1221; ^1H NMR (500 MHz, DMSO-d_6) δ 9.95 (s, 4H, OH), 7.47 (d, *J* = 8.7 Hz, 4H, ArH), 6.96 (d, *J* = 8.7 Hz, 6H, ArH), 6.65 (s, 2H, CH), 3.73 (s, 6H, OCH_3); ^{13}C NMR (125 MHz, DMSO-d_6) δ 151.71, 147.96, 134.12, 133.84, 129.01, 125.38, 120.74, 115.60, 112.93, 56.22, 38.84; HRMS (EI, m/z): $[M+H]^+$ calculated for $C_{30}H_{23}O_6$: 479.1489, found: 479.1481.

X-ray Crystallography: $C_{31}H_{26}O_7$, M_r = 510.52, monoclinic, $P2_1/c$ (No. 14), a = 16.64378(17) Å, b = 16.7892(2) Å, c = 8.51493(7) Å, β = 97.0723(8)°, $\alpha = \gamma$ = 90°, V = 2361.27(4) Å^3, T = 100.01(10) K, Z = 4, Z' = 1, μ(Cu K_α) = 0.835, 30812 reflections measured, 4952 unique (R_{int} = 0.0272) which were used in all calculations. The final wR_2 was 0.0977 (all data) and R_1 was 0.0375 ($I \geq 2\sigma(I)$).

5,6-Dihydroxyisobenzofuran-1(3H)-one (7)

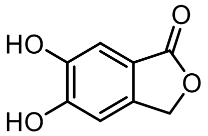

To a solution of 5,6-dimethoxyisobenzofuran-1(3H)-one **(3)** (5 g, 25.75 mmol) in anhydrous DCM (50 ml) under N_2 atmosphere, cooled to 0 °C, BBr_3 (9.68 g, 38.63 mmol) was added dropwise. The reaction mixture was allowed to warm up to room temperature and stirring for 3 h. The reaction mixture was poured into ice water and extracted with EtOAc. The combined organic layers were dried over anhydrous Na_2SO_4, and the solvent was removed under reduced pressure to yield the product **(7)** as white solid (3.5 g, 21.07 mmol, 82%). Mp: 258 °C; FTIR (ν, cm^{-1}): 3410, 3159, 1703, 1605, 1516; ^{1}H NMR (500 MHz, DMSO-d_6) δ 10.20 (s, 1H, Ph-OH), 9.67 (s, 1H, Ph-OH), 7.07 (s, 1H, Ar-H), 6.93 (s, 1H, Ar-H), 5.17 (s, 2H, CH_2); ^{13}C NMR (125 MHz, DMSO-d_6) δ 171.39, 152.79, 147.16, 140.82, 115.90, 109.92, 108.62, 69.32.

Tri(ethylene glycol) monomethyl ether tosylate (8)[152]

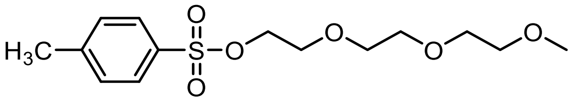

Triethylene glycol monomethyl ether (20 g, 121.8 mmol) was dissolved in THF (60 ml) at 0 °C. NaOH (9.75 g, 243.6 mmol) in 60 ml water was added dropwise to the THF solution. Tosylchloride (30.2 g, 158.41 mmol) in 60 ml THF was then added slowly to the mixture at 0 °C. The mixture was allowed to warm up to room temperature and stirred for 15 h. The resulting aqueous solution was extracted with diethyl ether (3 x 50 ml), and the combined organic layer was washed with water, brine and dried over anhydrous Na_2SO_4. The solvent was removed under reduced pressure to afford **(8)** as colourless liquid (35 g, 110 mmol, 90%). ^1H NMR (500 MHz, $CDCl_3$) δ 7.81 (d, 2H, Ar-H), 7.35(d, 2H, Ar-H), 4.17 (m, 2H, OCH_2), 3.69 (m, 2H, OCH_2), 3.61 (m, 6H, OCH_2), 3.53 (m, 2H, OCH_2), 2.45 (s, 3H, CH_3); ^{13}C NMR (125 MHz, $CDCl_3$) δ 144.79, 133.04, 129.82, 127.97, 71.91, 70.74, 70.56, 70.54, 69.24, 68.67, 59.01, 21.62.

5,6-bis(tri(ethylene glycol) monomethyl ether) isobenzofuran-1(3H)-one (9)

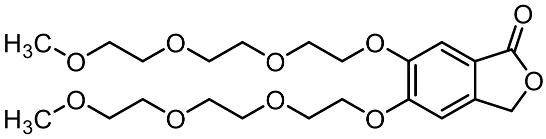

A mixture of 5,6-dihydroxyisobenzofuran-1(3H)-one **(7)** (2 g, 12.04 mmol), Tri(ethylene glycol) monomethyl ether tosylate **(8)** (9.6 g, 30.1 mmol), K_2CO_3 (8.32 g, 60.2 mmol) and anhydrous DMF (80 ml) was attired at 90 °C under N_2 atmosphere overnight. After cooling to room temperature, the mixture was concentrated under reduced pressure. The residues were dissolved in 100 ml DCM and washed with brine (50 ml x 3). The combined organic layers were collected and dried over anhydrous Na_2SO_4, and the solvent was removed under reduced pressure. The crude product was purified by silica gel column chromatography DCM/MeOH (98:2 v/v) to afford the product **(9)** as colourless liquid (3.31 g, 7.2 mmol, 60%). FTIR (*v*, cm^-

^{1}): 2869, 1750, 1670, 1504, 1454, 1342, 1288, 1100; ^{1}H NMR (500 MHz, $CDCl_3$) δ 7.09 (s, 1H, Ar-H), 6.81 (s, 1H, Ar-H), 5.03 (s, 2H, CH_2), 4.06 (m, 2H, CH_2), 4.01(m, 2H, CH_2), 3.73 (m, 4H, CH_2), 3.58 (m, 4H, CH_2), 3.48 (m, 8H, CH_2), 3.36 (m, 4H, CH_2), 3.19 (d, J = 2.0 Hz, 6H, OCH_3); ^{13}C NMR (125 MHz, $CDCl_3$) δ 171.18, 154.55, 149.84, 141.30, 117.48, 108.18, 105.57, 71.75, 71.73, 70.76, 70.74, 70.49, 70.34, 70.31, 69.31, 69.21, 69.07, 68.88, 58.76.

4,5-Bis(tri(ethylene glycol) monomethyl ether)-1,2-benzenedimethanol (10)

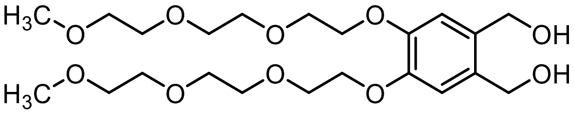

To a solution of 5,6-bis(tri(ethylene glycol) monomethyl ether) isobenzofuran-1(3H)-one **(9)** (5 g, 10.91 mmol) in dry THF (100 ml) was added $LiAlH_4$ (0.83 g, 21.82 mmol) in small portions at 0 °C. The reaction mixture was heated to reflux for 4 h. After cooling to room temperature, the reaction was carefully quenched at 0°C by addition of water (1 ml), 15% NaOH solution (1 ml) and water (3 ml). Some anhydrous Na_2SO_4 was added to the mixture and stirred at room temperature for 10 min, then filtered through Celite. The solvent was removed under reduced pressure to yield **(10)** as colourless liquid (4.15g, 8.97 mmol, 82%). FTIR (v, cm^{-1}): 3400, 2869, 1610, 1512, 1450, 1280, 1100; ^{1}H NMR (500 MHz, DMSO-d_6) δ 7.02 (s, 2H, Ar-H), 4.98 (t, J = 5.5 Hz, 2H, OH), 4.47 (d, J = 5.5 Hz, 4H, CH_2), 4.09 (m, 4H, CH_2), 3.75 (m, 4H, CH_2), 3.62 (m, 4H, CH_2), 3.54 (m, 8H, CH_2), 3.45 (m, 4H, CH_2), 3.26 (s, 6H, OCH_3); ^{13}C NMR (125 MHz, DMSO-d_6) δ 147.39, 132.99, 114.76, 71.78, 70.48, 70.34, 70.11, 69.58, 69.02, 60.64, 58.49.

4,5-Bis(tri(ethylene glycol) monomethyl ether)phthalaldehyde (11)

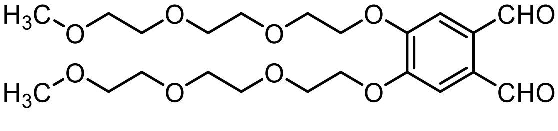

At -78 °C, a solution of DMSO (4.73 g, 60.55 mmol) in dry DCM (18 ml) was added dropwise to a solution of oxalyl chloride (4.83 g, 38.06 mmol) in dry DCM (80 ml). The resulting mixture was stirred for 10 min after the addition of DMSO was completed. A solution of diol **(10)** (8 g, 17.30 mmol) in dry DCM (40 ml) was added slowly and stirred for 60 min at -78 °C. Triethylamine (36 ml, 259.5 mmol) was added dropwise at -78 °C and then stirred for additional 60 min at room temperature. The reaction mixture was carefully quenched by addition of water (200 ml) and extracted with DCM. The combined organic layers were dried over Mg_2SO_4, and the solvent was removed under reduced pressure. The aldehyde **(11)** was obtained as colourless liquid (6.9 g, 17.05 mmol, 87%). FTIR (ν, cm^{-1}): 2874, 2613, 2501, 1680, 1580, 1517, 1450, 1284, 1100; ^1H NMR (500 MHz, $CDCl_3$) δ 10.54 (s, 2H, CHO), 7.51 (s, 2H, Ar-H), 4.32 (m, 4H, CH_2), 3.92 (m, 4H, CH_2), 3.75 (m, 4H, CH_2), 3.66 (m, 8H, CH_2), 3.54 (m, 4H, CH_2), 3.37 (s, 6H, OCH_3); ^{13}C NMR (125 MHz, $CDCl_3$) δ 190.36, 152.89, 131.03, 113.98, 71.93, 70.99, 70.71, 70.59, 69.42, 69.04, 59.02; HRMS (EI, m/z): $[M+H]^+$ calculated for $C_{22}H_{34}O_{10}$: 459.2224, found: 459.2210.

Tetrahydroxy-naphthopleiadene (TEGNP) (12)

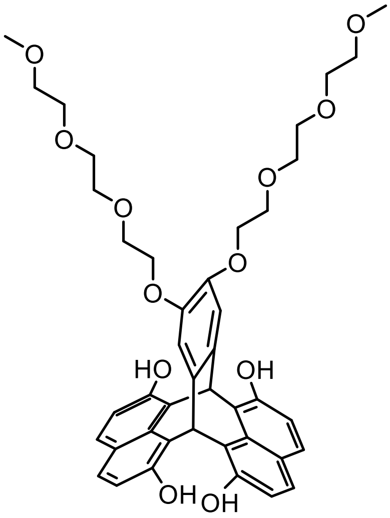

A solution of aldehyde **(11)** (5 g, 10.91 mmol), 2,7-dihydroxynaphthalene (4.37 g, 27.28 mmol) and methanesulfonic acid (2 ml) in DCM (100 ml) was stirred at room temperature for 24 h. The reaction mixture was quenched with water, extracted with DCM, dried over anhydrous

Na_2SO_4, and the solvent was removed under reduced pressure. The residue was purified by silica gel column chromatography DCM/MeOH (95:5 v/v) to yield the product **(12)** as orange solid (3,15 g, 4.24 mmol, 39%). Mp: 80 °C; FTIR (*v*, cm^{-1}): 3315, 2927, 2873, 1626, 1518, 1445, 1262, 1220, 1076; ^1H NMR (500 MHz, DMSO-d_6) δ 9.93 (s, 4H, OH), 7.45 (d, *J* = 8.7 Hz, 4H, ArH), 7.00 (s, 2H, ArH), 6.93 (d, *J* = 8.7 Hz, 4H, ArH), 6.64 (s, 2H, CH), 4.06 (t, *J* = 3.8 Hz, 4H, CH_2), 3.68 (t, *J* = 3.8 Hz, 4H, CH_2), 3.56 (m, 4H, CH_2), 3.48 (m, 8H, CH_2), 3.38 (m, 4H, CH_2), 3.20 (s, 6H, OCH_3); ^{13}C NMR (125 MHz, DMSO-d_6) δ 151.78, 147.68, 134.88, 133.84, 128.99, 125.35, 120.70, 115.60, 71.71, 70.38, 70.27, 70.03, 69.60, 69.22, 58.46, 38.79; HRMS (EI, m/z): $[M+H]^+$ calculated for $C_{42}H_{47}O_{12}$: 743.3062, found: 743.3077.

***trans*-Acenaphthene-1,2-diol (13)**[124]

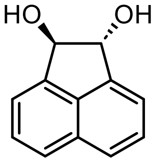

To a stirred suspension of acenaphthylene-1,2-dione (10 g, 54.89 mmol) in methanol (150 ml) at 0 °C, was added sodium borohydride (4.15 g, 109.78 mmol) in small portions. The reaction mixture was allowed to stir at room temperature for 1.5 h. The solvent was evaporated under reduced pressure, and the resulting residue was washed with water to yield the diol **(13)** (6.13 g, 32.93 mmol, 60%). ^1H NMR (500 MHz, DMSO-d_6) δ 7.76 (d, 2H, Ar-H), 7.57 (m, 2H, Ar-H), 7.45 (d, 2H, Ar-H), 5.88 (d, 2H, CH), 5.20 (d, 2H, OH); ^{13}C NMR (125 MHz, DMSO-d_6) δ 144.20, 135.82, 130.73, 128.69, 124.32, 120.42, 82.88.

1,8-Naphthalene dialdehyde hydrate (14)

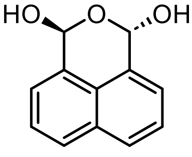

The compound 1.8-naphthalene dialdehyde hydrate **(14)** was synthesised according to the procedure reported by Criegee *et al.*[125] A mixture of *trans*-diol **(13)** (5g, 26.85 mmol), lead tetraacetate (13.10 g, 29.54 mmol) and toluene (135 ml) was stirred vigorously for 15 min at room temperature under N_2 atmosphere. The resulting precipitate was removed by filtration, 150 ml of 2M HCl solution was added to the filter and stirring vigorously for 5 min. The resulting precipitate was collected by filtration and washed with water to yield the hydrate **(14)** as white solid (2.44 g, 12.08 mmol, 45%). Mp: 130 °C; FTIR (v, cm^{-1}): 3306, 2866, 1318, 1007; ^1H NMR (500 MHz, DMSO-d_6) δ 7.87 (d, J = 7.1 Hz, 2H, Ar-H), 7.52 (m, 4H, Ar-H), 7.26 (d, J = 7.3 Hz, 2H, OH), 6.25 (d, J = 7.3 Hz, 2H, CH); ^{13}C NMR (125 MHz, DMSO-d_6) δ 136.14, 132.52, 127.57, 127.37, 126.17, 121.45. HRMS (ESI, m/z): $[M+Na]^+$ calculated for $C_{12}H_{10}O_3Na_1$: 225.05222, found: 225.0523.

Benzopleiadene (BP) (15)

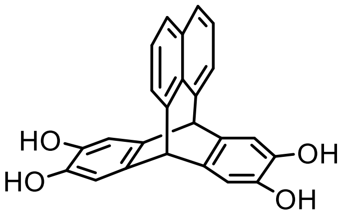

A solution of 1,8-naphthalene dialdehyde hydrate **(14)** (500 mg, 2.47 mmol), catechol (1.36 g, 12.35 mmol) and conc. H_2SO_4 (2 ml) in acetic acid (15 ml) was heated at reflux for 4 h. After cooling to room temperature, the reaction mixture was poured into ice water, neutralized with saturated $NaHCO_3$, and extracted with ethyl acetate. The combined organic layers were collected, dried over anhydrous Na_2SO_4, and the solvent was removed under reduced pressure. The crude product was purified by silica gel column chromatography DCM/MeOH (97:3 v/v) to afford the product **(15)** as white solid (318 mg, 0.86 mmol, 35%). Mp: >300 °C; FTIR (v, cm^{-1}): 3452, 3320, 3047, 2920, 1667, 1610, 1502, 1460, 1060; ^1H NMR (500 MHz, DMSO-d_6) δ 8.63 (s, 4H, OH), 7.60 (d, J = 8.2 Hz, 2H, ArH), 7.48 (d, J = 7.1 Hz, 2H, ArH), 7.28 (t, J = 7.6 Hz, 2H, ArH), 6.84 (s, 4H, ArH), 4.93 (s, 2H, CH); ^{13}C NMR (125 MHz, DMSO-d_6) δ

143.28, 139.57, 135.75, 133.87, 127.81, 127.66, 125.92, 123.44, 113.64, 54.64; HRMS (EI, m/z): $[M]^+$ calculated for $C_{24}H_{16}O_4$: 368.1043, found: 368.1045.

X-ray Crystallography: $C_{25.5}H_{19}O_{4.5}$, M_r = 397.41, monoclinic, *C2/c* (No. 15), a = 20.9694(11) Å, b = 9.0766(5) Å, c = 21.5098(11) Å, β = 117.382(3)°, $\alpha = \gamma$ = 90°, V = 3635.3(3) Å^3, T = 100.0 K, Z = 8, Z' = 1, μ(Mo K_α) = 0.099, 70956 reflections measured, 3337 unique (R_{int} = 0.0855) which were used in all calculations. The final wR_2 was 0.1768 (all data) and R_1 was 0.0593 (I≥2 σ(I)).

7,14-epoxy-7*H*,14*H*-cycloocta[1,2,3-*de*:5,6,7-*d'e'*]dinaphthalene (EDN) (16)

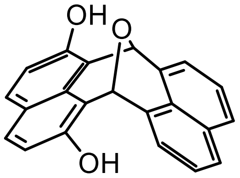

A solution of 1,8-naphthalene dialdehyde hydrate **(14)** (500 mg, 2.47 mmol), 2,7-dihydroxynaphthalene (475 mg, 2.96 mmol) and conc. HCl (1.25 ml) in acetic acid (10 ml) was heated at reflux for 6 h. After cooling to room temperature, the reaction mixture was quenched with water. The resulting precipitate was filtered, washed with water to afford **(16)** as light purple solid (750 mg, 2.30 mmol, 93%). Mp: >300 °C; FTIR (ν, cm^{-1}): 3300, 3047, 2939, 1638, 1592, 1510, 1266; ^{1}H NMR (500 MHz, DMSO-d$_6$) δ 10.02 (s, 2H, OH), 7.75 (m, 4H, ArH), 7.47 (m, 4H, ArH), 6.91 (d, J = 8.8 Hz, 2H, ArH), 6.56 (s, 2H, CH); ^{13}C NMR (125 MHz, DMSO-d$_6$) δ 149.65, 136.12, 133.00, 127.79, 127.08, 126.41, 126.16, 124.83, 122.08, 120.64, 115.34, 69.00; HRMS (EI, m/z): $[M+H]^+$ calculated for $C_{22}H_{15}O_3$: 327.1015, found: 327.1002.

X-ray Crystallography: $C_{22}H_{14}O_3$, M_r = 326.354, triclinic, *P*-1 (No. 2), a = 9.1543(3) Å, b = 11.9041(3) Å, c = 14.0829(4) Å, α = 74.820(2)°, β = 88.826(2)°, γ = 87.668(4)°, V = 1479.82(7) Å^3, T = 100.00(10) K, Z = 4, Z' = 2, μ(Cu K_α) = 0.785, 30743 reflections measured, 6133 unique (R_{int} = 0.0323) which were used in all calculations. The final wR_2 was 0.1151 (all data) and R_1 was 0.0402 (I≥2 σ(I)).

1,8-Dibenzoyl-2,7-dimethoxynaphthalene (17)

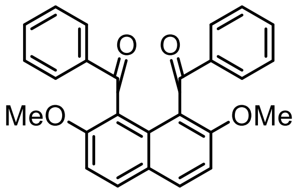

The compound 1,8-dibenzoyl-2,7-dimethoxynaphthalene was synthesised according to the procedure reported by Okamoto *et al.*[153] A mixture of 2,7-dimethoxynaphthalene (3,01 g, 16 mmol), benzoic acid (4.3 g, 35.2 mmol) and P_2O_5-MsOH (72 ml) was stirred at 60 °C for 3 h. The reaction mixture was poured into ice water (200 ml), and the resulting mixture was extracted with chloroform (150 ml x 3). The combined extracts were washed with 2M NaOH aqueous solution (300 ml x 2), brine (300 ml x 1). The organic layer was dried over anhydrous Na_2SO_4, and the solvent was removed under reduced pressure. The resulting crude product was washed with a small amount of methanol to yield **(17)** as white solid (4.12 g, 10.40 mmol, 65%). FTIR (v, cm^{-1}): 3051, 3010, 2945, 2850, 1662, 1600, 1510, 1452, 1255; ^{1}H NMR (500 MHz, $CDCl_3$) δ 7.99 (d, J = 9.3 Hz, 2H, ArH), 7.73 (d, J = 6.9 Hz, 4H, ArH), 7.51 (t, J = 7.4 Hz, 2H, ArH), 7.37 (t, J = 7.9 Hz, 4H, ArH), 7.24 (d, J = 9.3 Hz, 2H, ArH), 3.71 (s, 6H, OCH_3); ^{13}C NMR (125 MHz, $CDCl_3$) δ 196.88, 156.33, 138.67, 132.67, 132.05, 129.90, 129.13, 127.99, 125.61, 121.58, 111.31, 56.45.

1,8-Bis(hydroxymethyl)phenyl-2,7-dimethoxynaphthalene (18)

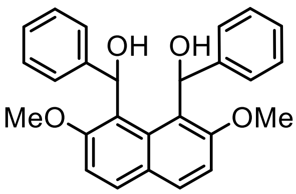

To a solution of 1,8-dibenzoyl-2,7-dimethoxynaphthalene **(17)** (2 g, 5.04 mmol) in dry THF

(80 ml) was added $LiAlH_4$ (2 g, 52.7 mmol) in small portions at 0 °C. The reaction mixture was allowed to warm up to room temperature and stirred for 15 h under N_2 atmosphere. The reaction mixture was carefully quenched with water in an ice bath and acidified with 1M HCl solution. The resulting mixture was extracted with DCM, the organic layer was dried over anhydrous Na_2SO_4, and the solvent was removed under reduced pressure. The residue was washed with a small amount of diethyl ether to afford **(18)** as white solid (1.45 g, 3.62 mmol, 72%). Mp: 188 °C; FTIR (ν, cm^{-1}): 3453, 3340, 3054, 2930, 2831, 1607, 1519, 1267, 1037; ^1H NMR (500 MHz, DMSO-d_6, 353K) δ 7.86 (d, J = 9.0 Hz, 2H, ArH), 7.23 (d, J = 9.0 Hz, 2H, ArH), 7.13 (m, 4H, ArH), 7.04 (m, 6H, ArH), 6.45 (d, J = 7.9 Hz, 2H, CH_2), 5.39 (br, 2H, OH), 3.49 (s, 6H, OCH_3); ^{13}C NMR (125 MHz, DMSO-d_6) δ 158.63, 146.66, 131.14, 127.57, 126.16, 125.81, 125.51, 113.05, 71.15, 56.63; HRMS (EI, m/z): $[M+Na]^+$ calculated for $C_{26}H_{24}O_4Na_1$: 423.1566, found: 423.1563.

Dimethoxy-functionalised benzopleiadene (DMBP) (19)

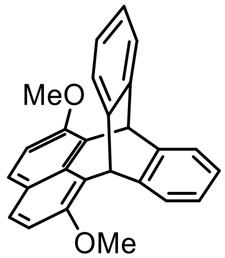

To a solution of **(18)** (2 g, 5 mmol) in dry DCM (100 ml) and hexafluoro-2-propanol (25 ml) was added anhydrous $AlCl_3$ (6.67 g, 50 mmol) under N_2 atmosphere, and stirred at room temperature for 10 min. The reaction mixture was quenched carefully with water in an ice bath and extracted with DCM. The combined organic layers were dried over anhydrous Na_2SO_4, and the solvent was removed under reduced pressure. The crude product was purified by silica gel column chromatography DCM/hexane (1:4 v/v) to yield the product **(19)** as white solid (0.91 g, 2.5 mmol, 50%). Mp: 287 °C; FTIR (ν, cm^{-1}): 3066, 3020, 2932, 2835, 1610, 1510, 1453, 1256; ^1H NMR (500 MHz, $CDCl_3$) δ 7.51 (d, J = 9.1 Hz, 2H, ArH), 7.46 (dd, J = 5.5, 3.3

Hz, 4H, ArH), 7.13 (dd, $J = 5.5, 3.3$ Hz, 4H, ArH), 7.10 (d, $J = 9.1$ Hz, 2H, ArH), 6.16 (s, 2H, CH), 4.08 (s, 6H, OCH_3); ^{13}C NMR (125 MHz, $CDCl_3$) δ 152.51, 142.41, 129.66, 128.76, 126.70, 126.33, 125.60, 121.72, 112.26, 57.53, 44.46; HRMS (EI, m/z): $[M+H]^+$ calculated for $C_{26}H_{21}O_2$: 365.1536, found: 365.1537.

X-ray Crystallography: $C_{26}H_{20}O_2$, $M_r = 364.447$, triclinic, P-1 (No. 2), a = 9.17048(17) Å, b = 10.3087(2) Å, c = 10.4552(2) Å, $\alpha = 76.6367(19)°$, $\beta = 69.8889(19)°$, $\gamma = 85.5235(17)°$, $V = 902.99(4)$ Å^3, $T = 100.01(10)$ K, $Z = 2$, $Z' = 1$, μ (Cu K_α) = 0.655, 7130 reflections measured, 7130 unique which were used in all calculations. The final wR_2 was 0.0515 (all data) and R_1 was 0.0194 ($I \geq 2\sigma(I)$).

Dihydroxyl-functionalised benzopleiadene (DHBP) (20)

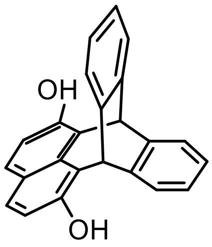

To a solution of **(19)** (1 g, 2.74 mmol) in anhydrous DCM (30 ml) under N_2 atmosphere, cooled to 0 °C, BBr_3 (1.03 g, 4.11 mmol) was added dropwise. The reaction mixture was allowed to warm up to room temperature and stirring for 3 h. The reaction mixture was poured into ice water and extracted with DCM. The combined organic layers were dried over anhydrous Na_2SO_4, and the solvent was removed under reduced pressure to yield the product **(20)** as white solid (0.78 g, 2.33 mmol, 85%). Mp: >300 °C; FTIR (v, cm^{-1}): 3562, 3400, 3335, 3070, 3015, 1620, 1510, 1286, 1262; ^1H NMR (500 MHz, DMSO-d_6) δ 9.76 (s, 2H, OH), 7.38 (m, 6H ArH), 7.11 (dd, $J = 5.5, 3.3$ Hz, 4H, ArH), 6.89 (d, $J = 8.7$ Hz, 2H, ArH), 5.97 (s, 2H, CH); ^{13}C NMR (125 MHz, DMSO-d_6) δ 150.52, 142.60, 130.35, 128.65, 126.64, 125.62, 124.58, 117.06, 115.12, 44.15; HRMS (EI, m/z): $[M+H]^+$ calculated for $C_{24}H_{17}O_2$: 337.1223, found: 337.1214.

8.3 Synthesis of Polymers

General procedure for polybenzodioxin polymers (GP-1)

The polybenzodioxin polymers were synthesised according to the literature procedure.[154] The appropriate biscatechol (1.00 eq.) and tetrafluoroterepthalonitrile (1.00 eq.) were dissolved in anhydrous DMF. Anhydrous potassium carbonate (8.00 eq.) was then added into the solution and the mixture was heated at 65 °C for 72 h. The reaction mixture was then poured into water, the precipitate was filtered, washed repeatedly with water, acetone and methanol. The obtained polymer was refluxed in acetone and methanol overnight, then filtered, and dried under vacuum at 100 °C for 24 h.

PIM-1

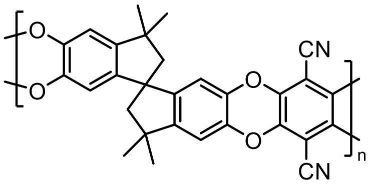

General procedure **GP-1** was followed using TTSBI (5 g, 14.69 mmol), TFTPN (2.93 g, 14.69 mmol), anhydrous potassium carbonate (16.24 g, 117.52 mmol) and anhydrous DMF (100 ml) were combined to afford **PIM-1** as yellow powder (6.62 g, 98%). FTIR (v, cm^{-1}): 2951, 2240, 1445, 1265; BET surface area = 709 m^2/g; total pore volume = 0.55 cm^3/g ($P/P_o = 0.98$); CO_2 uptake = 49 cm^3/g ($P/P_o = 0.99$); TGA: 500 °C (onset decomposition temperature).

PIM-DMNP$_{10}$

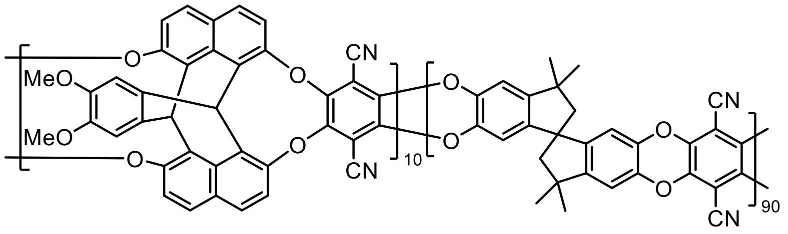

General procedure **GP-1** was followed using **DMNP (6)** monomer (0.2 g, 0.42 mmol), TTSBI (1.29g, 3.78 mmol), TFTPN (0.84 g, 4.2 mmol), anhydrous potassium carbonate (4.64 g, 33.6 mmol) and anhydrous DMF (30 ml) were combined to afford **PIM-DMNP$_{10}$** as yellow powder (1.96 g, 98%). FTIR (v, cm^{-1}): 2960, 2241, 1448, 1266, 1208, 1100, 1010, 878; BET surface area = 666 m^2/g; total pore volume = 0.47 cm^3/g (P/P_o = 0.98); CO$_2$ uptake = 47 cm^3/g (P/P_o = 0.99); TGA: 488 ℃ (onset decomposition temperature).

PIM-DMNP$_{25}$

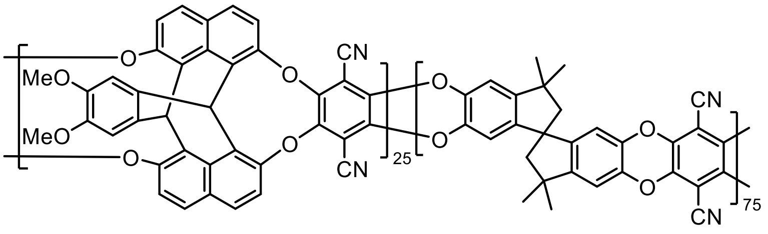

General procedure **GP-1** was followed using **DMNP (6)** monomer (0.4 g, 0.84 mmol), TTSBI (0.86 g, 2.52 mmol), TFTPN (0.67 g, 3.36 mmol), anhydrous potassium carbonate (3.72 g, 26.88 mmol) and anhydrous DMF (25 ml) were combined to afford **PIM-DMNP$_{25}$** as yellow powder (1.60 g, 96%). FTIR (v, cm^{-1}): 2956, 2241, 1609, 1518, 1448, 1262, 1200,1109, 1084, 1005, 878; BET surface area = 699 m^2/g; total pore volume = 0.59 cm^3/g (P/P_o = 0.98); CO$_2$ uptake = 51 cm^3/g (P/P_o = 0.99); TGA: 476 ℃ (onset decomposition temperature).

PIM-DMNP$_{50}$

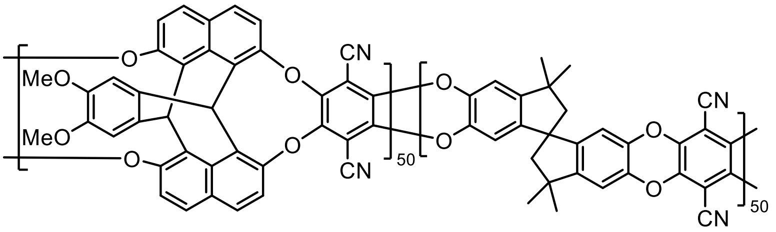

General procedure **GP-1** was followed using **DMNP (6)** monomer (0.6 g, 1.25 mmol), TTSBI (0.42 g, 1.25 mmol), TFTPN (0.50 g, 2.5 mmol), anhydrous potassium carbonate (2.76 g, 20 mmol) and anhydrous DMF (20 ml) were combined to afford **PIM-DMNP$_{50}$** as yellow powder (1.28 g, 97%). FTIR (v, cm^{-1}): 2956,2241, 1613, 1514, 1436, 1262, 1200, 1084, 1005, 873, 836; BET surface area = 683 m^2/g; total pore volume = 0.56 cm^3/g (P/P_o = 0.98); CO_2 uptake = 50 cm^3/g (P/P_o = 0.99); TGA: 461 °C (onset decomposition temperature).

PIM-BNP$_{10}$

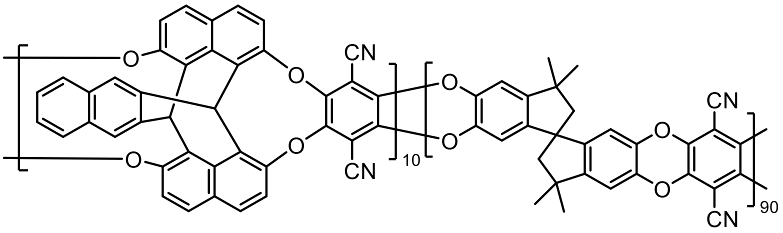

General procedure **GP-1** was followed using **BNP (2)** monomer (0.2 g, 0.43 mmol), TTSBI (1.32 g, 3.87 mmol), TFTPN (0.86 g, 4.3 mmol), anhydrous potassium carbonate (4.75 g, 34.4 mmol) and anhydrous DMF (30 ml) were combined to afford **PIM-BNP$_{10}$** as yellow powder (1.93 g, 95%). FTIR (v, cm^{-1}): 2960, 2860, 2241, 1445, 1266, 1010, 878; BET surface area = 728 m^2/g; total pore volume = 0.52 cm^3/g (P/P_o = 0.98); CO_2 uptake = 46 cm^3/g (P/P_o = 0.99); TGA: 506 °C (onset decomposition temperature).

PIM-BNP$_{25}$

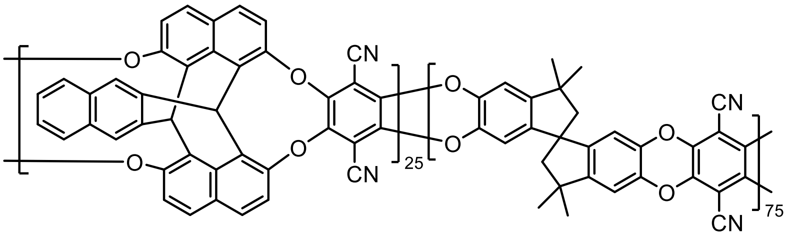

General procedure **GP-1** was followed using **BNP (2)** monomer (0.4 g, 0.85 mmol), TTSBI (0.87 g, 2.55 mmol), TFTPN (0.68 g, 3.4 mmol), anhydrous potassium carbonate (3.76 g, 27.2 mmol) and anhydrous DMF (27 ml) were combined to afford **PIM-BNP$_{25}$** as yellow powder (1.62 g, 97%). FTIR (*v*, cm^{-1}): 2960, 2860, 2241, 1445, 1266, 1005, 878, 840; BET surface area = 740 m^{2}/g; total pore volume = 0.54 cm^{3}/g (P/P_o = 0.98); CO$_2$ uptake = 57 cm^{3}/g (P/P_o = 0.99); TGA: 501 °C (onset decomposition temperature).

PIM-BNP$_{50}$

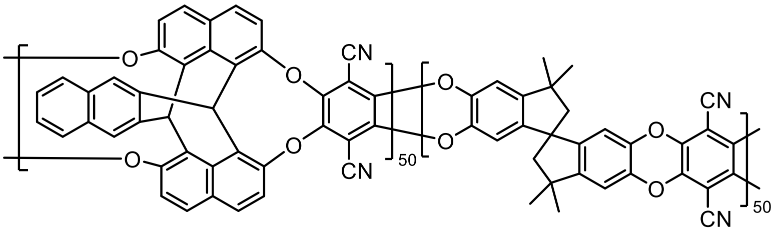

General procedure **GP-1** was followed using **BNP (2)** monomer (0.6 g, 1.28 mmol), TTSBI (0.44 g, 1.28 mmol), TFTPN (0.51 g, 2.56 mmol), anhydrous potassium carbonate (2.83 g, 20.48 mmol) and anhydrous DMF (22 ml) were combined to afford **PIM-BNP$_{50}$** as yellow powder (1.30 g, 97%). FTIR (*v*, cm^{-1}): 2960, 2860, 2241, 1431, 1290, 1005, 878, 840; BET surface area = 732 m^{2}/g; total pore volume = 0.47 cm^{3}/g (P/P_o = 0.98); CO$_2$ uptake = 53 cm^{3}/g (P/P_o = 0.99); TGA: 473 °C (onset decomposition temperature).

PIM-TEGNP$_{10}$

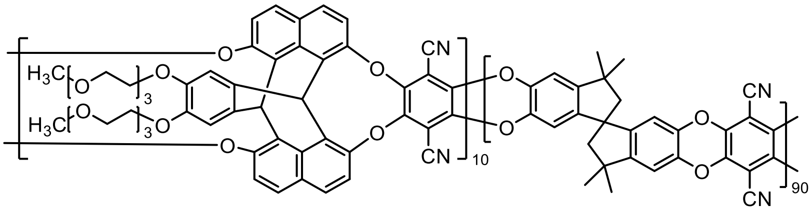

General procedure **GP-1** was followed using **TEGNP (12)** monomer (0.24 g, 0.32 mmol), TTSBI (0.99 g, 2.91 mmol), TFTPN (0.64 g, 3.2 mmol), anhydrous potassium carbonate (3.53 g, 25.6 mmol) and anhydrous DMF (21 ml) were combined to afford **PIM-TEGNP$_{10}$** as yellow powder (1.45 g, 90%). FTIR (v, cm^{-1}): 2960, 2871, 1617, 1450, 1262, 1011; BET surface area = 559 m^2/g; total pore volume = 0.34 cm^3/g (P/P_o = 0.98); CO$_2$ uptake = 46 cm^3/g (P/P_o = 0.99); TGA: 455 °C (onset decomposition temperature).

PIM-TEGNP

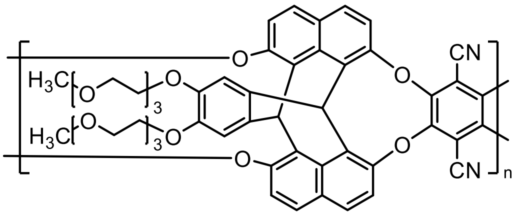

General procedure **GP-1** was followed using **TEGNP (12)** monomer (0.6 g, 0.81 mmol), TFTPN (0.162 g, 0.81 mmol), anhydrous potassium carbonate (0.90 g, 6.48 mmol) and anhydrous DMF (12 ml) were combined to afford **PIM-TEGNP** as yellow powder (0.64 g, 92%). FTIR (v, cm^{-1}): 2870, 2237, 1618, 1510, 1423, 1192, 1084, 1002; BET surface area = 0.175 m^2/g; total pore volume = 0.005 cm^3/g (P/P_o = 0.98); CO$_2$ uptake = 7.7 cm^3/g (P/P_o = 0.99); TGA: 359 °C (onset decomposition temperature).

PIM-BP

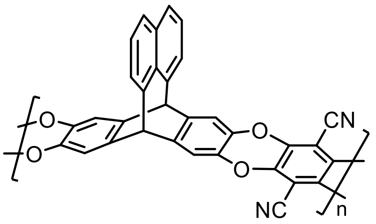

General procedure **GP-1** was followed using **BP (15)** monomer (0.8 g, 2.17 mmol), TFTPN (0.435 g, 2.17 mmol), anhydrous potassium carbonate (2.40 g, 17.36 mmol) and anhydrous DMF (15 ml) were combined to afford **PIM-BP** as yellow powder (1 g, 94%). FTIR (*v*, cm^{-1}):2241, 1448, 1290, 1262, 1230, 1146, 1005; BET surface area = 800 m^2/g; total pore volume = 0.53 cm^3/g (P/P_o = 0.98); CO_2 uptake = 68 cm^3/g (P/P_o = 0.99); TGA: 558 °C (onset decomposition temperature).

PIM-BP$_{25}$

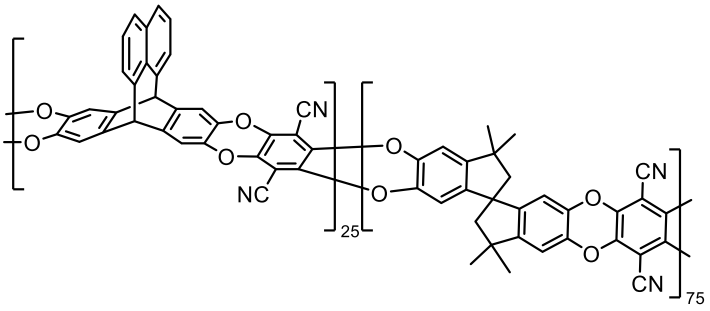

General procedure **GP-1** was followed using **BP (15)** monomer (0.20 g, 0.54 mmol), TTSBI (0.55 g, 1.62 mmol), TFTPN (0.43 g, 2.16 mmol), anhydrous potassium carbonate (2.39 g, 17.28 mmol) and anhydrous DMF (15 ml) were combined to afford **PIM-BP$_{25}$** as yellow powder (0.77 g, 76%). FTIR (*v*, cm^{-1}): 2956, 2241, 1448, 1287, 1262, 1100, 1010; BET surface area = 788 m^2/g; total pore volume = 0.54 cm^3/g (P/P_o = 0.98); CO_2 uptake = 59 cm^3/g (P/P_o = 0.99); TGA: 491 °C (onset decomposition temperature).

PIM-BP$_{50}$

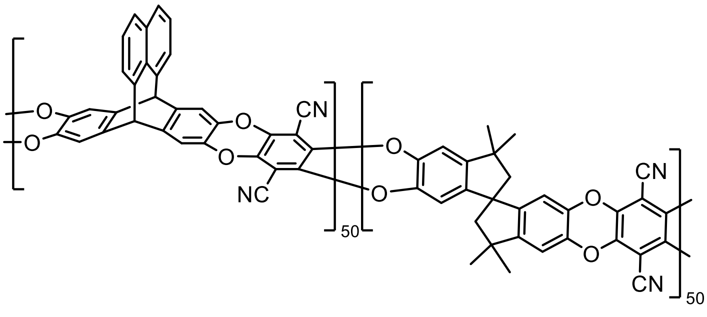

General procedure **GP-1** was followed using **BP (15)** monomer (0.4 g, 1.09 mmol), TTSBI (0.37 g, 1.09 mmol), TFTPN (0.44 g, 2.18 mmol), anhydrous potassium carbonate (2.41 g, 17.44 mmol) and anhydrous DMF (15 ml) were combined to afford **PIM-BP$_{50}$** as yellow powder (0.90g, 87%). FTIR (ν, cm^{-1}): 2241, 1448, 1287, 1262, 1225, 1146, 1005; BET surface area = 830 m^2/g; total pore volume = 0.53 cm^3/g (P/P_o = 0.98); CO$_2$ uptake = 65 cm^3/g (P/P_o = 0.99); TGA: 513 °C (onset decomposition temperature).

PIM-BP$_{75}$

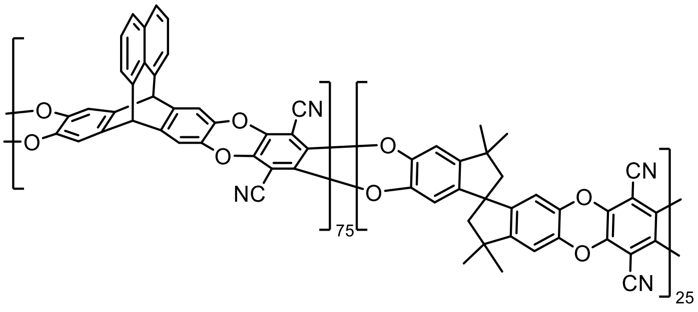

General procedure **GP-1** was followed using **BP (15)** monomer (0.6 g, 1.63 mmol), TTSBI (0.18 g, 0.54 mmol), TFTPN (0.43 g, 2.17 mmol), anhydrous potassium carbonate (2.40 g, 17.36 mmol) and anhydrous DMF (15 ml) were combined to afford **PIM-BP$_{75}$** as yellow powder (0.92 g, 89%). FTIR (ν, cm^{-1}): 2241, 1445, 1287, 1262, 1225, 1230, 1145, 1100, 1005; BET surface area = 813 m^2/g; total pore volume = 0.55 cm^3/g (P/P_o = 0.98); CO$_2$ uptake = 61 cm^3/g (P/P_o = 0.99); TGA: 502 °C (onset decomposition temperature).

AO-PIM-BP

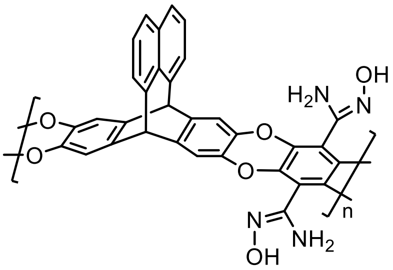

PIM-BP (0.5 g, 1.02 mmol) was dispersed in NMP (50 mL), followed by the addition of hydroxylamine (10 mL), and the mixture was reacted at 70 °C for 24 h. After cooling, the reaction mixture was poured into ethanol, and the resulting precipitate was collected by filtration and washed thoroughly with ethanol. **AO-PIM-BP** was obtained as a light brown powder (0.52 g, 92%); TGA: 238 °C (onset decomposition temperature).

PEEK-EDN

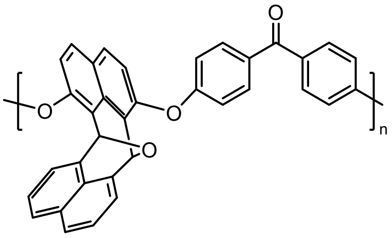

The **PEEK-EDN** polymer was synthesised following the literature work.[135, 155] **EDN** monomer (2 g, 6.13 mmol) and 4,4′-difluorobenzophenone (1.34 g, 6.13 mmol) were dissolved in anhydrous N,N-Dimethylacetamide (DMAc) (20 mL) and anhydrous toluene (5 mL) in a round bottom flask equipped with a Dean-stark apparatus under nitrogen atmosphere. Potassium carbonate (2,12 g, 15.33 mmol) was added, and the reaction was heated to 140°C to remove the generated water. After removal, the reaction was heated to reflux (165 °C) for 12 h. The reaction was precipitated in hot water and filtered. The resulting polymer was washed thoroughly with hot water followed by methanol. It was then purified by dissolution in DMAc and reprecipitation from methanol twice, yielding **PEEK-EDN** as a light brown fibrous solid after drying in a vacuum oven at 100 °C overnight. FTIR (ν, $\mathrm{cm^{-1}}$): 1655, 1591, 1496, 1225.

PES-EDN

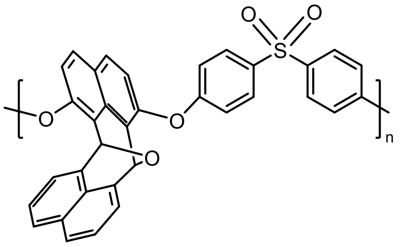

The **PES-EDN** polymer was synthesized using the same procedure as **PEEK-EDN**. **EDN** monomer (2 g, 6.13 mmol), 4,4′-Difluorodiphenyl sulfone (1.56 g, 6.13 mmol), potassium carbonate (2,12 g, 15.33 mmol), dimethylacetamide (DMAc) (20 mL) and anhydrous toluene (5 mL) were combined to afford **PES-EDN** as a light brown fibrous solid after drying in a vacuum oven at 100 °C overnight. FTIR (v, cm^{-1}): 1628, 1584, 1485, 1230, 1150, 1105; BET surface area = 40 m^2/g; total pore volume = 0.16 cm^3/g (P/P_o = 0.98); CO_2 uptake = 20 cm^3/g (P/P_o = 0.99).

PEN-DHBP

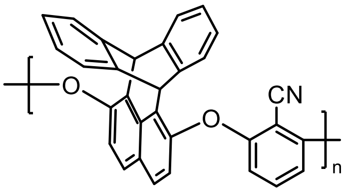

To a solution of **DHBP** (0.5 g, 1.49 mmol) and **DFBN** (0.21g, 1.49 mmol) in dry NMP (10 ml) was added anhydrous K_2CO_3 (0.62g, 4.47 mmol) under nitrogen atmosphere. Then the reaction mixture was stirred at 170 °C for 24 h. After cooling to room temperature, the mixture was quenched with water, filtered, washed with water, methanol. The crude product was refluxed in methanol to afford the desired **PEN-DHBP** polymer as an off-white powder (0.52 g, 80%). FTIR (v, cm^{-1}): 3335, 3021, 2230, 1030; BET surface area = 86 m^2/g; total pore volume = 0.22 cm^3/g (P/P_o = 0.98); CO_2 uptake = 22 cm^3/g (P/P_o = 0.99).

References

1 J. Rouquerol, D. Avnir, C. W. Fairbridge, D. H. Everett, J. Haynes, N. Pernicone, J. D. Ramsay, K. S. W. Sing, K. K. Unger, *Pure and Applied Chemistry* 1994, **66**, 1739-1758.

2 M. Thommes, K. Kaneko, A. V. Neimark, J. P. Olivier, F. Rodriguez-Reinoso, J. Rouquerol, K. S. Sing, *Pure and Applied Chemistry* 2015, **87**, 1051-1069.

3 F. Topuz, M. H. Abdellah, P. M. Budd, M. A. Abdulhamid, *Polymer Reviews* 2024, **64**, 251-305.

4 Y.-L. Zhao, X. Zhang, M.-Z. Li, J.-R. Li, *Chemical Society Reviews* 2024, **53**, 2056-2098.

5 Q. Qian, P. A. Asinger, M. J. Lee, G. Han, K. Mizrahi Rodriguez, S. Lin, F. M. Benedetti, A. X. Wu, W. S. Chi, Z. P. Smith, *Chemical Reviews* 2020, **120**, 8161-8266.

6 P. Klobes, R. G. Munro, Porosity and Specific Surface Area Measurements for Solid Materials, *National Institute of Standards and Technology (NIST)*, Gaithersburg MD, 2006.

7 L. M. Anovitz, D. R. Cole, *Reviews in Mineralogy and Geochemistry* 2015, **80**, 61-164.

8 S. Brunauer, P. H. Emmett, E. Teller, *Journal of the American Chemical Society* 1938, **60**, 309-319.

9 I. Langmuir, *Journal of the American Chemical Society* 1916, **38**, 2221-2295.

10 K. Sing, D. Everett, R. Haul, L. Moscou, R. Pierotti, J. Rouquerol, T. Siemieniewska, *Pure and Applied Chemistry* 1985, **57**, 603-619.

11 Z. Chen, K. O. Kirlikovali, K. B. Idrees, M. C. Wasson, O. K. Farha, *Chem* 2022, **8**, 693-716.

12 P. Del Campo, C. Martínez, A. Corma, *Chemical Society Reviews* 2021, **50**, 8511-8595.

13 E. Jin, S. Lee, E. Kang, Y. Kim, W. Choe, *Coordination Chemistry Reviews* 2020, **425**, 213526.

14 A. R. Kamble, C. M. Patel, Z. Murthy, *Renewable and Sustainable Energy Reviews* 2021, **145**, 111062.

15 R. S. K. Valappil, N. Ghasem, M. Al-Marzouqi, *Journal of Industrial and Engineering Chemistry* 2021, **98**, 103-129.

16 N. Stock, S. Biswas, *Chemical Reviews* 2012, **112**, 933-969.

17 S.-Y. Ding, W. Wang, *Chemical Society Reviews* 2013, **42**, 548-568.

18 N. B. McKeown, P. M. Budd, *Chemical Society Reviews* 2006, **35**, 675-683.

19 S. Sircar, T. Golden, M. Rao, *Carbon* 1996, **34**, 1-12.

20 J. i. Hayashi, A. Kazehaya, K. Muroyama, A. P. Watkinson, *Carbon* 2000, **38**, 1873-1878.

21 P. Girods, A. Dufour, V. Fierro, Y. Rogaume, C. Rogaume, A. Zoulalian, A. Celzard, *Journal of Hazardous Materials* 2009, **166**, 491-501.

22 W. M. A. W. Daud, W. S. W. Ali, M. Z. Sulaiman, *Carbon* 2000, **38**, 1925-1932.

23 C. Rodríguez Correa, M. Stollovsky, T. Hehr, Y. Rauscher, B. Rolli, A. Kruse, *ACS Sustainable Chemistry & Engineering* 2017, **5**, 8222-8233.

24 F. Sardella, M. Gimenez, C. Navas, C. Morandi, C. Deiana, K. Sapag, *Journal of Environmental Chemical Engineering* 2015, **3**, 253-260.

25 J. Pallarés, A. González-Cencerrado, I. Arauzo, *Biomass and Bioenergy* 2018, **115**, 64-73.

26 S. Lv, C. Li, J. Mi, H. Meng, *Applied Surface Science* 2020, **510**, 145425.

27 Z. Heidarinejad, M. H. Dehghani, M. Heidari, G. Javedan, I. Ali, M. Sillanpää, *Environmental Chemistry Letters* 2020, **18**, 393-415.

28 P. T. Moseley, D. A. Rand, A. Davidson, B. Monahov, *Journal of Energy Storage* 2018, **19**, 272-290.

29 W. Gu, G. Yushin, *WIREs Energy and Environment* 2014, **3**, 424-473.

30 M. Danish, T. Ahmad, *Renewable and Sustainable Energy Reviews* 2018, **87**, 1-21.

31 N. Z. M. Azmi, A. Buthiyappan, A. A. A. Raman, M. F. A. Patah, S. Sufian, *Journal of Industrial and Engineering Chemistry* 2022, **116**, 1-20.

32 A. Bhatnagar, W. Hogland, M. Marques, M. Sillanpää, *Chemical Engineering Journal* 2013, **219**, 499-511.

33 M. Mariana, A. K. Hps, E. Mistar, E. B. Yahya, T. Alfatah, M. Danish, M. Amayreh, *Journal of Water Process Engineering* 2021, **43**, 102221.

34 N. Masoumifard, R. Guillet-Nicolas, F. Kleitz, *Advanced Materials* 2018, **30**, 1704439.

35 A. F. Cronstedt, *Svenska Vetenskaps akademiens Handlingar* 1756, **17**, 120-123.

36 C. Colella, A. F. Gualtieri, *Microporous and Mesoporous Materials* 2007, **105**, 213-221.

37 E. Kapaca, J. Jiang, J. Cho, J. L. Jordá, M. J. Diaz-Cabanas, X. Zou, A. Corma, T. Willhammar, *Journal of the American Chemical Society* 2021, **143**, 8713-8719.

38 T. Nakano, Y. Nozue, *Journal of Computational Methods in Sciences and Engineering* 2007, **7**, 443-462.

39 Q. Zhang, S. Gao, J. Yu, *Chemical Reviews* 2022, **123**, 6039-6106.

40 G. N. Vayssilov, N. Rösch, *The Journal of Physical Chemistry B* 2001, **105**, 4277-4284.

41 S. Van Donk, A. H. Janssen, J. H. Bitter, K. P. de Jong, *Catalysis Reviews* 2003, **45**, 297-319.

42 E. Pérez-Botella, S. Valencia, F. Rey, *Chemical Reviews* 2022, **122**, 17647-17695.

43 B. Smit, T. L. Maesen, *Chemical Reviews* 2008, **108**, 4125-4184.

44 Y. Li, J. Yu, *Nature Reviews Materials* 2021, **6**, 1156-1174.

45 J. Huang, S. R. Turner, *Polymer Reviews* 2018, **58**, 1-41.

46 M. P. Tsyurupa, V. A. Davankov, *Reactive and Functional Polymers* 2006, **66**, 768-779.

47 L. Tan, B. Tan, *Chemical Society Reviews* 2017, **46**, 3322-3356.

48 J. Germain, J. M. J. Fréchet, F. Svec, *Journal of Materials Chemistry* 2007, **17**, 4989-4997.

49 S. Xu, Y. Luo, B. Tan, *Macromolecular Rapid Communications* 2013, **34**, 471-484.

50 Q. Liao, E. J. Kim, Y. Tang, H. Xu, D. G. Yu, W. Song, B. J. Kim, *Journal of Polymer Science* 2024, **62**, 1517-1535.

51 C. Liu, L. Shi, J. Zhang, J. Sun, *Chemical Engineering Journal* 2022, **427**, 131633.

52 C. Liu, J. Zhang, J. Liu, Z. Tan, Y. Cao, X. Li, Z. Rao, *Angewandte Chemie International Edition* 2021, **133**, 14097-14106.

53 Y. Fu, Y. Kong, Y. Wang, Y. Cao, S. Zhong, M. Xu, T. Lei, J. Huang, *Separation and Purification Technology* 2023, **318**, 123817.

54 S. Kitagawa, *Chemical Society Reviews* 2014, **43**, 5415-5418.

55 J. Park, J.-R. Li, Y.-P. Chen, J. Yu, A. A. Yakovenko, Z. U. Wang, L.-B. Sun, P. B. Balbuena, H.-C. Zhou, *Chemical Communications* 2012, **48**, 9995-9997.

56 O. M. Yaghi, G. Li, H. Li, *Nature* 1995, **378**, 703-706.

57 H. Li, M. Eddaoudi, T. L. Groy, O. Yaghi, *Journal of the American Chemical Society* 1998, **120**, 8571-8572.

58 E. V. Perez, K. J. Balkus Jr, J. P. Ferraris, I. H. Musselman, *Journal of Membrane Science* 2009, **328**, 165-173.

59 O. M. Yaghi, M. O'Keeffe, N. W. Ockwig, H. K. Chae, M. Eddaoudi, J. Kim, *Nature* 2003, **423**, 705-714.

60 R. Freund, O. Zaremba, G. Arnauts, R. Ameloot, G. Skorupskii, M. Dincă, A. Bavykina,

J. Gascon, A. Ejsmont, J. Goscianska, *Angewandte Chemie International Edition* 2021, **60**, 23975-24001.

61 H. Furukawa, N. Ko, Y. B. Go, N. Aratani, S. B. Choi, E. Choi, A. Ö. Yazaydin, R. Q. Snurr, M. O’Keeffe, J. Kim, *Science* 2010, **329**, 424-428.

62 O. K. Farha, A. Özgür Yazaydın, I. Eryazici, C. D. Malliakas, B. G. Hauser, M. G. Kanatzidis, S. T. Nguyen, R. Q. Snurr, J. T. Hupp, *Nature Chemistry* 2010, **2**, 944-948.

63 X. Zhao, Y. Wang, D. S. Li, X. Bu, P. Feng, *Advanced Materials* 2018, **30**, 1705189.

64 H. Li, K. Wang, Y. Sun, C. T. Lollar, J. Li, H.-C. Zhou, *Materials Today* 2018, **21**, 108-121.

65 J. Lee, O. K. Farha, J. Roberts, K. A. Scheidt, S. T. Nguyen, J. T. Hupp, *Chemical Society Reviews* 2009, **38**, 1450-1459.

66 W. Xia, A. Mahmood, R. Zou, Q. Xu, *Energy & Environmental Science* 2015, **8**, 1837-1866.

67 P. Horcajada, C. Serre, M. Vallet-Regí, M. Sebban, F. Taulelle, G. Férey, *Angewandte Chemie International Edition* 2006, **45**, 5974-5978.

68 H. Furukawa, K. E. Cordova, M. O’Keeffe, O. M. Yaghi, *Science* 2013, **341**, 1230444.

69 A. P. Cote, A. I. Benin, N. W. Ockwig, M. O'Keeffe, A. J. Matzger, O. M. Yaghi, *Science* 2005, **310**, 1166-1170.

70 H. M. El-Kaderi, J. R. Hunt, J. L. Mendoza-Cortés, A. P. Côté, R. E. Taylor, M. O'Keeffe, O. M. Yaghi, *Science* 2007, **316**, 268-272.

71 P. J. Waller, F. Gándara, O. M. Yaghi, *Accounts of Chemical Research* 2015, **48**, 3053-3063.

72 B. Gui, G. Lin, H. Ding, C. Gao, A. Mal, C. Wang, *Accounts of Chemical Research* 2020, **53**, 2225-2234.

73 Y.-N. Gong, X. Guan, H.-L. Jiang, *Coordination Chemistry Reviews* 2023, **475**, 214889.

74 H. Furukawa, O. M. Yaghi, *Journal of the American Chemical Society* 2009, **131**, 8875-8883.

75 Z. Wang, S. Zhang, Y. Chen, Z. Zhang, S. Ma, *Chemical Society Reviews* 2020, **49**, 708-735.

76 Y. Qian, H.-L. Jiang, *Accounts of Chemical Research* 2024, **57**, 1214-1226.

77 N. Keller, T. Bein, *Chemical Society Reviews* 2021, **50**, 1813-1845.

78 X. Liu, D. Huang, C. Lai, G. Zeng, L. Qin, H. Wang, H. Yi, B. Li, S. Liu, M. Zhang, *Chemical Society Reviews* 2019, **48**, 5266-5302.

79 P. M. Budd, B. S. Ghanem, S. Makhseed, N. B. McKeown, K. J. Msayib, C. E. Tattershall, *Chemical Communications* 2004, 230-231.

80 P. M. Budd, E. S. Elabas, B. S. Ghanem, S. Makhseed, N. B. McKeown, K. J. Msayib, C. E. Tattershall, D. Wang, *Advanced Materials* 2004, **16**, 456-459.

81 N. B. McKeown, P. M. Budd, *Macromolecules* 2010, **43**, 5163-5176.

82 N. B. McKeown, *Polymer* 2020, **202**, 122736.

83 N. B. McKeown, *Current Opinion in Chemical Engineering* 2022, **36**, 100785.

84 Q. Song, S. Cao, R. H. Pritchard, B. Ghalei, S. A. Al-Muhtaseb, E. M. Terentjev, A. K. Cheetham, E. Sivaniah, *Nature Communications* 2014, **5**, 4813.

85 N. B. McKeown, *Science China Chemistry* 2017, **60**, 1023-1032.

86 H. W. Lai, F. M. Benedetti, Z. Jin, Y. C. Teo, A. X. Wu, M. G. D. Angelis, Z. P. Smith, Y. Xia, *Macromolecules* 2019, **52**, 6294-6302.

87 H. W. Lai, S. Liu, Y. Xia, *Journal of Polymer Science Part A: Polymer Chemistry* 2017, **55**, 3075-3081.

88 P. M. Budd, K. J. Msayib, C. E. Tattershall, B. S. Ghanem, K. J. Reynolds, N. B. McKeown, D. Fritsch, *Journal of Membrane Science* 2005, **251**, 263-269.

89 A. Wang, R. Tan, C. Breakwell, X. Wei, Z. Fan, C. Ye, R. Malpass-Evans, T. Liu, M. A. Zwijnenburg, K. E. Jelfs, *Journal of the American Chemical Society* 2022, **144**, 17198-17208.

90 R. Tan, A. Wang, R. Malpass-Evans, R. Williams, E. W. Zhao, T. Liu, C. Ye, X. Zhou, B. P. Darwich, Z. Fan, *Nature Materials* 2020, **19**, 195-202.

91 L. M. Robeson, *Journal of Membrane Science* 2008, **320**, 390-400.

92 M. Carta, M. Croad, R. Malpass-Evans, J. C. Jansen, P. Bernardo, G. Clarizia, K. Friess, M. Lanč, N. B. McKeown, *Advanced Materials* 2014, **26**, 3526-3531.

93 B. S. Ghanem, R. Swaidan, E. Litwiller, I. Pinnau, *Advanced Materials* 2014, **26**, 3688-3692.

94 B. S. Ghanem, R. Swaidan, X. Ma, E. Litwiller, I. Pinnau, *Advanced Materials* 2014, **26**, 6696-6700.

95 R. Swaidan, B. Ghanem, I. Pinnau, *ACS Macro Letters* 2015, **4**, 947-951.

96 I. Rose, C. G. Bezzu, M. Carta, B. Comesaña-Gándara, E. Lasseuguette, M. C. Ferrari, P. Bernardo, G. Clarizia, A. Fuoco, J. C. Jansen, *Nature Materials* 2017, **16**, 932-937.

97 B. Comesaña-Gándara, J. Chen, C. G. Bezzu, M. Carta, I. Rose, M.-C. Ferrari, E. Esposito, A. Fuoco, J. C. Jansen, N. B. McKeown, *Energy & Environmental Science*

2019, **12**, 2733-2740.

98 P. M. Budd, in *Sustainable Nanoscale Engineering*, ed. G. Szekely, A. Livingston, Elsevier, Amsterdam, 2020, ch. 9, pp. 231-264.

99 N. Du, G. P. Robertson, J. Song, I. Pinnau, M. D. Guiver, *Macromolecules* 2009, **42**, 6038-6043.

100 B. Satilmis, M. Lanč, A. Fuoco, C. Rizzuto, E. Tocci, P. Bernardo, G. Clarizia, E. Esposito, M. Monteleone, M. Dendisová, *Journal of Membrane Science* 2018, **555**, 483-496.

101 M. Longo, M. P. De Santo, E. Esposito, A. Fuoco, M. Monteleone, L. Giorno, B. Comesaña-Gándara, J. Chen, C. G. Bezzu, M. Carta, *Industrial & Engineering Chemistry Research* 2019, **59**, 5381-5391.

102 B. D. Freeman, *Macromolecules* 1999, **32**, 375-380.

103 M. K. Amin, C. Ye, S. Pang, Y. Liu, D. Taylor, G. S. Nichol, N. B. McKeown, *Chemical Science* 2024, **15**, 14968-14976.

104 P. T. Lansbury, J. B. Bieber, F. D. Saeva, K. R. Fountain, *Journal of the American Chemical Society* 1969, **91**, 399-405.

105 P. D. Bartlett, M. J. Ryan, S. G. Cohen, *Journal of the American Chemical Society* 1942, **64**, 2649-2653.

106 C.-F. Chen, *Chemical Communications* 2011, **47**, 1674-1688.

107 J. H. Chong, M. J. MacLachlan, *Chemical Society Reviews* 2009, **38**, 3301-3315.

108 Y. Han, Z. Meng, Y.-X. Ma, C.-F. Chen, *Accounts of Chemical Research* 2014, **47**, 2026-2040.

109 T. M. Swager, *Accounts of Chemical Research* 2008, **41**, 1181-1189.

110 S.-X. L. Luo, W. Yuan, M. Xue, H. Feng, M. J. Bezdek, T. Palacios, T. M. Swager, *ACS Nano* 2023, **17**, 2679-2688.

111 S. Dey, A. Bhunia, D. Esquivel, C. Janiak, *Journal of Materials Chemistry A* 2016, **4**, 6259-6263.

112 T. M. Long, T. M. Swager, *Advanced Materials* 2001, **13**, 601-604.

113 F. Ishiwari, Y. Shoji, C. J. Martin, T. Fukushima, *Polymer Journal* 2024, **56**, 791-818.

114 B. S. Ghanem, K. J. Msayib, N. B. McKeown, K. D. Harris, Z. Pan, P. M. Budd, A. Butler, J. Selbie, D. Book, A. Walton, *Chemical Communications* 2007, 67-69.

115 B. S. Ghanem, M. Hashem, K. D. Harris, K. J. Msayib, M. Xu, P. M. Budd, N. Chaukura, D. Book, S. Tedds, A. Walton, *Macromolecules* 2010, **43**, 5287-5294.

116 M. Woźny, A. Mames, T. Ratajczyk, *Molecules* 2021, **27**, 250.

117 G. S. Prakash, C. Panja, A. Shakhmin, E. Shah, T. Mathew, G. A. Olah, *The Journal of Organic Chemistry* 2009, **74**, 8659-8668.

118 G. Li, S. Zhou, G. Su, Y. Liu, P. G. Wang, *The Journal of Organic Chemistry* 2007, **72**, 9830-9833.

119 K. Mohammadiannejad-Abbasabadi, I. Mohammadpoor-Baltork, S. Tangestaninejad, M. Moghadam, V. Mirkhani, R. Kia, *Tetrahedron* 2016, **72**, 1433-1439.

120 A. Mallouli, Y. Lepage, *Synthesis* 1980, **1980**, 689-689.

121 L. von Kleist, S. Michaelis, K. Bartho, O. Graebner, M. n. Schlief, M. Dreger, A. K. Schrey, M. Sefkow, F. Kroll, H. Koester, *Journal of Medicinal Chemistry* 2016, **59**, 4664-4675.

122 Y. Wang, B. S. Ghanem, Y. Han, I. Pinnau, *Current Opinion in Chemical Engineering* 2022, **35**, 100755.

123 I. Rose, M. Carta, R. Malpass-Evans, M.-C. Ferrari, P. Bernardo, G. Clarizia, J. C. Jansen, N. B. McKeown, *ACS Macro Letters* 2015, **4**, 912-915.

124 S. C. Dakdouki, D. Villemin, N. Bar, *European Journal of Organic Chemistry* 2011, **2011**, 4448-4454.

125 R. Criegee, L. Kraft, B. Rank, *Justus Liebigs Annalen der Chemie* 1933, **507**, 159-197.

126 A. Fuoco, B. Comesaña-Gándara, M. Longo, E. Esposito, M. Monteleone, I. Rose, C. G. Bezzu, M. Carta, N. B. McKeown, J. C. Jansen, *ACS Applied Materials & Interfaces* 2018, **10**, 36475-36482.

127 J. G. Wijmans, R. W. Baker, *Journal of Membrane Science* 1995, **107**, 1-21.

128 V. Teplyakov, P. Meares, *Gas Separation & Purification* 1990, **4**, 66-74.

129 R. Swaidan, B. S. Ghanem, E. Litwiller, I. Pinnau, *Journal of Membrane Science* 2014, **457**, 95-102.

130 N. Du, H. B. Park, G. P. Robertson, M. M. Dal-Cin, T. Visser, L. Scoles, M. D. Guiver, *Nature Materials* 2011, **10**, 372-375.

131 H. A. Patel, C. T. Yavuz, *Chemical Communications* 2012, **48**, 9989-9991.

132 J. Chen, M. Longo, A. Fuoco, E. Esposito, M. Monteleone, B. Comesaña Gándara, J. Carolus Jansen, N. B. McKeown, *Angewandte Chemie International Edition* 2023, **62**, e202215250.

133 S. Guo, J. Y. Yeo, F. M. Benedetti, D. Syar, T. M. Swager, Z. P. Smith, *Angewandte Chemie International Edition* 2024, **136**, e202315611.

134 L. C. Moh, J. B. Goods, Y. Kim, T. M. Swager, *Journal of Membrane Science* 2018, **549**, 236-243.

135 T. Wong, Y. Yang, R. Tan, A. Wang, Z. Zhou, Z. Yuan, J. Li, D. Liu, A. Alvarez-Fernandez, C. Ye, *Joule* 2025, **9**, 101795.

136 S. Guo, T. M. Swager, *Journal of the American Chemical Society* 2021, **143**, 11828-11835.

137 K. R. Storme, B. S. Schreib, Z. P. Smith, T. M. Swager, *Macromolecules* 2024, **57**, 7065-7073.

138 L. Hou, Z. Wang, Z. Chen, W. Chen, C. Yang, *Separation and Purification Technology* 2020, **242**, 116766.

139 Y. Zheng, X. Yang, M. Yuan, J. Luo, *High Performance Polymers* 2019, **31**, 1173-1182.

140 G. Wittig, R. Ludwig, *Angewandte Chemie* 1956, **68**, 40-40.

141 T. F. Mich, E. J. Nienhouse, T. E. Farino, J. J. Tufariello, *Journal of Chemical Education* 1968, **45**, 272.

142 L. Friedman, F. M. Logullo, *Journal of the American Chemical Society* 1963, **85**, 1549-1549.

143 R. L. Letsinger, P. T. Lansbury, *Journal of the American Chemical Society* 1959, **81**, 935-939.

144 T. Saitoh, S. Yoshida, J. Ichikawa, *Organic Letters* 2004, **6**, 4563-4565.

145 L. R. C. Barclay, R. A. Chapman, *Canadian Journal of Chemistry* 1965, **43**, 1754-1760.

146 R. Malpass-Evans, PhD Thesis, Cardiff University, 2014.

147 A. Okamoto, S. Watanabe, K. Nakaema, N. Yonezawa, *Crystal Structure Theory and Applications* 2012, **1**, 121-127.

148 A. Mallouli, Y. Lepage, *Synthesis* 1980, **9**, 689.

149 A. G. Griesbeck, B. Öngel, M. Atar, *Journal of Physical Organic Chemistry* 2017, **30**, e3741.

150 H. Santoso, M. I. Casana, C. D. Donner, *Organic & Biomolecular Chemistry* 2014, **12**, 171-176.

151 M. J. M. Cabrera, J. Tauber, M. J. Krische, *Angewandte Chemie International Edition* 2018, **57**, 1390.

152 R. K. Roy, E. B. Gowd, S. Ramakrishnan, *Macromolecules* 2012, **45**, 3063-3069.

153 A. Okamoto, S. Watanabe, K. Nakaema, N. Yonezawa, *Crystal Structure Theory and*

Applications 2012, **1**, 121.

154 P. M. Budd, E. S. Elabas, B. S. Ghanem, S. Makhseed, N. B. McKeown, K. J. Msayib, C. E. Tattershall, D. Wang, *Advanced Materials* 2004, **16**, 456-459.

155 M. A. Abdulhamid, S.-H. Park, Z. Zhou, D. A. Ladner, G. Szekely, *Journal of Membrane Science* 2021, **621**, 118997.

Appendix

^{1}H NMR and ^{13}C NMR spectrum of monomers

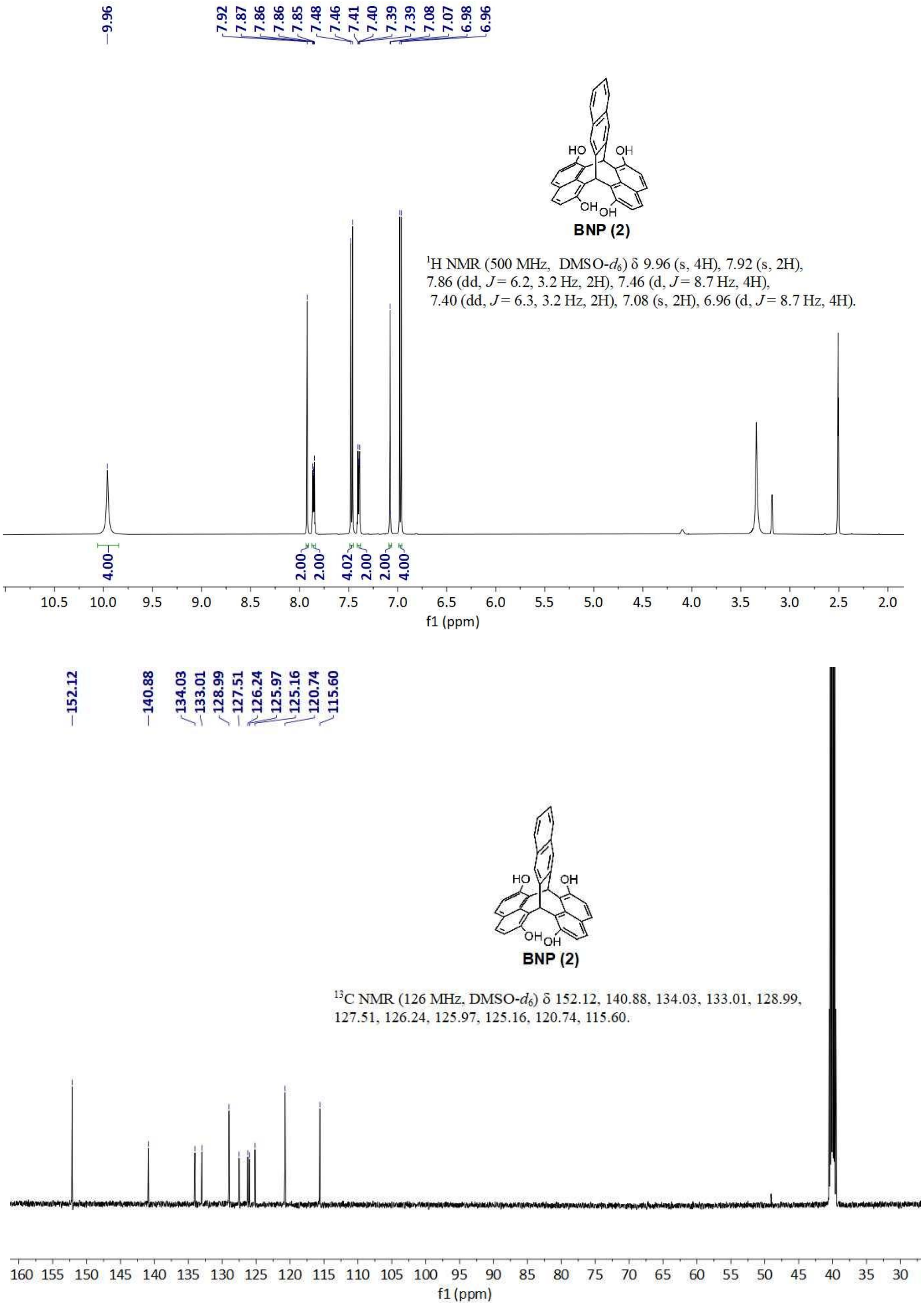

^{1}H NMR (500 MHz, DMSO-d_6) δ 9.96 (s, 4H), 7.92 (s, 2H), 7.86 (dd, J = 6.2, 3.2 Hz, 2H), 7.46 (d, J = 8.7 Hz, 4H), 7.40 (dd, J = 6.3, 3.2 Hz, 2H), 7.08 (s, 2H), 6.96 (d, J = 8.7 Hz, 4H).

^{13}C NMR (126 MHz, DMSO-d_6) δ 152.12, 140.88, 134.03, 133.01, 128.99, 127.51, 126.24, 125.97, 125.16, 120.74, 115.60.

Figure A1 ^{1}H NMR (top) and ^{13}C NMR (bottom) spectrum of **BNP (2)**.

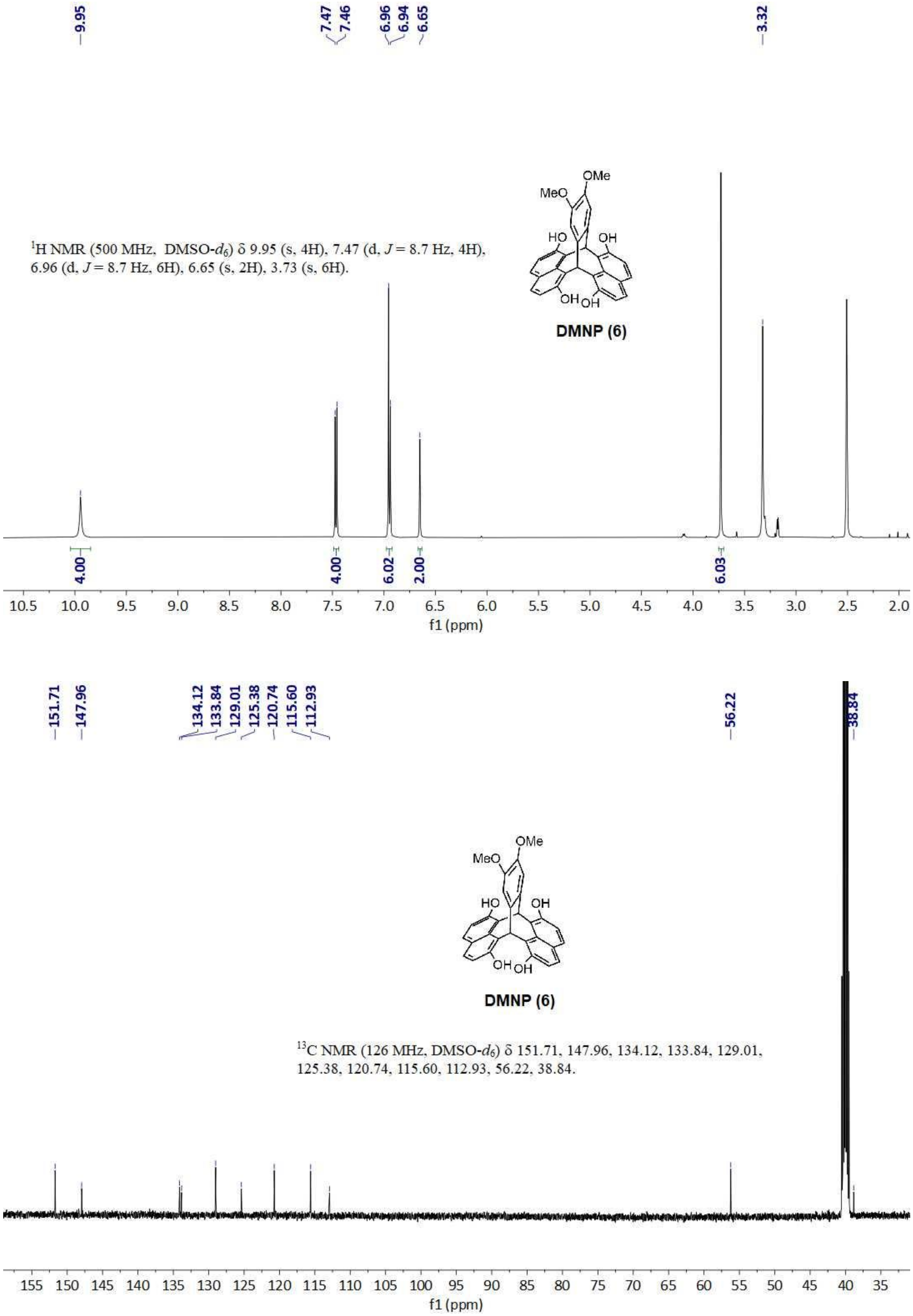

^{1}H NMR (500 MHz, DMSO-d_6) δ 9.95 (s, 4H), 7.47 (d, *J* = 8.7 Hz, 4H), 6.96 (d, *J* = 8.7 Hz, 6H), 6.65 (s, 2H), 3.73 (s, 6H).

^{13}C NMR (126 MHz, DMSO-d_6) δ 151.71, 147.96, 134.12, 133.84, 129.01, 125.38, 120.74, 115.60, 112.93, 56.22, 38.84.

Figure A2 ^{1}H NMR (top) and ^{13}C NMR (bottom) spectrum of **DMNP (6)**.

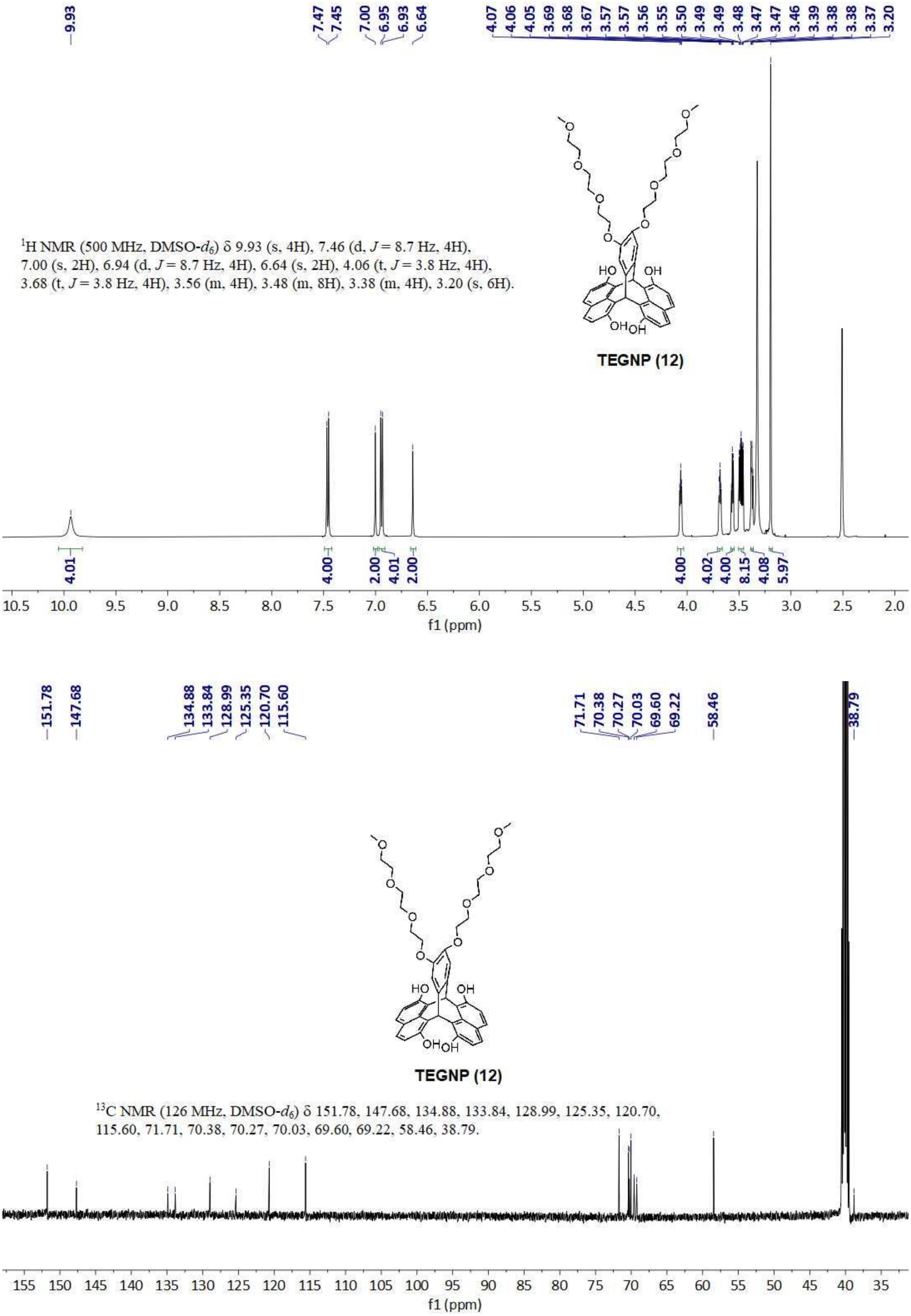

^{1}H NMR (500 MHz, DMSO-d_6) δ 9.93 (s, 4H), 7.46 (d, J = 8.7 Hz, 4H), 7.00 (s, 2H), 6.94 (d, J = 8.7 Hz, 4H), 6.64 (s, 2H), 4.06 (t, J = 3.8 Hz, 4H), 3.68 (t, J = 3.8 Hz, 4H), 3.56 (m, 4H), 3.48 (m, 8H), 3.38 (m, 4H), 3.20 (s, 6H).

^{13}C NMR (126 MHz, DMSO-d_6) δ 151.78, 147.68, 134.88, 133.84, 128.99, 125.35, 120.70, 115.60, 71.71, 70.38, 70.27, 70.03, 69.60, 69.22, 58.46, 38.79.

Figure A3 ^{1}H NMR (top) and ^{13}C NMR (bottom) spectrum of **TEGNP (12)**.

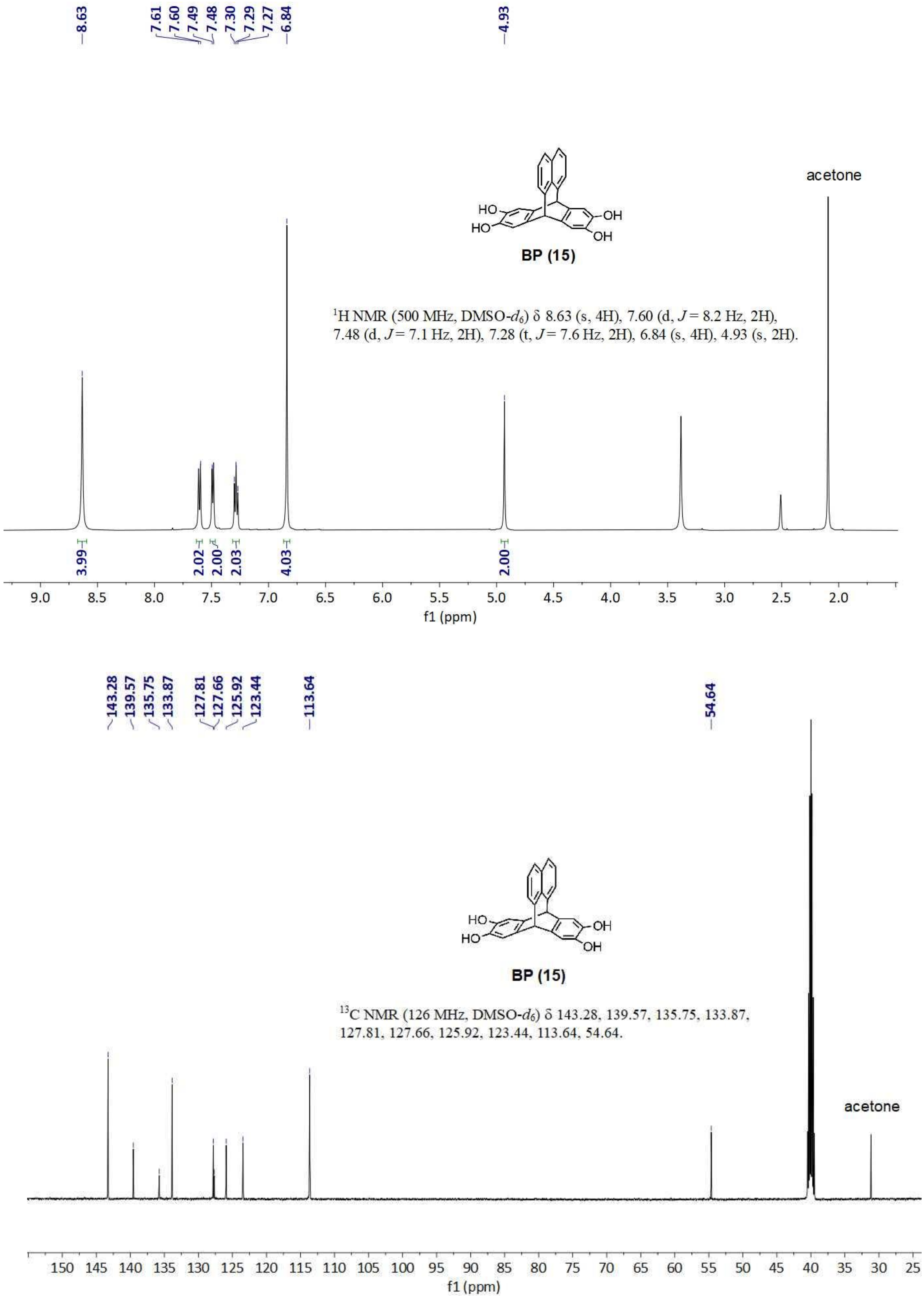

^{1}H NMR (500 MHz, DMSO-*d*$_6$) δ 8.63 (s, 4H), 7.60 (d, *J* = 8.2 Hz, 2H), 7.48 (d, *J* = 7.1 Hz, 2H), 7.28 (t, *J* = 7.6 Hz, 2H), 6.84 (s, 4H), 4.93 (s, 2H).

^{13}C NMR (126 MHz, DMSO-*d*$_6$) δ 143.28, 139.57, 135.75, 133.87, 127.81, 127.66, 125.92, 123.44, 113.64, 54.64.

Figure A4 ^{1}H NMR (top) and ^{13}C NMR (bottom) spectrum of **BP (15)**.

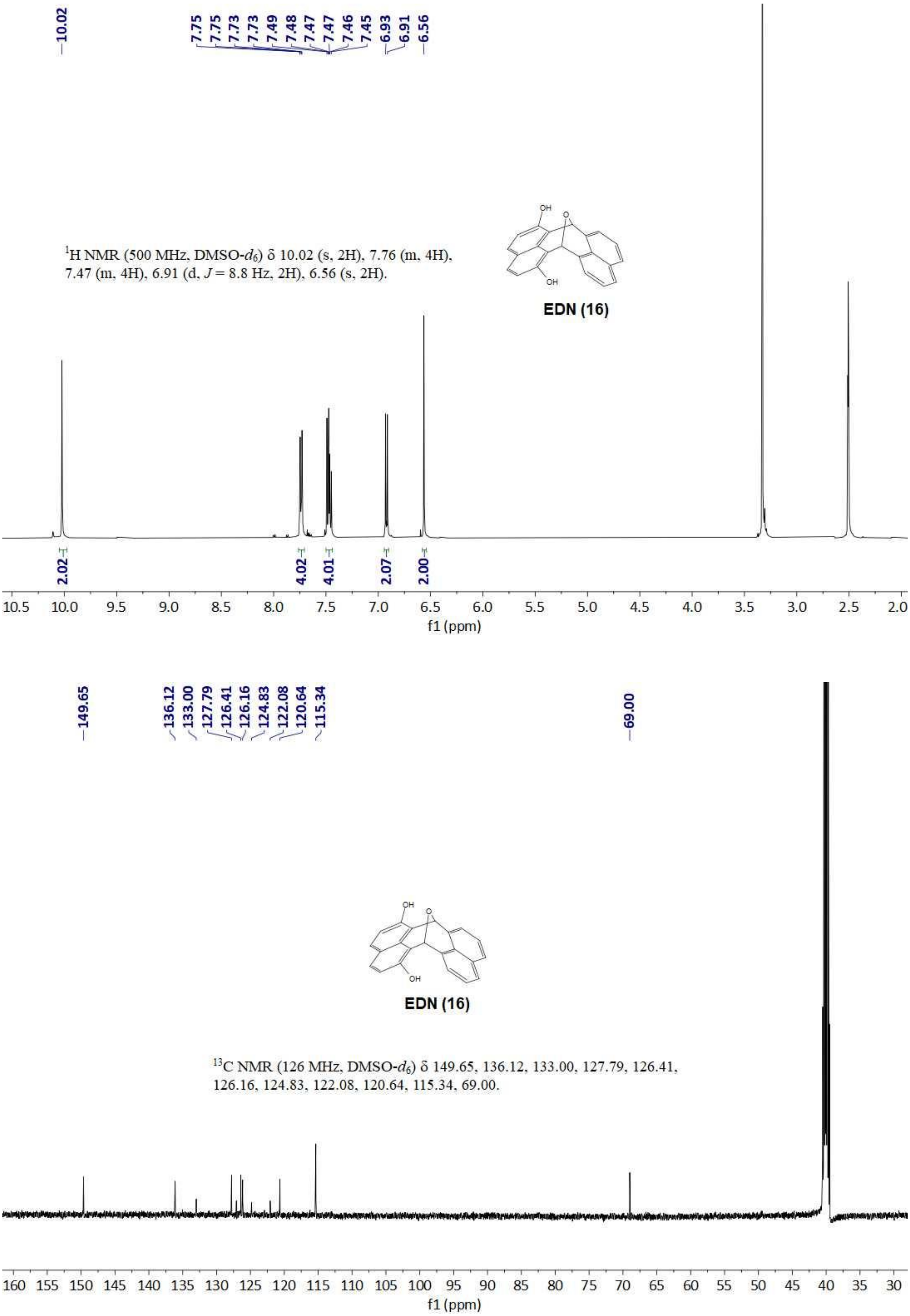

^{1}H NMR (500 MHz, DMSO-d_6) δ 10.02 (s, 2H), 7.76 (m, 4H), 7.47 (m, 4H), 6.91 (d, J = 8.8 Hz, 2H), 6.56 (s, 2H).

^{13}C NMR (126 MHz, DMSO-d_6) δ 149.65, 136.12, 133.00, 127.79, 126.41, 126.16, 124.83, 122.08, 120.64, 115.34, 69.00.

Figure A5 ^{1}H NMR (top) and ^{13}C NMR (bottom) spectrum of **EDN (16)**.

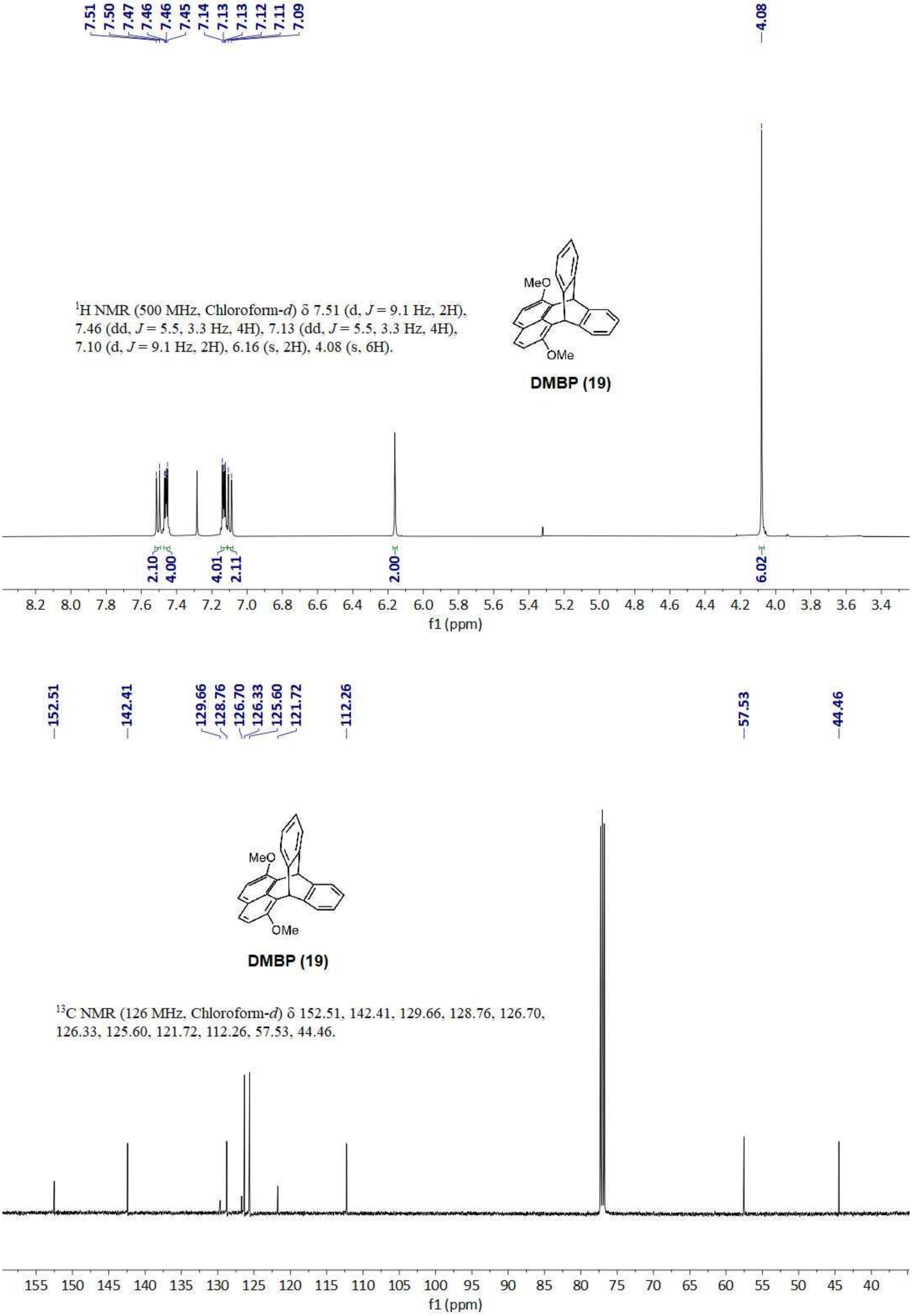

^{1}H NMR (500 MHz, Chloroform-*d*) δ 7.51 (d, *J* = 9.1 Hz, 2H), 7.46 (dd, *J* = 5.5, 3.3 Hz, 4H), 7.13 (dd, *J* = 5.5, 3.3 Hz, 4H), 7.10 (d, *J* = 9.1 Hz, 2H), 6.16 (s, 2H), 4.08 (s, 6H).

DMBP (19)

DMBP (19)

^{13}C NMR (126 MHz, Chloroform-*d*) δ 152.51, 142.41, 129.66, 128.76, 126.70, 126.33, 125.60, 121.72, 112.26, 57.53, 44.46.

Figure A6 ^{1}H NMR (top) and ^{13}C NMR (bottom) spectrum of **DMBP (19)**.

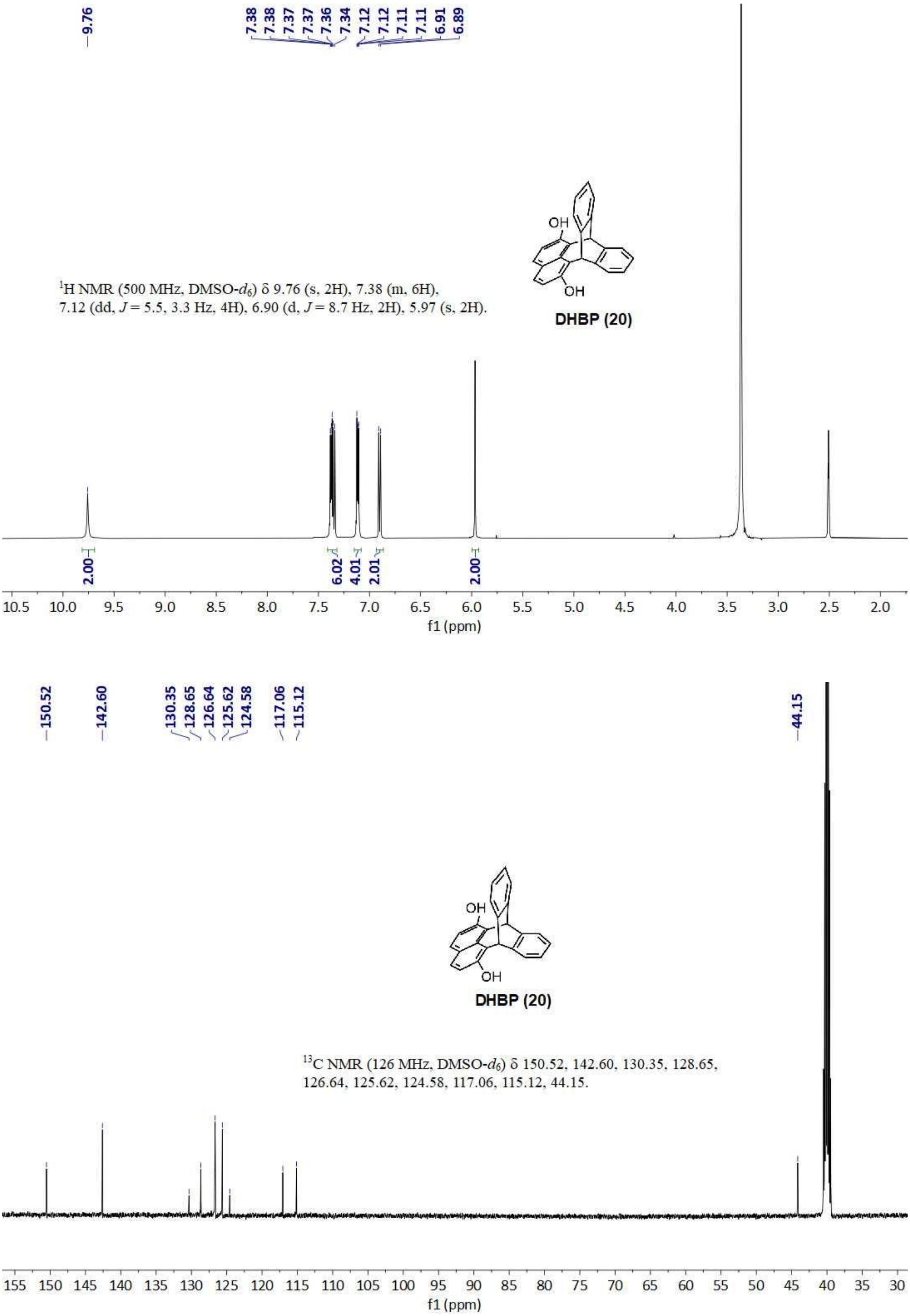

^{1}H NMR (500 MHz, DMSO-d_6) δ 9.76 (s, 2H), 7.38 (m, 6H), 7.12 (dd, J = 5.5, 3.3 Hz, 4H), 6.90 (d, J = 8.7 Hz, 2H), 5.97 (s, 2H).

^{13}C NMR (126 MHz, DMSO-d_6) δ 150.52, 142.60, 130.35, 128.65, 126.64, 125.62, 124.58, 117.06, 115.12, 44.15.

Figure A7 ^{1}H NMR (top) and ^{13}C NMR (bottom) spectrum of **DHBP (20)**.